JOURNAL OF PETROLOGY | VOLUME 0 | NUMBER 0 | PAGES 1–44 | 2012 | doi:10.1093/petrology/egs058
Journal of Petrology Advance Access published October 4, 2012

Crustal Melting and Flow beneath Northern Tibet: Evidence from Mid-Miocene to Quaternary Strongly Peraluminous Rhyolites in the Southern Kunlun Range

QIANG WANG[1,2]*, SUN-LIN CHUNG[3], XIAN-HUA LI[4], DEREK WYMAN[5], ZHENG-XIANG LI[2], WEI-DONG SUN[1], HUA-NING QIU[1], YONG-SHENG LIU[6] AND YING-TANG ZHU[7]

[1]STATE KEY LABORATORY OF ISOTOPE GEOCHEMISTRY, GUANGZHOU INSTITUTE OF GEOCHEMISTRY, CHINESE ACADEMY OF SCIENCES, GUANGZHOU 510640, CHINA

[2]ARC CENTRE OF EXCELLENCE FOR CORE TO CRUST FLUID SYSTEMS (CCFS) AND THE INSTITUTE FOR GEOSCIENCE RESEARCH (TIGER), DEPARTMENT OF APPLIED GEOLOGY, CURTIN UNIVERSITY, PERTH, WA 6845, AUSTRALIA

[3]DEPARTMENT OF GEOSCIENCES, NATIONAL TAIWAN UNIVERSITY, PO BOX 13-318, TAIPEI 10617, TAIWAN

[4]INSTITUTE OF GEOLOGY AND GEOPHYSICS, CHINESE ACADEMY OF SCIENCES, BEIJING 100029, CHINA

[5]SCHOOL OF GEOSCIENCES, UNIVERSITY OF SYDNEY, NSW 2006, AUSTRALIA

[6]STATE KEY LABORATORY OF GEOLOGICAL PROCESSES AND MINERAL RESOURCES, FACULTY OF EARTH SCIENCES, CHINA UNIVERSITY OF GEOSCIENCES, WUHAN, 430074, CHINA

[7]SEDIMENTARY GEOLOGY INSTITUTE, CHENGDU UNIVERSITY OF TECHNOLOGY, CHENGDU, 610059, CHINA

RECEIVED SEPTEMBER 5, 2011; ACCEPTED AUGUST 9, 2012

One of the major geophysical discoveries concerning the Tibetan Plateau is the existence of unusually weak layers in the mid- to lower crust, a characteristic widely interpreted as the result of crustal melting. This interpretation, however, remains highly contentious, particularly when applied to northern Tibet where crustally derived magmatic rocks are scarce. Here we report the finding of tourmaline-bearing mica and biotite rhyolites in the Bukadaban–Malanshan area, southern Kunlun Range, near the northern margin of the Tibetan Plateau. Zircon U–Pb and whole-rock or mineral ^{40}Ar–^{39}Ar analyses suggest that these rocks erupted between 9·0 and 1·5 Ma. These rocks are geochemically similar to Himalayan leucogranites (interpreted as crustal melts), with strongly peraluminous compositions, high SiO_2 contents (69·0–76·0 wt %), and clear negative Eu, Ba and Sr anomalies. They have low εNd (−5·8 to −8·6) and high $^{87}Sr/^{86}Sr$ (0·7125–0·7178), $^{206}Pb/^{204}Pb$ (18·59–18·70), $^{207}Pb/^{204}Pb$ (15·49–15·63) and $^{208}Pb/^{204}Pb$ (38·31–38·74) isotopic compositions as well as magmatic zircon εHf (−0·7 to −5·0) compositions similar to those of global marine sediments and Proterozoic–Triassic sedimentary rocks in northern Tibet. We suggest that the Bukadaban–Malanshan rhyolites were generated by dehydration melting of metasedimentary rocks at 0·5–1·2 GPa and 740–863°C. Our data not only confirm the occurrence of a partially molten zone in the mid- to lower crust beneath northern Tibet but also constrain the crustal melting to have existed from middle Miocene to Quaternary times. Adopting the crustal flow model, we further argue the importance of outward flowing of the melt-weakened crust in the formation of crustal inflation, surface uplift, and earthquakes along the northern margin of the Tibetan Plateau.

KEY WORDS: *Tibet; crustal melting; crustal flow; low-velocity zone; crustal thickening; plateau growth*

*Corresponding author. E-mail: wqiang@gig.ac.cn

INTRODUCTION

The Tibetan Plateau is characterized by anomalously thick (~50–90 km) continental crust and is the product of continuous convergence between India and Eurasia (England & Houseman, 1989; Owens & Zandt, 1997; Yin & Harrison, 2000; Tapponnier *et al*., 2001; Chung *et al*., 2005, 2009; Royden *et al*., 2008). However, the mechanisms for crustal thickening and the development of the Tibetan Plateau topography remain controversial. Two end-member models have been proposed: (1) brittle crustal thickening by stacking of crustal duplexes along thrust faults with major strike-slip shearing (e.g. Tapponnier *et al*., 2001; Yin *et al*., 2008*a*; Hubbard & Shaw, 2009); (2) ductile flow and inflation of low-viscosity materials within the mid- to lower crust (e.g. Bird, 1991; Royden *et al*., 1997, 2008; Clark & Royden, 2000; Grujic *et al*., 2002; Cowgill *et al*., 2003; Enkelmann *et al*., 2006; Grujic, 2006; Searle *et al*., 2006; Harris, 2007; King *et al*., 2007; Cook & Royden, 2008; Yao *et al*., 2008; Bai *et al*., 2010; Unsworth, 2010; Wang *et al*., 2010; Jamieson *et al*., 2011).

Geophysical investigations have repeatedly demonstrated the presence of low-velocity zones (LVZs) interpreted to be unusually weak layers at different depths in the mid- to lower (15–50 km) crust throughout Tibet (e.g. Nelson *et al*., 1996; Owens & Zandt, 1997; Wei *et al*., 2001; Unsworth *et al*., 2004, 2005; Klemperer, 2006; Le Pape *et al*., 2012). In southern Tibet, these LVZs have been widely considered to be partially molten layers in the middle (15–30 km) crust (e.g. Pham *et al*., 1986; Nelson *et al*., 1996; Owens & Zandt, 1997; Unsworth *et al*., 2004, 2005; Ashish *et al*., 2009; Caldwell *et al*., 2009; Bai *et al*., 2010; Zhang & Klemperer, 2010). This interpretation implies that partial melting decreases the strength and the effective viscosity of the crustal rocks by several orders of magnitude, that the partially molten crustal layer is weaker than the domains above and below, and that a horizontal pressure gradient can occur, leading to the process of crustal channel flow (Beaumont *et al*., 2001; Grujic *et al*., 2002; Grujic, 2006; Searle *et al*., 2006, 2007, 2009; Harris, 2007). It also considers that southern Tibet is a region under which partial melting of the continental crust of India has occurred and that the extrusion of crustal materials southward has exposed the Greater Himalayan Sequence and associated leucogranites. The leucogranites, emplaced throughout the Himalayas from 28 to 9 Ma (Le Fort *et al*., 1987; Harrison *et al*., 1999; Searle *et al*., 1997, 2006, 2007, 2009; Grujic *et al*., 2002; Visonà & Lombardo, 2002; Searle & Godin, 2003; Zhang *et al*., 2004; Kellett *et al*., 2009; King *et al*., 2011; Guo & Wilson, 2012) (Fig. 1a), are considered to have formed via dehydration melting of metasedimentary rocks (e.g. Inger & Harris, 1993; Harris & Massey, 1994; Harris *et al*., 1995; Patiño Douce & Harris, 1998; Knesel & Davidson, 2002), and are interpreted as solidified exposures of the mid-crustal melts that are now present beneath southern Tibet (Nelson *et al*., 1996; Grujic *et al*., 1996, 2002; Gaillard *et al*., 2004; Searle *et al*., 2006, 2007, 2009; Kellett *et al*., 2009). There are also other views regarding the cause of such weak crustal layers, such as crustal shearing (Wittlinger *et al*., 1998; Tapponnier *et al*., 2001), preferred horizontal orientation of mica crystals immersed in a matrix of isotropic crystals (Shapiro *et al*., 2004), aqueous fluid-bearing rocks (Klemperer, 2006), intruding mantle-derived melts (Wei *et al*., 2001), and a layer separating upper felsic and lower mafic lithologies (Vergne *et al*., 2002; Hetényi *et al*., 2007) in the mid- to lower crust. In addition, some workers have argued that such weak crustal layers in southern Tibet are thin and are present in only limited areas (e.g. Harrison, 2006; Nábelek *et al*., 2009; Wittlinger *et al*., 2009).

In northern Tibet, weak crustal layers are observed at different depths (15–50 km) in the crust (Owens & Zandt, 1997; Wei *et al*., 2001; Unsworth *et al*., 2004; Klemperer, 2006; Le Pape *et al*., 2012). Most Cenozoic magmatic rocks recognized in the area originated from low-degree melting of enriched mantle sources (Arnaud *et al*., 1992; Turner *et al*., 1993, 1996; Ding *et al*., 2003; Chung *et al*., 2005; Guo *et al*., 2006). Crustally derived magmas are scarce, with comparatively small outcrops of ~11–4 Ma leucogranites and rhyolites previously being identified only in the Ulugh Muztagh and Weixueshan areas (Burchfiel *et al*., 1989; McKenna & Walker, 1990; Jolivet *et al*., 2003) (Fig. 1b and c). In this study, we report the finding of 9·0–1·5 Ma tourmaline-bearing muscovite and biotite rhyolites from the Bukadaban–Malanshan (BM) area, southern Kunlun Range (Fig. 1c). We note that these silicic rocks occur in high-altitude (>5000 m) areas near major glaciers, following the approximately east–west-trending Kunlun Fault Zone along which the 2001 Hohxil earthquake and a 426 km long surface rupture zone took place (Lin *et al*., 2002; Xu *et al*., 2006) (Fig. 1b and c). These magmatic rocks therefore allow us to study the deep geodynamic processes involved in crustal melting, and its relation to the seismicity, crustal thickening and surface uplift along the northern margin of the Tibetan Plateau.

REGIONAL GEOLOGY AND SAMPLE PETROLOGY

The Tibetan Plateau mainly comprises the Songpan–Ganzi, Qiangtang and Lhasa blocks (Yin & Harrison, 2000; Chung *et al*., 2005) (Fig. 1a). The Songpan–Ganzi Block is bounded by the Jinshajiang suture to the south and the Anyimaqen–Kunlun–Muztagh suture to the north (Yin & Harrison, 2000). The exposed Songpan–Ganzi Block consists mainly of Triassic and younger strata with some Early Mesozoic granites exposed in the eastern part (Yin & Harrison, 2000; Weislogel *et al*., 2006).

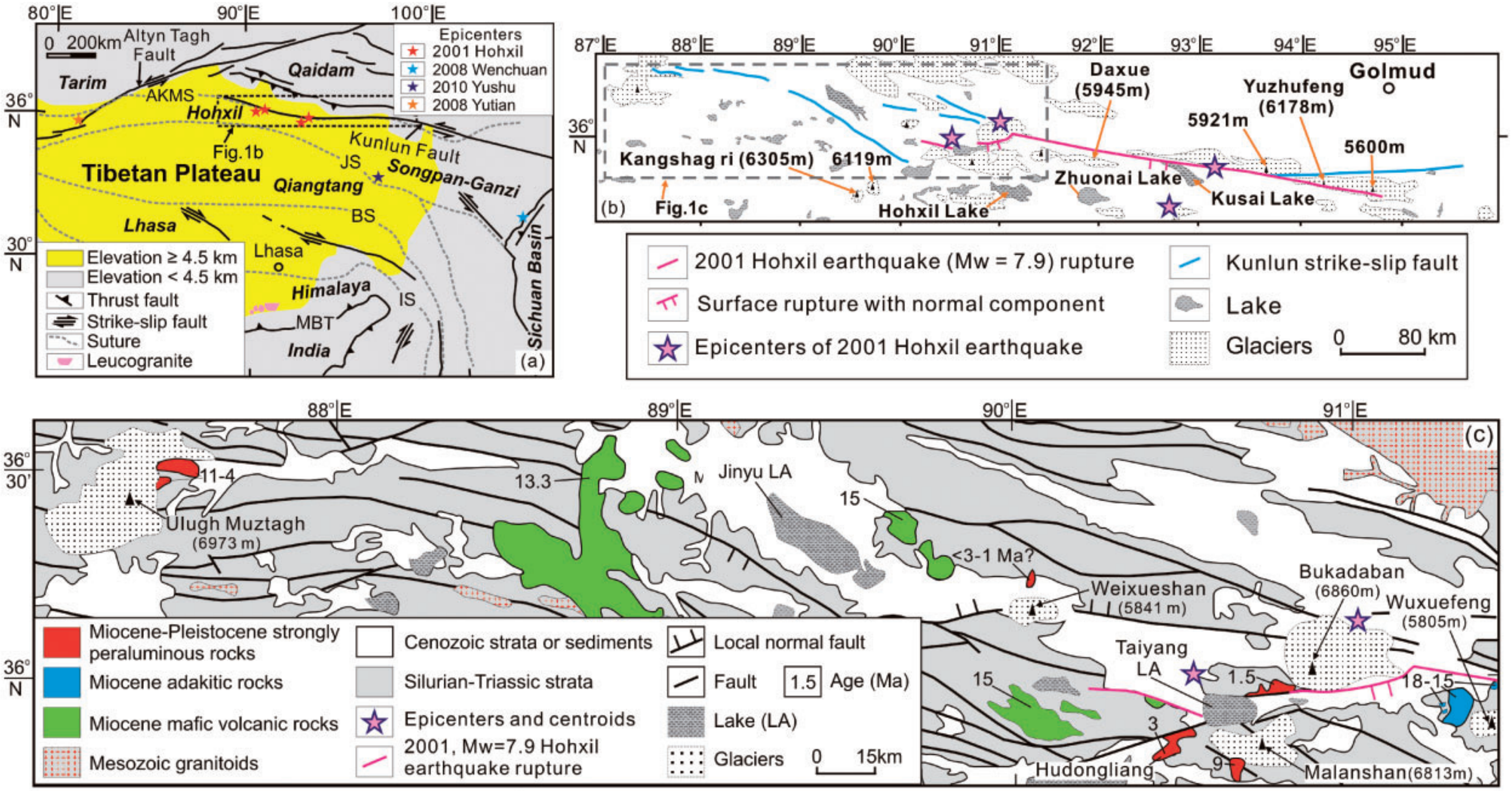

Fig. 1. (a) Tectonic map of the Tibetan Plateau showing the major terrane blocks (modified from Chung *et al.*, 2005). Main suture zones: AKMS, Anyimaqen–Kunlun–Muztagh; JS, Jinshajiang; BS, Bangong; IS, Indus. Major fault: MBT, Main Boundary Thrust. The epicenters for the 2001 Hohxil, 2008 Wenchuan and Yutian, and 2010 Yushu earthquakes are from Lin *et al.* (2002), Li *et al.* (2005), Burchfiel *et al.* (2008), Royden *et al.* (2008), Elliott *et al.* (2010) and http://earthquake.usgs.gov/earthquakes/shakemap/global/shake/2010vacp/. (b) Sketch map of the Kunlun Ranges showing the location of the epicenters and ruptures of the 2001 Hohxil earthquake (after Lin *et al.* (2002), Li *et al.* (2005) and Xu *et al.* (2006)). (c) Sketch map of the southern Kunlun Ranges showing the locations of Miocene–Pleistocene peraluminous leucogranites and rhyolites in the Ulugh Muztagh, Weixueshan (Burchfiel *et al.*, 1989; McKenna & Walker, 1990; Jolivet *et al.*, 2003) and Bukadaban–Malanshan (this study) areas, Miocene adakitic rocks near the Wuxuefeng area (Wang *et al.*, 2005), and the epicenters and ruptures of the 2001 Hohxil earthquake (Lin *et al.*, 2002; Li *et al.*, 2005). Thrusts, strike-slip faults and normal faults in the Kunlun Ranges are after Jolivet *et al.* (2003). The normal component in the west of the 2001 Hohxil earthquake rupture is after Xu *et al.* (2006). Age data for the Ulugh Muztagh leucogranites and rhyolitic rocks are from Burchfiel *et al.* (1989). The age for the Weixueshan rhyolites was estimated based on detailed geological and petrological evidence from Jolivet *et al.* (2003).

Table 1: Sample localities, grid coordinates, mineralogy and ages of rhyolitic rock samples from the Bukadaban–Malanshan area

Location and sample	Latitude	Longitude	Altitude(m)	Rock type	Mineralogy	Age analyses			
						Phase dated	Method	Age (Ma, 2σ)	MSWD
Bukadaban									
2509	35°58′09″N	90°48′06″E	5159	biotite rhyolite	Kf + Pl + Bi + Q + Zr + Ap + Cm + Gm	whole-rock	GZA	1·68 ± 0·08	4·9
						K-feldspar	GZA	1·46 ± 0·14	58
						zircon	WHL	1·55 ± 0·03	4·9
						zircon	GZL	1·54 ± 0·07	0·47
						zircon	BJC	1·55 ± 0·02	2·6
2509a	35°58′09″N	90°48′06″E	5158		Kf + Pl + Bi + Q + Zr + Ap + Cm + Gm				
2511-1	35°57′57″N	90°47′15″E	5146		Kf + Pl + Bi + Q + Zr + Ap + Cm + Gm				
Southern Malanshan									
2303	35°45′12″N	90°39′47″E	5234	biotite rhyolitic porphyry	Kf + Pl + Bi + Q + Zr + Ap	zircon	WHL	9·06 ± 0·19	0·72
						zircon	GZL	9·05 ± 0·34	0·34
						zircon	BJC	9·04 ± 0·25	1·5
2303a	35°45′04″N	90°39′23″E	5239						
Hudongliang									
$1P_2JD7$-1	35°47′26″N	90°25′39″E	5160	tourmaline-bearing two-mica rhyolite	Kf + Ab + Bi + Q + Mus + Tm + Zr + Ap + Cm + Gm	whole rock	GZA	3·09 ± 0·23	0·90
						K-feldspar	GZA	2·94 ± 0·07	2·0
						zircon	WHL	3·07 ± 0·04	1·8
						zircon	BJC	3·14 ± 0·05	2·5
$1P_2JD7$-1a	35°47′26″N	90°25′39″E	5162						
2011a	35°50′54″N	90°29′4″E	5100						

Ab, albite; Ap, apatite; Bi, biotite; Cm, cryptocrystalline materials; Gm, glassy materials; Kf, K-feldspar; Mus, muscovite; Pl, plagioclase; Q, quartz; Tm, tourmaline; Zr, zircon. All these rocks are lavas with massive structures and porphyritic textures. MSWD, mean square of weighted deviates. Analytical methods: GZA: $^{40}Ar/^{39}Ar$ analyses at the Key Laboratory of Isotope Geochronology and Geochemistry (KLIGG), Guangzhou Institute of Geochemistry (GIG), Chinese Academy of Sciences (CAS); WHL: LA-ICP-MS zircon U–Pb analyses at the National Key Laboratory of Geological Processes and Mineral Resources, Faculty of Earth Sciences, China University of Geosciences (Wuhan); GZL: LA-ICP-MS zircon U–Pb analyses at the KLIGG, GIG CAS; BJC: CASIMS zircon U–Pb analyses at the Institute of Geology and Geophysics, CAS in Beijing.

The magmatic rocks that we discovered crop out as small volcanic domes or lava flows in the southern Malanshan, Hudongliang and Bukadaban localities of the northern Hohxil district (central Songpan–Ganzi Block) (Fig. 1a–c; Electronic Appendix 1, available for downloading at http://www.petrology.oxfordjournals.org). As they mainly occur in high-altitude areas between 5100 and 5500 m, they are often overlain by modern glaciers (Electronic Appendix 1). They mainly consist of rhyolitic lavas overlying Permian–Triassic sedimentary rocks or Paleocene formations and porphyries occurring near volcanic necks. These lava flows generally have thicknesses ranging from several metres to ~350 m and are mainly distributed along west–east-trending faults (Fig. 1c). The Bukadaban lavas are located in very close proximity to the surface rupture zone of the 2001 Hohxil earthquake (Fig. 1c). At the southern Malanshan site, the lavas unconformably overlie Triassic sedimentary rocks and at the other two localities the lavas overlie Permian–Triassic sedimentary rocks or Paleocene formations (Fig. 1c). We collected eight rhyolite lava and porphyry samples from the above three locations. The detailed localities, coordinates, mineralogy and ages for all the samples are listed in Table 1.

These rhyolitic rocks exhibit porphyritic textures and mainly consist of tourmaline-bearing two-mica or biotite rhyolites or rhyolitic porphyries (Fig. 2; Table 1). The southern Malanshan biotite rhyolitic porphyries are subvolcanic rocks located close to a volcanic neck (Fig. 2a and b). They consist of potassium feldspar, plagioclase, biotite and quartz phenocrysts and a similar microlitic groundmass mineral assemblage with cryptocrystalline materials.

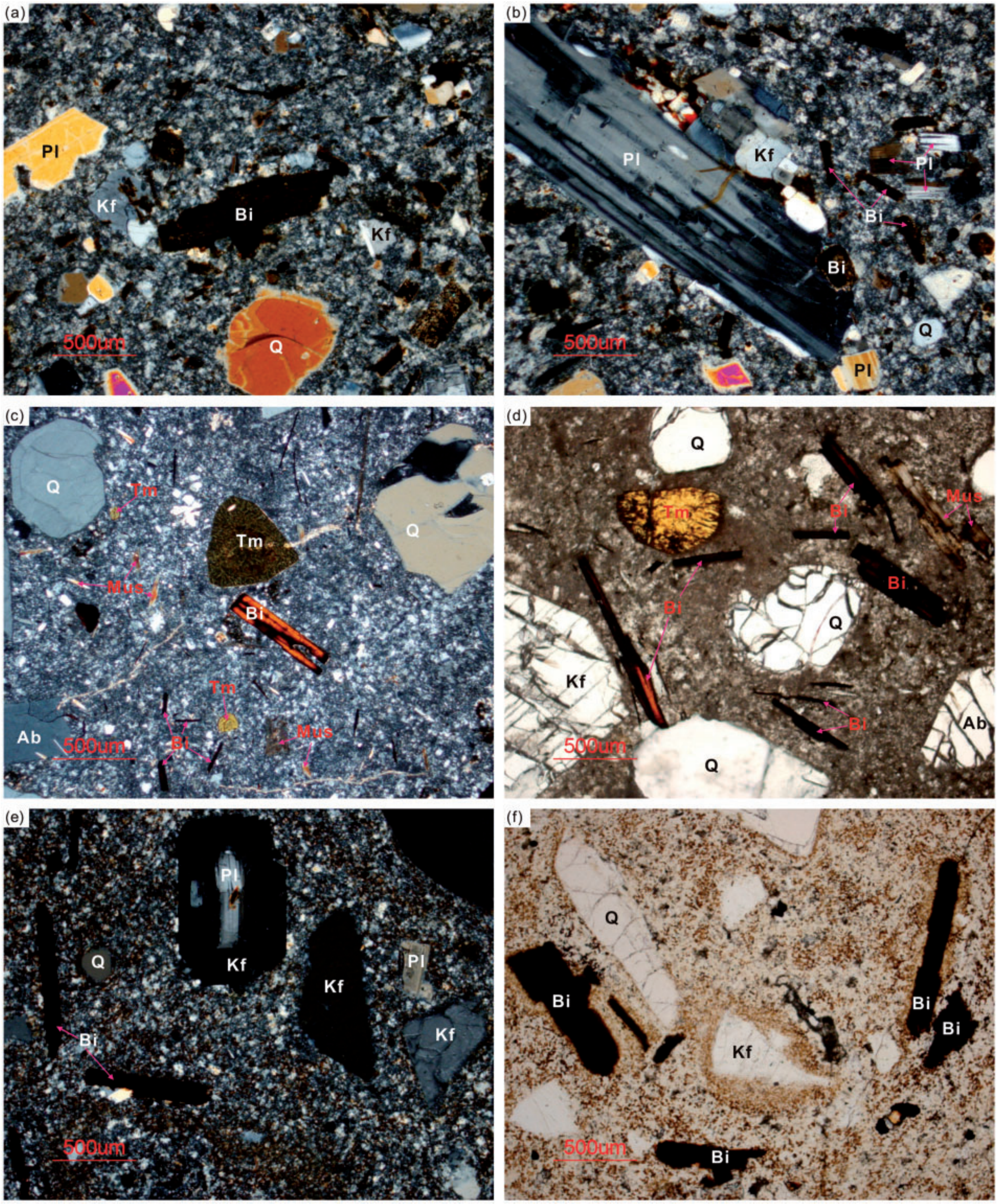

Fig. 2. Photomicrographs of the Bukadaban–Malanshan rhyolitic rocks. (a) Porphyrytic texture of the southern Malanshan biotite rhyolitic porphyry [sample 2303, crossed polarized light (xpl)]. (b) Plagioclase, potassium feldspar, biotite and quartz phenocrysts in the southern Malanshan biotite rhyolitic porphyry (sample 2303, xpl). (c) Porphyritic texture of the Hudongliang tourmaline-bearing two-mica rhyolite (sample $1P_2$JD7-1, xpl). (d) Potassium feldspar, albite, biotite, quartz, muscovite, and Fe-rich tourmaline phenocrysts in the Hudongliang rhyolite [sample $1P_2$JD7-1, plane-polarized light (ppl)]. (e) Porphyritic texture and phenocryst minerals of the Bukadaban biotite rhyolite (sample 2509, xpl). (f) Potassium feldspar, biotite and quartz phenocrysts in the Bukadaban rhyolite (sample 2509, ppl). Ab, albite; Bt, biotite; Kf, potassium feldspar, Mus, muscovite; Pl, plagioclase; Q, quartz; Tm, tourmaline.

The Hudongliang tourmaline-bearing two-mica rhyolites comprise potassium feldspar, albite, biotite, quartz, muscovite, and tourmaline phenocrysts, and similar microlitic minerals in the groundmass along with cryptocrystalline–glassy materials (Fig. 2c and d). The Bukadaban biotite rhyolites are composed of potassium feldspar, plagioclase, biotite and quartz phenocrysts, and groundmass microlitic minerals similar to the phenocrysts in addition to cryptocrystalline–glassy materials (Fig. 2e and f).

ANALYTICAL METHODS

Mineral composition analyses

All silicate mineral analyses were carried out at the State Key Laboratory of Isotope Geochemistry (SKLIG), Guangzhou Institute of Geochemistry (GIG), Chinese Academy of Sciences (CAS) with a JEOL JXA-8100 Superprobe. Operating conditions were as follows: 15 kV accelerating voltage, 20 nA beam current, 1–2 µm beam diameter, 10 s counting time and ZAF correction procedure for data reduction. The analytical procedures were described in detail by Huang *et al.* (2007).

^{40}Ar–^{39}Ar age dating

Argon isotope analyses were conducted on a GV-5400 mass spectrometer at the SKLIG GIG CAS. Whole-rock chips of 30–60 mesh (1 mesh = 0·254 mm) in size and mineral separates (potassium feldspar and biotite) were ultrasonically cleaned first in distilled water with <5% HNO_3 and then in deionized water, and then dried and handpicked to remove visible contamination. The sample and a monitor standard (ZBH-2506 with an age of 132·500 ± 0·663 Ma) were irradiated in the 49-2 reactor in Beijing for 54 h. Details of the analytical procedure used have been given by Qiu (2006) and Qiu & Jiang (2007). The ^{40}Ar–^{39}Ar dating results are calculated and plotted using the ArArCALC software of Koppers (2002).

Zircon U–Pb age dating

Zircons were separated using conventional heavy liquid and magnetic separation techniques. Cathodoluminescence (CL) images were obtained for zircons prior to analysis, using a JEOL JXA-8100 Superprobe at the SKLIG GIG CAS, to characterize the internal structures and choose potential target sites for U–Pb dating.

CASIMS (Cameca IMS-1280 SIMS) method

CASIMS zircon U–Pb analyses were conducted by secondary ion mass spectrometry (SIMS) using the Cameca IMS-1280 system at the Institute of Geology and Geophysics, CAS. Analytical procedures are the same as those described by Li *et al.* (2009). The O_2^- primary ion beam with an intensity of *c.* 10 nA was accelerated at −13 kV. The ellipsoidal spot is about 20 µm × 30 µm in size. The aperture illumination mode (Kohler illumination) was used with a 200 µm primary beam mass filter (PBMF) aperture to produce even sputtering over the entire analyzed area. In the secondary ion beam optics, a 60 eV energy window was used, together with a mass resolution of *c.* 5400. Rectangular lenses were activated in the secondary ion optics to increase the transmission at high mass resolution. A single electron multiplier was used in ion-counting mode to measure secondary ion beam intensities by the peak jumping sequence: 196 ($^{90}Zr_2{}^{16}O$, matrix reference), 200 ($^{92}Zr_2{}^{16}O$), 200·5 (background), 203·81 ($^{94}Zr_2{}^{16}O$, for mass calibration), 203·97 (Pb), 206 (Pb), 207 (Pb), 208 (Pb), 209 ($^{177}Hf^{16}O_2$), 238 (U), 248 ($^{232}Th^{16}O$), 270 ($^{238}U^{16}O_2$), and 270·1 (reference mass), 1·04, 0·56, 4·16, 0·56, 6·24, 4·16, 6·24, 2·08, 1·04, 2·08, 2·08, 2·08, and 0·24 s, respectively. Each measurement consisted of seven cycles, and the total analytical time is *c.* 12 min.

Calibration of Pb/U ratios is relative to the standard zircon TEMORA 2 (417 Ma) (Black *et al.*, 2004) based on an observed linear relationship between $\ln(^{206}Pb/^{238}U)$ and $\ln(^{238}U^{16}O_2/^{238}U)$ (Whitehouse *et al.*, 1997). U and Th concentrations of unknowns were determined relative to the standard zircon 91500 with Th and U concentrations of *c.* 29 and 81 ppm respectively (Wiedenbeck *et al.*, 1995). Measured compositions were corrected for common Pb using non-radiogenic ^{204}Pb. Common Pb is very low, and is largely derived from laboratory contamination introduced during sample preparation (Ireland & Williams, 2003). An average of present-day crustal composition (Stacey & Kramers, 1975) is used for the common Pb. Uncertainties on single analyses are reported at the 1σ level; mean ages for pooled U–Pb analyses are quoted with a 95% confidence interval. Data reduction was carried out using the Isoplot/Ex v. 2.49 program (Ludwig, 2003).

LAM-ICP-MS method

Laser ablation inductively coupled plasma mass spectrometry (LA-ICP-MS) zircon U–Pb analyses were conducted on an Agilent 7500 ICP-MS system equipped with a 193 nm laser, housed at the National Key Laboratory of Geological Processes and Mineral Resources, Faculty of Earth Sciences, China University of Geosciences (Wuhan), and the SKLIG GIG CAS, respectively. Zircon U–Pb ages and trace element contents were analysed synchronously at the SKLIG GIG CAS. Zircon 91500 was used as the standard and the standard silicate glass NIST 610 was used to optimize the machine, with a beam diameter of 30 µm. Raw count rates for ^{29}Si, ^{204}Pb, ^{206}Pb, ^{207}Pb, ^{208}Pb, ^{232}Th and ^{238}U were collected and U, Th and Pb concentrations were calibrated using ^{29}Si as the internal calibrant and NIST 610 as the reference material. $^{207}Pb/^{206}Pb$ and $^{206}Pb/^{238}U$ ratios were calculated using the GLITTER software (Jackson *et al.*, 2004). Measured $^{207}Pb/^{206}Pb$, $^{206}Pb/^{238}U$ and $^{208}Pb/^{232}Th$ ratios in zircon

91500 were averaged over the course of the analytical session and used to calculate correction factors. These correction factors were then applied to each sample to correct for both instrumental mass bias and depth-dependent elemental and isotopic fractionation. Further detailed descriptions of the instrumentation and analytical procedure for the LA-ICP-MS zircon U–Pb and trace element technique have been given by Gao *et al.* (2002) and Liu *et al.* (2008, 2010). The age calculations and plots were made using Isoplot (version 3.00) (Liu *et al.*, 2010).

Element and Nd–Sr–Pb isotope analyses

After crushing, unweathered rock fractions were selected and subjected to ultrasonic cleaning in distilled water with <5% HNO_3 and distilled water, dried and hand-picked to remove visible contamination, and then pulverized.

Major element oxides (wt %) for whole-rock powders were determined by inductively coupled plasma atomic emission spectrometry (ICP-AES) using a Varian Vista PRO system at the SKLIG GIG CAS and the Hubei Institute of Geology and Mineral Resource (HIGMR), using wavelength X-ray fluorescence spectrometry with analytical errors better than 2%. The FeO contents of some samples were analyzed by conventional volumetric methods at the HIGMR. Details of the analytical procedures at the SKLIG GIG CAS and HIGMR were described by Li *et al.* (2002) and Gao *et al.* (1995), respectively. Trace elements, including the rare earth elements (REE), were analyzed using a Perkin-Elmer ELAN 6000 inductively coupled plasma source mass spectrometer (ICP-MS) at the SKLIG GIG CAS, following procedures described by Li *et al.* (2002). Analytical precision for most elements is better than 3%.

Sr and Nd isotope compositions of selected samples were determined by ICP-MS using a Micromass Isoprobe multi-collector (MC)-ICP-MS system at the SKLIG GIG CAS. Analytical procedures are similar to those described by Li *et al.* (2006). The $^{87}Sr/^{86}Sr$ ratio of the NBS987 standard and $^{143}Nd/^{144}Nd$ ratio of the Shin Etsu JNdi-1 standard measured were 0·710288 ±28 (2σm) and 0·512109 ±12 (2σm), respectively. All measured $^{143}Nd/^{144}Nd$ and $^{86}Sr/^{88}Sr$ ratios are fractionation corrected to $^{146}Nd/^{144}Nd = 0·7219$ and $^{86}Sr/^{88}Sr = 0·1194$, respectively.

For Pb isotope determinations, about 100 mg powder was weighed into a Teflon beaker, spiked and dissolved in concentrated HF at 180°C for 7 h. Lead was separated and purified by conventional cation-exchange techniques (AG1X 8, 200–400 resin) with diluted HBr as an eluant. Total procedural blanks were less than 50 pg Pb. Isotopic ratios were measured using a VG-354 mass spectrometer at the SKLIG GIG CAS following procedures described by Zhu *et al.* (2001). Repeated analyses of SRM 981 yielded average values of $^{206}Pb/^{204}Pb = 16·9 ±4 (2σ)$, $^{207}Pb/^{204}Pb = 15·498 ±4 (2σ)$ and $^{208}Pb/^{204}Pb = 36·728 ±9 (2σ)$.

In situ zircon Hf isotope analyses were carried out at the SKLIG GIG CAS by MC-ICP-MS using a Neptune system equipped with a Geolas-193 laser ablation system. During analyses, spot sizes of 32 and 63 μm and a laser repetition rate of 10 Hz with 100 mJ were used. Details of the technique have been given by Wu *et al.* (2006). During analyses, the $^{176}Hf/^{177}Hf$ ratio of standard zircon (Penglai zircon megacrysts) was 0·282900 ±2 (2σ, *n* = 488), similar to the recommended $^{176}Hf/^{177}Hf$ ratio of ~0·282906 (Li *et al.*, 2010).

RESULTS

Mineral chemistry

Mineral major element compositions are listed in Tables 2–5 and the chemical characteristics of selected minerals are presented in Fig. 3. Biotite spot analyses for the Hudongliang rhyolites plot in the biotite field of peraluminous granites (S-type granites) (Abdel Rahman, 1994) (Fig. 3a and b). Biotite compositions in the Bukadaban rhyolites mainly plot near the boundary between the fields of biotites from peraluminous granites (S-type granites) and metaluminous calc-alkaline granite suites (I-type granites). Biotites in the southern Malanshan rhyolitic porphyry mainly plot in the biotite field of the metaluminous calc-alkaline granites suite (I-type granites), although a minority are comparable with biotites in peraluminous granites (S-type granites) (Fig. 3a and b). The biotites in the southern Malanshan and Bukadaban rhyolitic rocks have higher MgO but lower Fe/(Fe + Mg) values than those of the Hudongliang rocks (Fig. 3c). Muscovites in the Hudongliang rhyolites are primary rather than alteration products, based on their high Ti and Na and low Mg (Miller *et al.*, 1981) (Fig. 3d). Tourmaline in these rhyolites exhibits high Al_2O_3 (32·97–34·57 wt %) and FeO (10·99–12·44 wt %) and low MgO (1·67–2·83 wt %) (Table 5), corresponding to schörl. The Hudongliang rhyolites contain albite and sanidine whereas the southern Malanshan and Bukadaban rhyolitic rocks contain sanidine, oligoclase and andesine but no albite (Fig. 3e).

Zircon LA-ICP-MS trace element data are presented in Table 6. Most analysed zircon crystals from the rhyolites exhibit clear oscillatory zoning, indicating their magmatic origin. The chondrite-normalized rare earth element (REE) patterns for zircons of the Southern Malanshan rhyolite are enriched in heavy rare earth elements (HREE) ($Lu_n/Sm_n = 14–237$), and have distinct positive Ce anomalies and negative Eu anomalies (Eu/Eu* = 0·04–0·43) (Fig. 4a; Table 6). The REE patterns for zircons of the Bukadaban and Hudongliang rhyolites exhibit similar positive Ce anomalies and negative Eu anomalies (Eu/Eu* = 0·01–0·07), but are variable in terms of their HREE abundances ($Lu_n/Sm_n = 2–181$) (Fig. 4b; Table 6). Some Hudongliang rhyolite zircons display higher HREE contents (Yb = 778–993 ppm,

Table 2: Biotite compositions in the Bukadaban–Malanshan rhyolites

Sample	SiO_2	TiO_2	Al_2O_3	FeO	MgO	CaO	Na_2O	K_2O	F	Cl	Total
$1P_2JD7$-1	33·13	2·12	18·66	21·99	3·69	0·06	0·62	9·33	2·48	0·14	92·22
$1P_2JD7$-1	34·65	2·2	19·17	22·96	3·73	0·02	0·61	9·24	2·68	0·16	95·42
$1P_2JD7$-1	34·41	2·39	19·13	22·07	3·85	0·01	0·71	9·44	3·07	0·07	95·15
$1P_2JD7$-1	34·36	1·89	20·37	23·26	3·41	b.d.	0·52	7·73	3·68	0·07	95·29
$1P_2JD7$-1	35·18	2·13	18·32	21·76	4·64	b.d.	0·48	9·45	2·5	0·09	94·55
$1P_2JD7$-1	34·87	2·02	19·06	23·11	3·8	0·03	0·54	9·02	3·1	0·14	95·69
$1P_2JD7$-1	35·02	2·2	19·56	23·72	3·85	0·02	0·59	9·25	2·84	0·03	97·08
2303	34·57	3·63	16·71	21·78	7·65	0·01	0·39	9·42	3·71	0·25	98·12
2303	34·19	3·75	13·86	13·59	8·57	0·09	0·57	9·48	3·49	0·29	87·88
2303	34·88	3·79	16·6	20·59	8·15	0·02	0·51	9·39	3·39	0·17	97·49
2303	34·11	4·05	14·93	15·53	8·23	0·15	0·41	9·41	3·26	0·25	90·33
2303	34·19	3·62	15·51	23·83	8·75	b.d.	0·52	9·04	3·11	0·11	98·68
2303	36·1	4·23	15·59	19·42	8·07	0·06	0·67	9·41	3·13	0·13	96·81
2303	35·76	1·31	13·93	12·08	9·09	0·32	0·15	7·13	3·55	0·22	83·54
2303	32·81	3·86	14·89	18·95	7·87	0·01	0·42	8·89	3·2	0·15	91·05
2303	35·5	3·39	17·29	20·81	8·74	b.d.	0·51	9·7	2·84	0·26	99·04
2303	35·08	4·03	15·97	20·28	8·78	b.d.	0·33	9·51	3·49	0·22	97·69
2303	36·48	4·27	16·08	17·54	8·22	0·07	0·52	9·46	3·35	0·14	96·13
2509	32·31	4·1	17·92	25·15	6·48	0·01	0·45	7·6	2·24	0·28	96·54
2509	37·1	3·69	18·81	16·67	6·1	0·06	0·6	9·52	2·72	0·31	95·58
2509	38·46	2·68	18·04	14·71	9·52	0·03	0·31	9·75	4·36	0·23	98·09
2509	38·43	2·51	17·81	13·91	9·96	0·03	0·37	9·86	4·76	0·18	97·82
2509	40·44	2·35	19·31	10·82	10·15	b.d.	0·36	10·48	4·51	0·11	98·53
2509	36·83	4·32	17·17	17·35	8·28	0·01	0·19	9·97	3·72	0·21	98·05

Mineral composition analyses were carried out on a JEOL JXA-8100 Superprobe, State Key Laboratory of Isotope Geochemistry, Guangzhou Institute of Geochemistry, Chinese Academy of Sciences. b.d., below detection.

Lu = 133–171 ppm) than zircons from the Southern Malanshan and Bukadaban rhyolites (Yb = 15·7–606 ppm, Lu = 2·2–112 ppm) but all the rhyolite zircons plot in or near the field of zircons derived from continental crust (Grimes *et al*., 2007) (Fig. 4d).

Geochronology

Tables 1 and 7–10 report $^{40}Ar/^{39}Ar$, CASIMS and LA-ICP-MS zircon U–Pb age data. The southern Malanshan rhyolitic porphyry sample 2303 yielded whole-rock $^{40}Ar/^{39}Ar$ weighted mean and normal and inverse isochron ages of 7·24 ± 0·08, 7·24 ± 0·66 and 7·24 ± 0·63 Ma, respectively (Fig. 5a_1–a_3; Table 7). However, zircon U–Pb analyses for the same sample show that it contains zircon crystals with variable $^{206}Pb/^{238}U$ (780–8·6 Ma) or $^{207}Pb/^{206}Pb$ (2514–1836 Ma) ages (Tables 8–10). Moroever, LA-ICP-MS U–Pb analyses for the young (<10·0 Ma) zircons in two different laboratories yielded consistent weighted mean $^{206}Pb/^{238}U$ ages of 9·06 ± 0·19 and 9·05 ± 0·34 Ma, respectively (Fig. 6a_1 and a_2). CASIMS U–Pb analyses for young zircons also gave consistent lower intercept and weighted mean $^{206}Pb/^{238}U$ ages of 8·97 ± 0·25 and 9·04 ± 0·25, respectively (Fig. 6a_3). Thus, all the youngest zircon grains yielded a consistent $^{206}Pb/^{238}U$ age of ~9·0 Ma. We suggest that the ~9·0 Ma zircon U–Pb age can be interpreted as the best estimate of the crystallization age of the southern Malanshan rhyolitic porphyries, and that zircons with older ages have been inherited from the porphyry source rocks or entrained from the wall-rocks during magma ascent. Accordingly, the ~7·24 Ma whole-rock $^{40}Ar/^{39}Ar$ age corresponds to the cooling age of the subvolcanic rocks.

The Hudongliang rhyolite sample $1P_2JD7$-1 yielded whole-rock $^{40}Ar/^{39}Ar$ normal and inverse isochron ages of 3·09 ± 0·23, 3·10 ± 0·23, respectively (Fig. 5b_2–b_3), and a biotite weighted plateau age of 2·94 ± 0·07 Ma (Fig. 5c_1). However, zircon U–Pb analyses for the same sample

Table 3: Muscovite compositions in sample 1P$_2$JD7-1

SiO_2	TiO_2	Al_2O_3	FeO	MgO	CaO	Na_2O	K_2O	F	Cl	Total
45·77	0·62	32·41	2·30	0·94	0·03	0·95	10·44	3·15		96·61
43·84	0·57	31·44	3·12	0·92	0·1	0·97	10·21	3·29	0·03	94·49
45·85	0·73	32·23	2·09	0·88	0·01	0·96	10·49	2·86	0·08	96·18
44·08	0·7	33·67	2·07	0·88	0·12	0·78	10·01	3·1	0·05	95·46
44·78	0·68	30·19	2·21	0·84	0·57	0·82	9·76	2·85		92·7
45·56	0·7	32·74	2·41	0·77	0·03	0·85	10·54	2·97	0·03	96·6
45·18	0·75	32·63	2·03	0·9	0·01	0·8	10·6	2·76		95·66

Mineral composition analyses were conducted on a JEOL JXA-8100 Superprobe, State Key Laboratory of Isotope Geochemistry, Guangzhou Institute of Geochemistry, Chinese Academy of Sciences.

Table 4: Feldspar compositions in the Bukadaban–Malanshan rhyolites

Sample	SiO_2	TiO_2	Al_2O_3	FeO	MgO	CaO	Na_2O	K_2O	Total
1P$_2$JD7-1	64·84	0·00	18·35	0·03	0·00	0·06	3·45	12·41	99·14
1P$_2$JD7-1	65·54	0·00	20·87	0	0·01	2·15	10·2	0·84	99·61
1P$_2$JD7-1	65·1	0·00	18·26	0·02	0·00	0·03	3·44	12·59	99·44
1P$_2$JD7-1	66·12	0·00	19·88	0·03	0·00	1·48	10·43	1·00	98·94
1P$_2$JD7-1	65·84	0·00	20·57	0·04	0·00	1·67	10·04	1·03	99·19
1P$_2$JD7-1	65·55	0·00	21	0·02	0·00	2·19	9·68	0·93	99·37
1P$_2$JD7-1	63·94	0·00	17·54	0	0·00	0·05	3·49	12·69	97·71
1P$_2$JD7-1	66·21	0·01	20·66	0	0·00	1·77	10·49	1·00	100·14
2303	64·36	0·05	18·23	0·03	0·00	0·3	3·85	10·94	97·76
2303	62·11	0·00	22·97	0·05	0·00	5·19	8·2	1·01	99·53
2303	60·33	0·05	22·93	0·12	0·04	4·85	7·61	1·06	96·99
2303	64·9	0·00	18·45	0·04	0·00	0·27	3·91	11·07	98·64
2303	60·63	0·00	23·98	0·01	0·00	6·29	7·9	0·81	99·62
2303	61·27	0·00	23·43	0·03	0·00	5·84	7·74	1·04	99·35
2303	60·37	0·05	24·46	0·07	0·00	6·84	7·48	0·79	100·06
2303	58·85	0·00	25·04	0·04	0·01	7·48	7·03	0·76	99·21
2303	61·21	0·01	23·92	0·03	0·00	6·1	7·58	0·97	99·82
2303	65·17	0·00	18·59	0	0·00	0·26	3·81	11·67	99·5
2509	61·77	0·07	23·25	0·03	0·00	5·26	8·29	0·94	99·61
2509	65·43	0·00	18·53	0	0·00	0·26	4·38	10·9	99·5
2509	65·19	0·00	18·45	0·01	0·00	0·2	3·61	11·97	99·43
2509	61·48	0·04	23·37	0·01	0·01	5·4	8·05	0·97	99·33
2509	66·05	0·04	18·64	0·03	0·00	0·33	4·7	10·2	99·99
2509	65·53	0·00	18·54	0	0·00	0·3	4·54	10·85	99·76
2509	61·69	0·03	23·44	0·04	0·00	5·35	8·05	0·92	99·52
2509	65·48	0·04	18·41	0	0·00	0·22	3·2	12·47	99·82
2509	61·84	0·00	23·47	0·02	0·00	5·33	7·93	0·95	99·54

Mineral composition analyses were carried out on a JEOL JXA-8100 Superprobe, State Key Laboratory of Isotope Geochemistry, Guangzhou Institute of Geochemistry, Chinese Academy of Sciences.

Table 5: Tourmaline compositions in sample 1P$_2$JD7-1

SiO_2	TiO_2	Al_2O_3	FeO	MgO	CaO	Na_2O	K_2O	F	Cl	Total
35·04	0·60	33·40	11·77	2·36	0·23	1·98	0·06	0·28		85·60
35·28	0·66	33·44	10·99	2·83	0·29	1·96	0·07	0·56	0·078	85·90
35·05	0·74	32·97	11·64	2·48	0·24	2·23	0·04	0·38		85·59
36·57	0·20	34·57	11·93	1·67	0·04	1·67	0·04	0·20		86·79
35·45	0·58	33·67	12·44	2·40	0·18	2·18	0·04	0·58		87·28
35·86	0·72	33·28	11·63	2·62	0·23	2·00	0·04	0·36		86·58

Mineral composition analyses were conducted on a JEOL JXA-8100 Superprobe, State Key Laboratory of Isotope Geochemistry, Guangzhou Institute of Geochemistry, Chinese Academy of Sciences.

revealed zircon crystals with variable $^{206}Pb/^{238}U$ (967–2·7 Ma) ages (Tables 8–10). Moreover, LA-ICP-MS U–Pb analyses for the young (<4·0 Ma) zircon crystals consistently yielded lower intercept and weighted mean $^{206}Pb/^{238}U$ ages of 3·04 ± 0·04 and 3·07 ± 0·04 Ma, respectively (Fig. 6b$_1$). CASIMS U–Pb analyses for the young zircons gave consistent lower intercept and weighted mean $^{206}Pb/^{238}U$ ages of 3·11 ± 0·09 and 3·14 ± 0·05, respectively (Fig. 6b$_2$). Both $^{40}Ar/^{39}Ar$ and zircon U–Pb analyses suggest that the Hudongliang rhyolites crystallized at ~3·0 Ma. Zircons with ages greater than ~4·0 Ma were either inherited from the rhyolite source rocks or derived from the wall-rocks during magma ascent.

The Bukadaban rhyolite sample 2509 yielded whole–rock $^{40}Ar/^{39}Ar$ weighted mean and normal and inverse isochron ages of 1·72 ± 0·04, 1·68 ± 0·08 and 1·74 ± 0·06 Ma, respectively (Fig. 5d$_1$–d$_3$), and a potassium feldspar normal and inverse isochron age of 1·38 ± 0·17 and 1·46 ± 0·14 Ma (Fig. 5e$_2$–e$_3$; Table 7). Zircon U–Pb analyses for the same sample showed that most of the zircons have $^{206}Pb/^{238}U$ age ranging from 10·0 to 1·45 Ma, with the exception of two crystals with $^{206}Pb/^{238}U$ ages of 802 and 228 Ma (Tables 8–10). LA-ICP-MS U–Pb analyses of the young (<2·0 Ma) zircon crystals in two different laboratories yielded consistent weighted mean $^{206}Pb/^{238}U$ ages of 1·55 ± 0·03 and 1·54 ± 0·07 Ma, respectively (Fig. 6c$_1$–c$_2$). Likewise, CASIMS U–Pb analyses for the young (<2·0 Ma) zircons also gave consistent lower intercept and weighted mean $^{206}Pb/^{238}U$ ages of 1·56 ± 0·02 and 1·55 ± 0·02 Ma, respectively (Fig. 6c$_3$). Both the $^{40}Ar/^{39}Ar$ and zircon U–Pb analyses suggest that the Bukadaban rhyolites were generated in the Early Quaternary Period. The slightly older whole–rock $^{40}Ar/^{39}Ar$ age may be affected by excess argon; however, the younger potassium feldspar $^{40}Ar/^{39}Ar$ age is consistent with the ~1·5 Ma zircon U–Pb age, within error limits. We suggest that ~1·5 Ma should be interpreted as the best estimate of the formation age for the Bukadaban rhyolites, and that zircons with ages greater than ~2·0 Ma are probably inherited from the magma source rocks or derived from the wall-rocks during magma ascent.

Our $^{40}Ar/^{39}Ar$ and zircon U–Pb age results indicate that the southern Malanshan, Hudongliang and Bukadaban rhyolites erupted at ~9·0, 3·0 and 1·5 Ma, respectively (Figs 5 and 6; Table 1). In addition to the young (9·0–1·5 Ma) magmatic zircons, the rhyolites contain a number of older (>200 Ma) inherited or xenocrystic zircon grains with ages clustering in the Late Archean (~2500 Ma), early Proterozoic (1900–1800 Ma), Neoproterozoic (900–700 Ma) and Paleozoic–Early Mesozoic (400–200 Ma) (Fig. 7). The age spectrum is in accord with those of detrital zircons from the Triassic Songpan–Ganzi sedimentary complex (Bruguier *et al.*, 1997; Weislogel *et al.*, 2006).

Whole-rock major and trace elements geochemistry

Major (wt %) and trace (ppm) element data for the rhyolites are provided in Table 11. Along with the Ulugh Muztagh and Weixueshan rocks, the Bukadaban–Malanshan (BM) rhyolites exhibit high SiO_2 contents (69–76 wt %) and very low Mg# [$= 100Mg^{2+}/(Mg^{2+} + Fe^{2+})$] (4–35) and plot entirely in the field of rhyolites in a SiO_2 vs $K_2O + Na_2O$ diagram (Fig. 8a; Table 11). They are strongly peraluminous {$[Al_2O_3/(Na_2O + K_2O + CaO)]_{molar} = 1{\cdot}13–1{\cdot}40$} (Fig. 8b; Table 11) and high-K calc-alkaline, and plot in the field of 'syn-collisional granites', with overall geochemical characteristics comparable with those of Himalayan leucogranites (Fig. 8c and d). The BM rocks are marked by enrichment in light rare earth elements (LREE), depletion in HREE and Y (4·0–9·8 ppm), and negative anomalies in Eu, Ba and Sr, similar to the Ulugh Muztagh leucogranites and rhyolites and the Himalayan leucogranites (Fig. 9a and b; Table 11). They are similar to upper (continental) crust and Himalayan leucogranites (Fig. 10a and b) in terms of their low Nb/Ta ratios (<10) and high Th/La (1·0–1·3) values (Table 11), but have higher and more

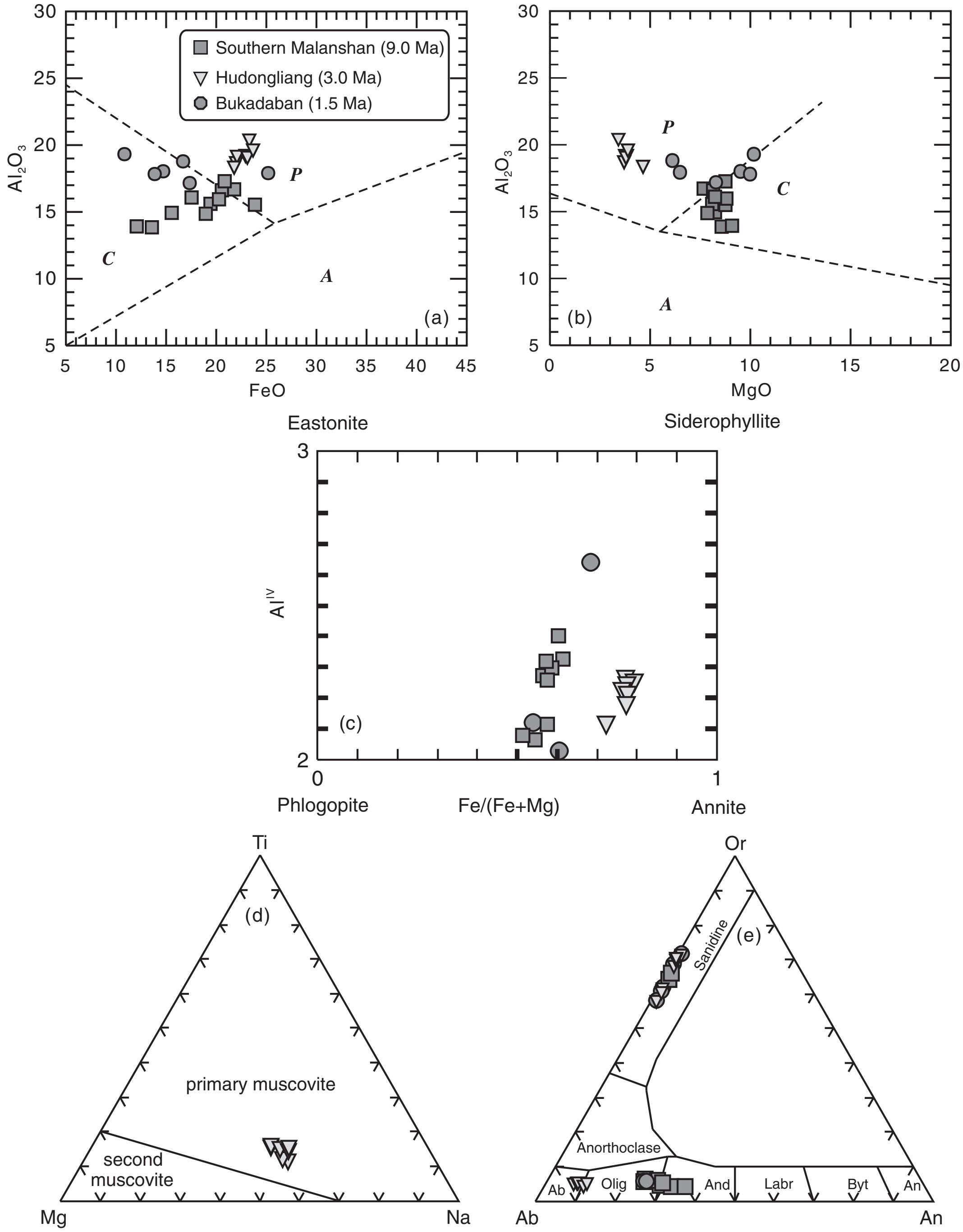

Fig. 3. Chemical characteristics of phenocryst minerals in the Bukadaban–Malanshan rhyolitic rocks. (a, b) FeO–Al_2O_3–MgO diagrams for biotite classification (after Abdel Rahman, 1994). A, biotite in anorogenic alkaline suites; P, biotite in peraluminous granites (S-type granites); C, biotite in metaluminous calc-alkaline granite suites (I-type granites). (c) Al^{IV} vs Fe/(Fe + Mg) diagram for biotite. (d) Ternary Mg–Ti–Na classification diagram for muscovite; primary and secondary muscovite fields from Miller *et al*. (1981). (e) Ab–Or–An diagram for feldspar. Ab, albite; Or, orthoclase; An, anorthite; Olig, oligoclase; And, andesine; Labr, labradorite; Byt, bytownite.

variable Th (12·0–103 ppm) contents. However, the southern Malanshan and Bukadaban biotite rhyolites have slightly higher LREE contents, TiO_2, MgO, FeO^{total} (= FeO + $Fe_2O_3 \times 0{\cdot}9$) than the Hudongliang rhyolites, Ulugh Muztagh leucogranites and rhyolites or the Himalayan leucogranites (Fig. 9a and b; Table 11), and slightly lower Rb/Sr ratios (4–20) than those (15–137) of the Hudongliang rhyolites (Table 11).

Table 6: LA-ICP-MS trace element data for zircons from the Bukadaban–Malanshan rhyolites

Sample:	2303									
Sample spot:	1	2	3	4	5	6	7	9	10	11
wt %										
SiO_2	32·7	32·7	32·7	32·7	32·7	32·7	32·7	32·7	32·7	32·7
ppm										
P	310	174	230	245	209	117	326	350	187	471
Ti	12·5	18·0	18·8	20·4	16·6	60·5	18·8	10·3	15·6	9·82
Y	1058	460	822	565	822	344	701	515	343	739
Nb	1·84	1·36	1·65	1·36	2·54	1·45	1·46	0·89	1·73	1·18
La	0·36	0·04	0·24	0·05	0·06	0·16	5·03	0·01	0·44	0·04
Ce	19·9	17·3	19·4	6·68	17·9	11·0	28·6	8·25	18·8	2·26
Pr	0·53	0·26	0·56	0·32	0·42	0·20	1·76	0·12	0·20	0·17
Nd	7·49	3·99	7·25	5·07	6·16	3·03	11·4	1·98	2·04	2·95
Sm	9·82	5·52	8·52	6·61	7·86	3·63	8·64	3·09	2·93	6·46
Eu	1·35	1·13	1·41	0·74	1·30	0·59	1·49	0·53	0·53	0·16
Gd	34·3	18·1	30·0	22·2	28·0	13·5	28·4	10·7	11·7	22·5
Tb	9·99	4·78	8·50	6·01	8·19	3·51	7·46	3·73	3·31	6·95
Dy	100	46·8	82·5	59·1	81·3	35·9	74·0	42·3	34·0	73·5
Ho	33·4	15·1	27·1	18·9	27·2	12·4	23·9	16·1	11·5	24·5
Er	140	60·9	109	77·4	115	46·2	95·3	80·0	47·3	106
Tm	29·1	11·8	21·5	15·4	23·3	9·22	18·6	18·8	9·63	23·3
Yb	263	104	192	136	208	82·1	163	192	85·4	221
Lu	51·5	20·4	36·9	27·0	39·8	15·9	31·3	39·4	16·8	42·7
Hf	10181	7964	7010	8449	8489	6255	8900	9561	8754	10344
Ta	0·94	0·54	0·69	0·64	1·08	0·57	0·68	0·87	0·69	0·73
Pb	1·68	0·38	1·37	0·64	1·52	2·30	0·61	1·434	0·69	2·18
Th	418	173	367	170	300	141	308	60·4	184	231
U	975	177	549	319	853	189	270	922	206	1460
Age (Ma)*	9·0	8·7	9·4	8·7	9·0	26·2	9·0	8·8	11·4	8·8
$T_{Zr\text{-}Ti}$ (°C)†	840	882	887	897	873	1050	888	819	865	814
1σ (°C)	30	32	32	33	32	39	32	30	31	29

Sample:	2303		$1P_2JD7$-1				2509	
Sample spot:	12	13	3	4	7	8	1	2
wt %								
SiO_2	32·7	32·7	32·7	32·7	32·7	32·7	32·7	32·7
ppm								
P	659	202	406	2168	714	2614	234	252
Ti	3·84	19·6	4·40	6·42	8·77	5·34	25·0	20·3
Y	1286	664	614	3573	1343	4263	331	226
Nb	3·82	1·29	1·79	9·80	4·09	4·62	2·24	0·48
La	0·43	1·12	0·06	0·20	0·02	0·10	0·04	0·02
Ce	11·7	31·7	1·22	1·50	5·68	0·73	9·56	4·06
Pr	0·16	0·89	0·093	0·11	0·12	0·13	0·32	0·19
Nd	1·03	10·8	1·34	1·31	2·27	1·37	6·0	4·5
Sm	2·54	10·9	3·52	6·47	6·38	5·68	9·9	7·1
Eu	0·44	2·64	0·022	0·19	0·12	0·18	0·23	0·18
Gd	16·9	32·6	21·4	50·9	35·5	53·0	27·7	21·7
Tb	7·12	8·14	7·48	26·2	13·9	28·5	6·07	4·91
Dy	97·8	74·3	69·8	333	143	375	47·4	34·2
Ho	39·8	22·5	18·5	107	38·1	125	10·6	7·42
Er	200	87·2	60·1	437	138	531	30·3	19·3
Tm	47·9	16·1	9·73	88·9	26·4	112	4·04	2·58
Yb	488	142	69·3	778	212	993	25·7	15·7
Lu	100	25·7	10·4	133	34·4	171	3·59	2·20
Hf	9229	6793	10482	12371	13013	12614	10263	11297
Ta	1·84	0·50	0·64	9·25	2·67	3·89	0·62	0·14
Pb	12·78	0·44	0·70	7·97	2·27	5·98	0·14	0·31
Th	107	249	89·9	250	184	162	260	177
U	1677	151	1068	18575	3815	15249	311	214
Age (Ma)*	51·9	9·1	3·0	3·0	3·0	3·0	1·59	5·87
$T_{Zr\text{-}Ti}$ (°C)†	722	892	770	802	752	734	924	897
1σ (°C)	26	32	35	37	34	33	43	42

(continued)

Table 6: Continued

Sample:	2509								
Sample spot:	3	4	5	6	7	8	9	10	11
wt %									
SiO_2	32·7	32·7	32·7	32·7	32·7	32·7	32·7	32·7	32·7
ppm									
P	7								
11	535	1398	228	1128	1154	766	180	1118	
Ti	15·8	63·1	9·80	14·3	10·6	6·17	4·36	19·1	4·41
Y	1561	704	2181	457	2187	1716	1018	233	1490
Nb	1·38	1·34	4·18	0·63	3·13	1·41	0·95	0·80	1·42
La	0·08	0·00	3·78	0·18	0·16	0·09	0·01	0·12	0·13
Ce	5·58	0·35	6·79	6·71	0·00	0·52	0·28	8·40	0·90
Pr	0·83	0·009	0·81	0·49	0·29	0·04	0·03	0·39	0·03
Nd	13·3	0·459	4·0	7·9	2·15	1·18	0·52	7·63	1·79
Sm	24·4	2·190	5·9	12·7	6·43	4·99	2·42	10·3	4·50
Eu	0·31	0·076	0·04	0·38	0·14	0·11	0·07	0·38	0·14
Gd	80·7	17·0	33·1	34·2	41·6	34·5	18·6	27·2	28·5
Tb	20·3	7·38	15·7	7·51	18·7	14·6	8·52	5·25	12·5
Dy	180	74·2	188	59·1	206	163·0	92·0	36·0	137
Ho	50·3	20·5	63·0	15·4	66·3	51·7	30·3	7·81	44·1
Er	181·6	72·9	289	53·2	277·4	217·5	133·6	21·9	188·3
Tm	32·2	12·8	65·8	9·40	58·7	46·6	28·3	3·32	39·6
Yb	257	109	606	77·8	521	427	258	23·4	361
Lu	45·4	19·3	112	13·5	94·2	77·2	47·3	3·52	65·9
Hf	11440	12197	12798	12084	14065	13988	11075	9408	11361
Ta	0·46	1·08	2·91	0·26	2·28	1·27	0·94	0·17	1·18
Pb	1·34	2·32	2·72	0·63	1·24	1·04	0·61	0·17	1·34
Th	701	35	268	425	157	104	62·2	168	86·8
U	1394	1750	9035	555	4232	3523	2222	140	2787
Age (Ma)*	5·06	7·86	1·47	5·89	1·52	1·58	1·46	5·42	1·64
$T_{Zr\text{-}Ti}$ (°C)†	867	1057	813	855	822	766	733	889	734
1σ (°C)	40	50	37	39	38	35	33	41	33

LA-ICP-MS zircon trace element analyses were carried out on an Agilent 7500 ICP-MS system equipped with a 193 nm laser, housed at the State Key Laboratory of Isotope Geochemistry, Guangzhou Institute of Geochemistry, Chinese Academy of Sciences.
*Age ($^{206}Pb/^{238}U$) data for samples 2303 and 2509 are from Table 10. Age ($^{206}Pb/^{238}U$) data for samples $1P_2JD7$-1 are from Table 8.
†*T*, temperature based on titanium-in-zircon thermometer (Ferry & Watson, 2007).

Nd–Sr–Pb–Hf isotope compositions

The whole-rock Nd–Sr–Pb isotope data for the BM rhyolites are reported in Table 11. The BM and Ulugh Muztagh/Weixueshan strongly peraluminous rocks have lower εNd (–5·8 to –8·6) and $^{143}Nd/^{144}Nd$ (0·512199–0·512338) and higher $^{87}Sr/^{86}Sr$ (0·7125–0·7178) than other Cenozoic magmatic rocks in northern Tibet, but show isotopic similarities to marine sediments and Proterozoic–Triassic sedimentary rocks in the Songpan–Ganzi Block (Figs 10c, d and 11a, b; Table 11). In detail, the BM rhyolites have higher $^{143}Nd/^{144}Nd$ and lower $^{87}Sr/^{86}Sr$ than the Himalayan leucogranites [0·511693–0·511906 and 0·7240–0·7973, respectively (e.g. Zhang *et al.*, 2004; Guo & Wilson, 2012)]. The ranges of Pb isotope compositions ($^{206}Pb/^{204}Pb$ 18·59–18·70; $^{207}Pb/^{204}Pb$ 15·49–15·63; $^{208}Pb/^{204}Pb$ 38·31–38·74) are, however, similar to those of marine sediments (Fig. 11c and d; Table 11).

In situ zircon Hf isotope data for the BM rhyolites are provided in Table 12, and shown in plots of εHf(t) values vs U–Pb age (Fig. 12a). The ~9·0 Ma zircons from the Southern Malanshan rhyolite sample (2303) have $\varepsilon_{Hf}(t)$ values ranging from –3·4 to –0·7 (weighted average –2·2 ± 0·3) and crustal model ages (T_{DM2}) ranging from 1·14 to 1·31 Ga (average 1·23 Ga) (Table 12; Fig. 12a).

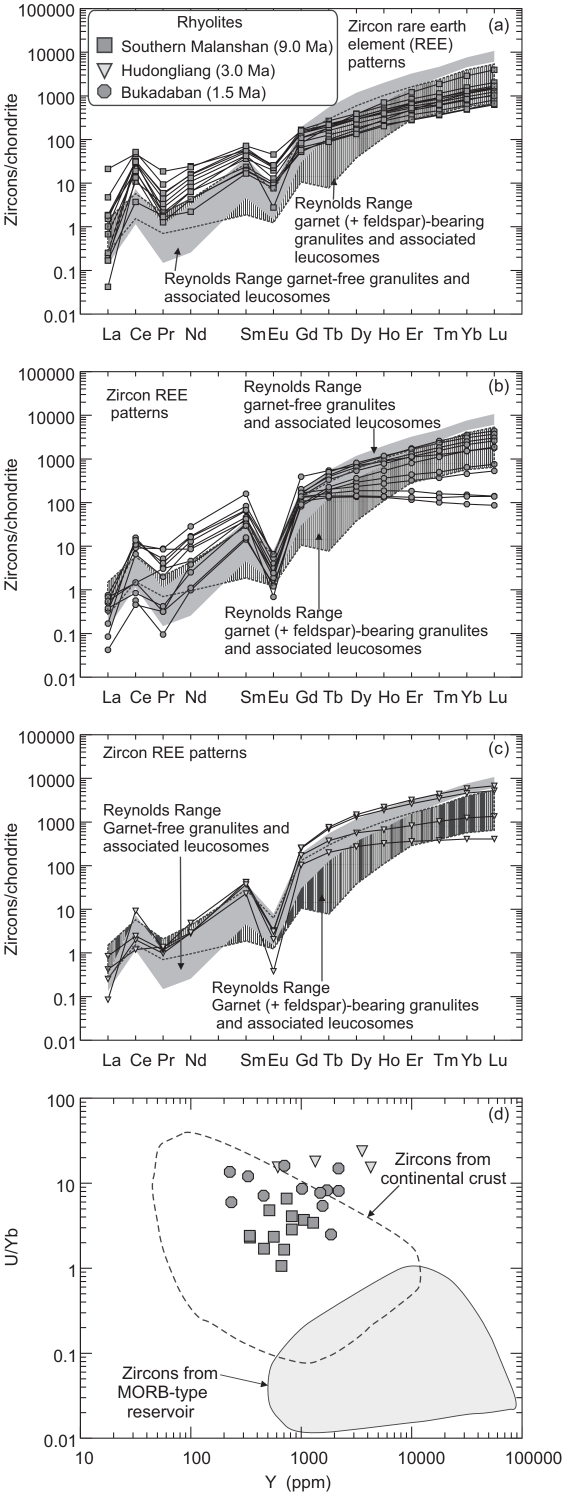

Fig. 4. (a–c) Chondrite-normalized rare earth element patterns for zircons from the BM rhyolites. Chondrite normalization values are from Sun & McDonough (1989). Zircon data for garnet-bearing and garnet-free granulites and associated leucosomes in the Reynolds Range (Australia) are from Rubatto (2002). (d) Variation of U/Yb vs Y for zircons. Fields for zircons from mid-ocean ridge basalt (MORB)-type reservoirs and continental crust are from Grimes *et al.* (2007).

The ~1·5 Ma zircons from the Bukadaban rhyolite sample (2509) have $\varepsilon_{Hf}(t)$ values ranging from −4·7 to −0·8 (weighted average −3·2 ± 0·9) and T_{DM2} values ranging from 1·11 to 1·39 Ga (average 1·28 Ga) (Table 12; Fig. 12a). Most zircon grains in the Hudongliang rhyolite sample ($1P_2JD7$-1), however, are generally too small to permit analysis. The one analysis for an ~3·0 Ma zircon grain from this sample gave a slightly lower $\varepsilon_{Hf}(t)$ (−5·0) and an older T_{DM2} (1·41 Ga) than found in other samples (Table 12; Fig. 12a). Thus, all magmatic zircons from the BM rhyolites exhibit broadly similar $\varepsilon_{Hf}(t)$ and T_{DM2} values (Table 12; Fig. 12a). Moreover, on a magmatic zircon $\varepsilon_{Hf}(t)$ vs whole-rock $\varepsilon_{Nd}(t)$ diagram (Fig. 12b), the BM rhyolites plot in the field of oceanic sediments (Chauvel *et al.*, 2008). Inherited or xenocrystic zircons generally have T_{DM2} values (1·10–1·63 Ga) that are similar to those of cognate magmatic zircons, although several grains returned older (2·02–3·09 Ga) or younger (0·78–1·0 Ga) model ages (Table 12; Fig. 12a).

PETROGENESIS

Crustal melts and source rocks

The BM and Ulugh Muztagh/Weixueshan rocks have the highest SiO_2 contents and $^{87}Sr/^{86}Sr$ values among all reported Cenozoic magmatic rocks in the Songpan–Ganzi Block (Figs 8a, c and 10c, d), indicating that they are unlikely to be derived by mixing between mantle-derived mafic and crust-derived felsic magmas. Moreover, a non-continuous trend in Nd–Sr isotope compositions from Cenozoic mafic to rhyolitic rocks in the Songpan–Ganzi Block (Fig. 10c and d) suggests that they could not be generated by combined crustal assimilation and fractional crystallization involving mantle-derived mafic magmas. We therefore interpret the BM and Ulugh Muztagh/Weixueshan rocks to consist essentially of crustally derived magmas based on the following observations.

First, they are highly silicic and strongly peraluminous (Fig. 8), comparable with the Himalayan leucogranites that have been interpreted to represent crustal melts (Le Fort *et al.*, 1987; Inger & Harris, 1993; Searle *et al.*, 1997, 2007, 2009; Patiño Douce & Harris, 1998; Patiño Douce & McCarthy, 1998; Sylvester, 1998; Barbarin, 1999; Knesel & Davidson, 2002; Guo & Wilson, 2012). Except for the slightly higher LREE contents of the southern Malanshan and Bukadaban biotite rhyolites, their trace element characteristics, including Nb/Ta and Th/La ratios, are also comparable with those of the Himalayan leucogranites (Figs 9 and 10a, b).

Second, they appear to be generated by partial melting of sedimentary rocks. They are similar to metasedimentary or sedimentary rock-derived experimental melts generated under dehydration melting conditions in having strongly peraluminous compositions (ACNK > 1·10) and low Mg# (<47) (e.g. Patiño Douce & Harris, 1998;

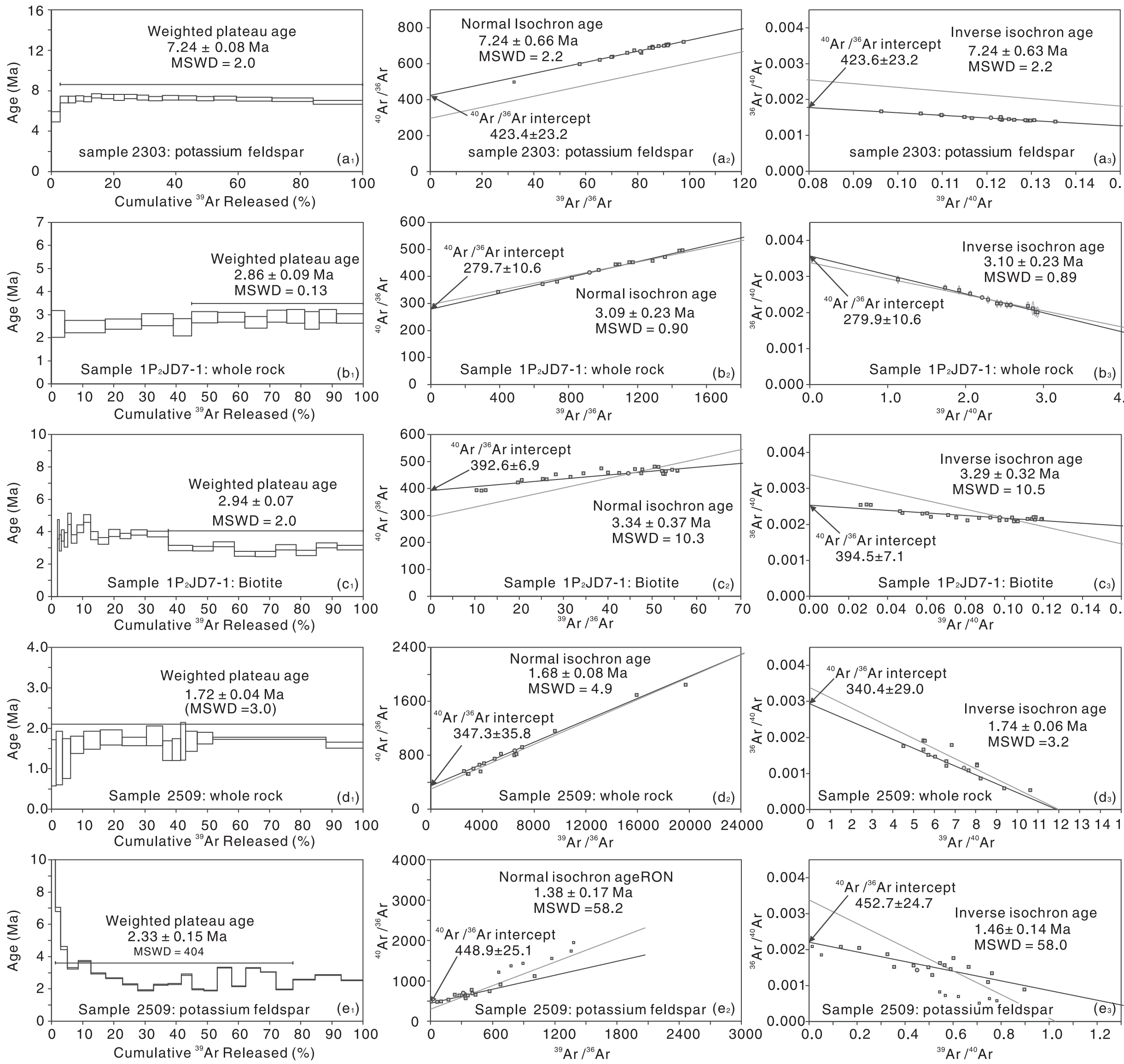

Fig. 5. $^{40}Ar/^{39}Ar$ age spectra diagrams for the Bukadaban–Malanshan rhyolitic rocks. (a_1, b_1, c_1, d_1 and e_1) $^{40}Ar/^{39}Ar$ plateau ages; (a_2, b_2, c_2, d_2 and e_2) $^{40}Ar/^{39}Ar$ isochron ages; (a_3, b_3, c_3, d_3 and e_3) $^{40}Ar/^{39}Ar$ inverse isochron ages.

Patiño Douce & McCarthy, 1998; Castro *et al.*, 2000; Schmidt *et al.*, 2004). They also have Na/Ta and Th/La ratios and Nd–Sr isotopic compositions that are distinct from either Miocene mantle-derived mafic rocks (Turner *et al.*, 1993; Guo *et al.*, 2006) or eclogitic lower crust-derived adakitic rocks (Wang *et al.*, 2005) in the Songpan–Gangzi Block (Fig. 10a and b). Their distinct Nd–Sr isotope compositions, noted above, indicate different crustal source rocks from those of the peraluminous rhyolites in northern Tibet or the Himalayan leucogranites. However, the former have Nb/Ta and Th/La ratios, Th contents and Nd–Sr–Pb–Hf isotopic compositions that are similar to those of marine sediments and Proterozoic–Triassic sedimentary rocks in the Songpang–Ganzi Block (Figs 10–12). Their cognate zircons are continental crust-type (Fig. 4b) and their inherited or captured zircons exhibit an age spectrum similar to those of detrital zircons from the Triassic Songpan–Ganzi sedimentary complex (Fig. 7), which formed in a remnant oceanic basin (e.g. Yin & Harrison, 2000; Wang *et al.*, 2011). Moreover, most inherited or captured zircons have crustal model ages (T_{DM2}) that are similar to those of their magmatic zircons (Table 12; Fig. 12a). It is hence argued that Triassic sedimentary rocks of the Songpan–Ganzi complex may have been accreted to the mid- to lower crust beneath central–northern Tibet as a consequence of southward subduction of the Asian continent during the Cenozoic India–Eurasia convergence or Pre-Cenozoic subduction (Meyer *et al.*, 1998;

Table 7: Summary of argon isotopic data and ages for the Bukadaban-Malanshan rhyolites

Incremental heating		^{36}Ar(a)	^{37}Ar(ca)	^{38}Ar(cl)	^{39}Ar(k)	^{40}Ar(r)	^{40}Ar(r) (%)	^{39}Ar(k) (%)	Age ± 2σ (Ma)
2303 (Kf)									
08G2111B	3·80 W	0·000380	0·000773	0·000000	0·012311	0·028340	14·95	2·81	5·41 ± 0·51
08G2111C	4·20 W	0·000196	0·000584	0·000000	0·011278	0·034207	29·17	2·57	7·12 ± 0·34
08G2111D	4·60 W	0·000166	0·000476	0·000000	0·010885	0·033051	31·90	2·48	7·13 ± 0·34
08G2111E	5·00 W	0·000162	0·000476	0·000000	0·011385	0·035034	33·77	2·60	7·23 ± 0·27
08G2111F	5·40 W	0·000156	0·000430	0·000000	0·010877	0·033169	33·46	2·48	7·16 ± 0·26
08G2111H	6·00 W	0·000177	0·000349	0·000000	0·013959	0·044517	37·17	3·19	7·49 ± 0·22
08G2111I	6·50 W	0·000200	0·000458	0·000000	0·017161	0·054291	39·00	3·92	7·43 ± 0·21
08G2111J	7·00 W	0·000198	0·000353	0·000000	0·015045	0·047017	35·91	3·43	7·34 ± 0·30
08G2111K	7·50 W	0·000208	0·000473	0·000000	0·017791	0·056261	38·95	4·06	7·43 ± 0·21
08G2111L	8·00 W	0·000192	0·000403	0·000000	0·016251	0·050697	38·35	3·71	7·33 ± 0·24
08G2111N	8·80 W	0·000226	0·000558	0·000000	0·019402	0·059638	38·37	4·43	7·22 ± 0·21
08G2111O	9·60 W	0·000260	0·000690	0·000000	0·022890	0·071324	39·28	5·22	7·32 ± 0·23
08G2111P	10·40 W	0·000278	0·000744	0·000000	0·025304	0·078481	39·97	5·77	7·28 ± 0·20
08G2111Q	11·20 W	0·000268	0·000700	0·000000	0·024122	0·074162	39·52	5·50	7·22 ± 0·20
08G2111R	12·50 W	0·000349	0·000930	0·000000	0·032053	0·099172	40·13	7·31	7·27 ± 0·19
08G2111T	15·00 W	0·000509	0·001198	0·000000	0·049746	0·151838	41·29	11·35	7·17 ± 0·20
08G2111U	18·00 W	0·000637	0·001613	0·000000	0·058390	0·177060	39·59	13·32	7·12 ± 0·18
08G2111V	25·00 W	0·000852	0·001815	0·000000	0·069375	0·202260	35·87	15·83	6·85 ± 0·20
$J = 0·0013046 \pm 0·0000020$, $T_{p(plateau\ age)} = 7·24 \pm 0·08$ Ma, $T_{n(normal\ isochron\ age)} = 7·24 \pm 0·66$ Ma, $T_{i(inverse\ isochron\ age)} = 7·24 \pm 0·63$ Ma									
2303 (WR)									
07M2078B	2·00 W	0·000028	0·000250	0·000003	0·010720	0·001325	13·90	4·26	2·60 ± 0·58
07M2078C	3·00 W	0·000051	0·000711	0·000017	0·032778	0·003863	20·27	13·03	2·48 ± 0·26
07M2078D	3·50 W	0·000036	0·000652	0·000006	0·029287	0·003603	25·04	11·65	2·59 ± 0·23
07M2078E	4·00 W	0·000026	0·000652	0·000007	0·025489	0·003371	29·85	10·14	2·78 ± 0·26
07M2078F	4·50 W	0·000020	0·000353	0·000003	0·014807	0·001730	22·14	5·89	2·46 ± 0·37
07M2078H	5·50 W	0·000019	0·000442	0·000005	0·021028	0·002882	33·13	8·36	2·89 ± 0·24
07M2078I	6·50 W	0·000019	0·000428	0·000006	0·021868	0·003005	34·27	8·70	2·89 ± 0·22
07M2078J	7·50 W	0·000014	0·000346	0·000003	0·018051	0·002285	34·87	7·18	2·67 ± 0·25
07M2078K	9·00 W	0·000011	0·000292	0·000003	0·015748	0·002194	39·70	6·26	2·93 ± 0·26
07M2078L	11·00 W	0·000010	0·000264	0·000003	0·014414	0·002001	39·91	5·73	2·92 ± 0·30
07M2078N	13·00 W	0·000009	0·000213	0·000003	0·011657	0·001522	36·79	4·64	2·75 ± 0·39
07M2078O	18·00 W	0·000013	0·000290	0·000003	0·014048	0·001958	33·04	5·59	2·93 ± 0·28
07M2078P	25·00 W	0·000018	0·000471	0·000006	0·021575	0·002903	34·19	8·58	2·83 ± 0·20
$J = 0·0116770 \pm 0·0000175$, $T_{p(plateau\ age)} = 2·86 \pm 0·09$ Ma, $T_{n(normal\ isochron\ age)} = 3·09 \pm 0·23$ Ma, $T_{i(inverse\ isochron\ age)} = 3·10 \pm 0·23$ Ma									
IP2JD7-1(Bi)									
08G2110B	3·80 W	0·000197	0·000074	0·000000	0·002036	0·000000	0·00	0·76	0·00 ± 0·00
08G2110D	4·20 W	0·000101	0·000022	0·000002	0·001247	0·000000	0·00	0·47	0·00 ± 0·00
08G2110E	4·60 W	0·000153	0·000000	0·000001	0·001755	0·000000	0·00	0·66	0·00 ± 0·00
08G2110F	5·00 W	0·000072	0·000000	0·000001	0·001481	0·002638	8·50	0·56	4·15 ± 1·18
08G2110G	5·40 W	0·000098	0·000005	0·000001	0·001930	0·002745	6·62	0·72	3·31 ± 1·00
08G2110J	5·80 W	0·000094	0·000003	0·000001	0·002393	0·003877	9·42	0·90	3·77 ± 0·68
08G2110K	6·30 W	0·000120	0·000058	0·000001	0·003138	0·004718	9·08	1·18	3·50 ± 0·90
08G2110L	6·80 W	0·000108	0·000000	0·000003	0·003053	0·006287	12·84	1·15	4·79 ± 0·70
08G2110O	7·30 W	0·000145	0·000033	0·000003	0·004591	0·007009	10·89	1·72	3·55 ± 0·52
08G2110P	7·90 W	0·000170	0·000087	0·000001	0·005872	0·010560	13·57	2·20	4·18 ± 0·50
08G2110Q	8·50 W	0·000153	0·000059	0·000002	0·005892	0·012210	16·82	2·21	4·82 ± 0·48

(continued)

Table 7: Continued

Incremental heating		^{36}Ar(a)	^{37}Ar(ca)	^{38}Ar(cl)	^{39}Ar(k)	^{40}Ar(r)	^{40}Ar(r) (%)	^{39}Ar(k) (%)	Age ± 2σ (Ma)
08G2110R	9·10 W	0·000159	0·000090	0·000001	0·006343	0·010224	14·04	2·38	3·75 ± 0·50
08G2110T	10·00 W	0·000213	0·000076	0·000004	0·009059	0·013348	13·70	3·40	3·43 ± 0·40
08G2110U	11·00 W	0·000210	0·000084	0·000005	0·009671	0·016303	16·46	3·63	3·92 ± 0·42
08G2110V	12·00 W	0·000199	0·000095	0·000005	0·009519	0·015283	16·27	3·57	3·74 ± 0·34
08G2110W	13·00 W	0·000273	0·000148	0·000005	0·013811	0·023495	17·88	5·18	3·96 ± 0·32
08G2110X	15·00 W	0·000351	0·000177	0·000010	0·018026	0·029887	17·76	6·77	3·86 ± 0·34
08G2110Y	16·50 W	0·000437	0·000272	0·000008	0·020771	0·026735	13·42	7·80	3·00 ± 0·32
08G3110A	18·00 W	0·000318	0·000111	0·000006	0·017702	0·022425	15·15	6·64	2·95 ± 0·28
08G3110B	19·50 W	0·000331	0·000082	0·000007	0·018020	0·024926	16·04	6·76	3·22 ± 0·32
08G3110C	21·00 W	0·000336	0·000083	0·000006	0·017676	0·020042	13·14	6·63	2·64 ± 0·32
08G3110D	22·50 W	0·000337	0·000103	0·000005	0·017782	0·020045	13·11	6·67	2·62 ± 0·32
08G3110E	24·00 W	0·000328	0·000109	0·000004	0·017421	0·022781	14·96	6·54	3·04 ± 0·32
08G3110G	25·50 W	0·000324	0·000069	0·000005	0·017020	0·019715	13·34	6·39	2·70 ± 0·32
08G3110H	27·00 W	0·000342	0·000106	0·000006	0·017838	0·024227	15·23	6·69	3·16 ± 0·30
08G3110I	30·00 W	0·000402	0·000161	0·000005	0·022406	0·029106	15·49	8·41	3·02 ± 0·28
$J = 0{\cdot}0012912 \pm 0{\cdot}0000019$, $T_{p(plateau\ age)} = 2{\cdot}94 \pm 0{\cdot}07$ Ma, $T_{n(normal\ isochron\ age)} = 3{\cdot}34 \pm 0{\cdot}37$ Ma, $T_{i(inverse\ isochron\ age)} = 3{\cdot}29 \pm 0{\cdot}32$ Ma									
2509 (WR)									
07M2079B	2·00 W	0·000002	0·000268	0·000005	0·006650	0·000368	36·39	1·47	1·14 ± 0·57
07M2079C	2·50 W	0·000003	0·000375	0·000002	0·009014	0·000552	32·43	1·99	1·26 ± 0·66
07M2079D	3·00 W	0·000004	0·000479	0·000002	0·012130	0·000734	32·51	2·68	1·25 ± 0·49
07M2079E	3·50 W	0·000006	0·000753	0·000002	0·019088	0·001471	40·89	4·22	1·59 ± 0·22
07M2079F	4·00 W	0·000006	0·000994	0·000007	0·023821	0·001965	45·61	5·26	1·70 ± 0·22
07M2079H	5·00 W	0·000012	0·001324	0·000004	0·031746	0·002729	37·73	7·01	1·78 ± 0·19
07M2079I	6·00 W	0·000009	0·001457	0·000006	0·035376	0·002863	47·23	7·81	1·67 ± 0·10
07M2079J	7·00 W	0·000004	0·000964	0·000001	0·023778	0·002084	55·55	5·25	1·81 ± 0·24
07M2079K	8·50 W	0·000002	0·000502	0·000003	0·013754	0·000965	53·96	3·04	1·45 ± 0·24
07M2079L	10·00 W	0·000002	0·000449	0·000002	0·012244	0·000873	54·85	2·70	1·47 ± 0·27
07M2079N	12·00 W	0·000001	0·000289	0·000000	0·007297	0·000592	51·46	1·61	1·68 ± 0·46
07M2079O	15·00 W	0·000002	0·000693	0·000001	0·016875	0·001374	59·52	3·73	1·68 ± 0·25
07M2079P	18·00 W	0·000002	0·000936	0·000000	0·022274	0·001895	66·76	4·92	1·76 ± 0·14
07M2079Q	30·00 W	0·000010	0·006259	0·000000	0·165046	0·014001	75·26	36·46	1·75 ± 0·03
07M2079R	40·00 W	0·000003	0·003156	0·000030	0·053615	0·004100	76·36	11·84	1·58 ± 0·07
$J = 0{\cdot}0114523 \pm 0{\cdot}0000172$, $T_{p(plateau\ age)} = 1{\cdot}72 \pm 0{\cdot}04$ Ma, $T_{n(normal\ isochron\ age)} = 1{\cdot}68 \pm 0{\cdot}08$ Ma, $T_{i(inverse\ isochron\ age)} = 1{\cdot}74 \pm 0{\cdot}06$ Ma									
2509 (Kf)									
08G2112B	3·8 %	0·000153	0·000191	0·000002	0·001011	0·027968	38·29	0·24	64·94 ± 2·42
08G2112C	4·2%	0·000147	0·000381	0·000000	0·004077	0·035842	45·11	0·98	20·90 ± 0·48
08G2112D	4·6%	0·000110	0·000467	0·000000	0·007027	0·020377	38·50	1·69	6·92 ± 0·28
08G2112E	4·9%	0·000088	0·000470	0·000000	0·009024	0·017090	39·47	2·17	4·52 ± 0·20
08G2112G	5·5%	0·000082	0·000755	0·000000	0·014341	0·019681	44·71	3·45	3·28 ± 0·10
08G2112H	6·0%	0·000073	0·000735	0·000000	0·016960	0·026368	54·99	4·08	3·71 ± 0·06
08G2112I	6·5%	0·000071	0·000640	0·000000	0·019858	0·024569	53·65	4·78	2·96 ± 0·06
08G2112J	7·0%	0·000069	0·000776	0·000000	0·022542	0·025121	55·17	5·43	2·66 ± 0·06
08G2112L	7·5%	0·000061	0·000607	0·000000	0·020373	0·019411	51·79	4·90	2·28 ± 0·06
08G2112M	7·9%	0·000061	0·000880	0·000000	0·020880	0·016615	47·65	5·03	1·90 ± 0·06
08G2112N	8·3%	0·000053	0·000697	0·000000	0·019113	0·018154	53·44	4·60	2·27 ± 0·06
08G2112O	8·7%	0·000045	0·000678	0·000000	0·018103	0·017508	56·77	4·36	2·31 ± 0·06
08G2112Q	9·1%	0·000035	0·000898	0·000000	0·014011	0·016884	61·67	3·37	2·88 ± 0·08

(continued)

Table 7: Continued

Incremental heating		$^{36}Ar(a)$	$^{37}Ar(ca)$	$^{38}Ar(cl)$	$^{39}Ar(k)$	$^{40}Ar(r)$	$^{40}Ar(r)$ (%)	$^{39}Ar(k)$ (%)	Age ± 2σ (Ma)
08G2112R	9·6%	0·000037	0·000662	0·000000	0·015963	0·013216	54·76	3·84	1·98 ± 0·06
08G2112S	10·1%	0·000031	0·000647	0·000000	0·017734	0·014052	60·14	4·27	1·89 ± 0·06
08G2112T	10·6%	0·000029	0·001647	0·000001	0·019118	0·026584	75·33	4·60	3·32 ± 0·04
08G2112V	11·1%	0·000028	0·001053	0·000000	0·019044	0·017234	67·16	4·58	2·16 ± 0·04
08G2112W	11·6%	0·000025	0·000824	0·000000	0·019517	0·026952	78·16	4·70	3·30 ± 0·04
08G2112X	12·3%	0·000024	0·000895	0·000000	0·021013	0·026782	79·06	5·06	3·04 ± 0·04
08G2112Y	13·1%	0·000022	0·000923	0·000000	0·022468	0·018441	73·23	5·41	1·96 ± 0·04
08G3112B	16·6%	0·000025	0·002430	0·000002	0·029527	0·031845	80·67	7·11	2·58 ± 0·02
08G3112C	19·6%	0·000025	0·002370	0·000000	0·034687	0·041538	84·49	8·35	2·86 ± 0·02
08G3112D	25·0%	0·000021	0·001418	0·000000	0·029057	0·030800	82·59	6·99	2·53 ± 0·02

J = 0·0013252 ± 0·0000020, $T_{p(plateau\ age)}$ = 2·33 ± 0·15 Ma, $T_{n(normal\ isochron\ age)}$ = 1·38 ± 0·17 Ma, $T_{i(inverse\ isochron\ age)}$ = 1·46 ± 0·14 Ma

^{40}Ar–^{39}Ar age analyses were conducted on a GV-5400 mass spectrometer, State Key Laboratory of Isotope Geochemistry, Guangzhou Institute of Geochemistry, Chinese Academy of Sciences. WR, whole-rock.

Table 8: SIMS zircon U–Pb data and ages

Sample spot	U (ppm)	Th (ppm)	Th/U	f_{206}%*	$^{238}U/^{206}Pb$	±σ (%)	$^{207}Pb/^{206}Pb$	±σ (%)	$^{206}Pb/^{238}U$ age (Ma)	±σ
2509@9	6261	275	0·044	7·71	4171·285	1·79	0·05726	4·06	1·52	0·03
2509@10	6141	158	0·026	851·56	2867·010	1·51	0·08915	2·95	2·12	0·0
2509@11	7754	276	0·036	8·41	3982·681	1·99	0·05519	3·88	1·60	0·03
2509@12	8358	585	0·070	4·10	4080·310	1·62	0·06003	3·76	1·55	0·03
2509@14	6637	234	0·035	4·03	4007·883	1·72	0·05914	3·79	1·58	0·03
2509@15	10121	481	0·048	1·26	4132·878	1·71	0·05122	3·46	1·55	0·03
2509@16	6546	249	0·038	7·58	3991·399	1·84	0·06234	3·80	1·58	0·03
2509@17	6057	247	0·041	3·64	4215·441	1·92	0·06460	4·10	1·49	0·03
2509@18	6027	218	0·036	3·32	4115·874	1·90	0·04905	4·63	1·56	0·03
2509@19	4869	338	0·070	4·35	4056·294	1·92	0·07221	4·47	1·54	0·03
2509@20	5604	221	0·039	96·82	3786·974	1·84	0·09436	5·94	1·60	0·03
2509@21	8140	450	0·055	10·00	3936·133	1·75	0·08649	3·02	1·55	0·03
2509@22	6708	243	0·036	2·92	4249·485	1·86	0·06598	3·87	1·48	0·03
2509@23	7499	1308	0·174	9·49	3420·764	1·69	0·06234	3·46	1·85	0·03
2509@24	6005	218	0·036	5·75	4096·243	2·36	0·06940	4·23	1·53	0·04
2509@25	6379	264	0·041	19·17	3918·083	1·85	0·06660	4·58	1·60	0·03
2509@26	9770	837	0·086	2·30	4009·830	1·70	0·05319	3·47	1·59	0·03
2509@27	9679	299	0·031	2·57	3540·277	1·71	0·06469	3·46	1·78	0·03
2509@28	5164	207	0·040	10·72	4266·332	1·95	0·07259	4·30	1·46	0·03
2509@29	4384	199	0·045	2·31	4062·872	1·86	0·05549	5·16	1·57	0·03
2509@30	6343	195	0·031	3·64	3573·614	1·80	0·07662	3·54	1·73	0·03
2509@31	5144	341	0·066	49·51	3867·987	1·90	0·05682	4·73	1·64	0·03
2509@32	5681	212	0·037	7·09	4080·388	2·11	0·07492	4·30	1·52	0·03
2509@33	6725	277	0·041	4·65	4228·760	1·88	0·05627	4·28	1·50	0·03
2509@34	14228	346	0·024	14·48	3353·591	1·63	0·15050	2·22	1·67	0·04
2509@35	6099	236	0·039	44·13	4122·779	1·85	0·06728	4·04	1·52	0·03
2509@36	4307	158	0·037	2·07	4193·618	2·01	0·06092	5·11	1·51	0·03
2509@37	5227	219	0·042	4·50	4126·018	1·91	0·06003	5·17	1·53	0·03
2509@38	7491	322	0·043	3·28	4034·918	1·91	0·06016	3·89	1·57	0·03

(continued)

Table 8: Continued

Sample spot	U (ppm)	Th (ppm)	Th/U	f_{206}%*	^{238}U/^{206}Pb	±σ (%)	^{207}Pb/^{206}Pb	±σ (%)	^{206}Pb/^{238}U age (Ma)	±σ
2509@39	4661	155	0·033	1·39	4241·082	1·91	0·05571	4·93	1·50	0·03
2509@40	4436	147	0·033	2·09	4383·142	1·99	0·05383	5·07	1·46	0·03
2509@41	4438	965	0·217	2·72	4134·029	1·96	0·05120	5·83	1·55	0·03
2509@42	4696	340	0·072	21·77	3457·770	2·07	0·20256	5·86	1·49	0·06
2509@43	15542	1839	0·118	0·34	3974·722	1·50	0·05012	2·76	1·61	0·02
2509@44	6135	1557	0·254	22·51	3768·685	1·65	0·07924	3·56	1·64	0·03
2509@45	6406	364	0·057	3·91	4166·122	1·65	0·07825	5·47	1·48	0·03
2509@46	5511	236	0·043	6·43	3953·580	1·86	0·09209	5·85	1·53	0·03
2509@47	6201	539	0·087	13·45	3739·027	1·68	0·13831	3·50	1·52	0·04
2509@48	7995	2881	0·360	9·83	3685·281	1·72	0·06898	3·92	1·70	0·03
1P2JD7-1@1	3116	100	0·032	0·81	2338·1	1·78	0·05581	7·90	2·7	0·1
1P2JD7-1@2	4282	306	0·071	5·05	1982·2	1·91	0·05320	4·02	3·2	0·1
1P2JD7-1@3	57449	1217	0·021	0·07	2018·4	1·65	0·04810	2·41	3·2	0·1
1P2JD7-1@4	59311	1304	0·02	2·43	1927·6	1·57	0·065171	4·18	3·3	0·1
1P2JD7-1@5	1894	1516	0·80	11·60	535·2	2·71	0·109531	6·95	11·1	0·3
1P2JD7-1@6	34919	1739	0·05	2·49	1985·5	2·21	0·066072	5·84	3·2	0·1
1P2JD7-1@7	33416	739	0·02	5·53	1962·1	1·57	0·090693	6·20	3·1	0·1
1P2JD7-1@8	31107	721	0·02	10·03	1862·8	2·18	0·108575	8·03	3·2	0·1
1P2JD7-1@9	28956	660	0·02	5·19	1948·2	1·78	0·095923	7·40	3·1	0·1
1P2JD7-1@10	4929	763	0·15	14·85	1119·6	2·20	0·169319	5·95	4·9	0·2
1P2JD7-1@11	58556	1137	0·019	0·29	2005·7	1·62	0·05045	2·65	3·2	0·1
1P2JD7-1@12	35895	782	0·022	1·40	1781·9	1·65	0·05710	3·10	3·6	0·1
1P2JD7-1@13	45293	1018	0·022	1·69	2079·3	1·61	0·05238	1·87	3·1	0·0
1P2JD7-1@14	60684	1140	0·019	1·01	2066·8	1·63	0·05400	1·87	3·1	0·1
1P2JD7-1@15	47620	891	0·019	0·77	2126·5	1·66	0·04992	2·06	3·0	0·1
1P2JD7-1@16	2289	3194	1·395	70·96	226·1	3·50	0·58037	1·86	9·1	2·5
1P2JD7-1@17	73330	2713	0·037	0·80	1959·7	1·60	0·05157	1·57	3·3	0·1
1P2JD7-1@18	6575	444	0·067	78·78	2027·2	2·21	0·11872	8·70	2·9	0·1
2303@1	469	626	1·335	0·03	719·561	2·21	0·05586	6·42	8·8	0·2
2303@2	181	305	1·689	0·30	733·403	3·58	0·06013	12·21	8·6	0·3
2303@3	625	439	0·703	0·18	14·712	1·64	0·05534	1·07	423·9	6·8
2303@4	137	190	1·389	0·10	725·093	3·97	0·07414	10·63	8·6	0·4
2303@5	305	248	0·814	0·05	725·258	3·27	0·05867	9·15	8·7	0·3
2303@6	1652	2965	1·795	5·51	20·437	2·18	0·05507	0·95	307·0	6·6
2303@7	192	277	1·441	0·11	10·855	1·50	0·05877	1·28	568·3	8·3
2303@8	185	291	1·570	0·04	676·591	3·11	0·07432	15·90	9·2	0·3
2303@9	681	438	0·643	0·05	9·329	10·68	0·10095	7·46	623·6	65·3
2303@10	1127	526	0·467	4·14	15·550	1·54	0·05644	0·77	400·9	6·1
2303@11	54	47	0·866	0·21	8·491	2·32	0·06916	2·88	712·4	16·2
2303@12	298	362	1·214	0·33	657·646	2·62	0·10597	7·66	9·0	0·3
2303@13	457	248	0·543	30·39	656·662	2·60	0·07424	7·89	9·5	0·3
2303@14	208	352	1·692	21·18	601·031	3·61	0·20057	10·21	8·6	0·5
2303@15	546	1162	2·128	37·55	665·698	2·63	0·10850	6·93	8·9	0·3
2303@16	223	477	2·142	0·36	460·275	4·72	0·25635	10·07	10·2	0·8
2303@17	393	420	1·067	13·87	667·038	3·16	0·12220	8·82	8·7	0·3
2303@18	254	273	1·074	25·71	462·651	2·91	0·26749	6·51	10·0	0·7
2303@19	7382	273	0·037	5·19	625·258	1·50	0·04871	2·31	10·3	0·2
2303@20	527	689	1·307	6·75	688·107	2·28	0·08063	5·57	9·0	0·2

SIMS zircon U–Pb analyses were conducted on the Cameca IMS-1280 SIMS at the Institute of Geology and Geophysics, Chinese Academy of Sciences.
*f_{206} is the proportion of common ^{206}Pb in total measured ^{206}Pb.

Table 9: LA-ICP-MS U–Pb isotopic data and ages for zircons from the Bukadaban–Malanshan rhyolites (Wuhan)

Sample spot	Pb (ppm)	Th (ppm)	U (ppm)	Th/U	$^{207}Pb/^{206}Pb$		$^{207}Pb/^{235}U$		$^{206}Pb/^{238}U$		$^{207}Pb/^{206}Pb$ (Ma)		$^{207}Pb/^{235}U$ (Ma)		$^{206}Pb/^{238}U$ (Ma)	
					Ratio	1σ	Ratio	1σ	Ratio	1σ	Age	1σ	Age	1σ	Age	1σ
2303																
1	1·9	151	173	0·87	0·40557	0·04868	0·08592	0·00805	0·00202	0·00011	3931	181	83·7	7·5	13·0	0·7
2	38·8	220	280	0·79	0·05411	0·00268	0·31319	0·01504	0·04223	0·00095	376	111	277	12	267	6
3	158	334	420	0·79	0·07141	0·00120	1·25832	0·02354	0·12867	0·00173	969	1	827	11	780	10
4	5·2	938	581	1·62	0·13516	0·01560	0·02308	0·00217	0·00145	0·00006	2166	202	23·2	2·2	9·3	0·4
5	480	342	598	0·57	0·11958	0·00075	5·36767	0·03910	0·32410	0·00161	1950	11	1880	6	1810	8
6	2·7	303	558	0·54	0·12575	0·01504	0·02220	0·00280	0·00135	0·00006	2039	212	22·3	2·8	8·7	0·4
7	35·7	168	319	0·53	0·05617	0·00095	0·48168	0·00801	0·06220	0·00035	457	37	399	5	389	2
8	1·3	140	140	1·00	0·60582	0·08704	0·08912	0·01356	0·00136	0·00010	4522	227	86·7	12·6	8·8	0·6
9	71·7	396	775	0·51	0·05324	0·00070	0·38789	0·00504	0·05266	0·00023	339	30	333	4	331	1
10	2·5	326	469	0·69	0·24677	0·02724	0·04297	0·00432	0·00138	0·00005	3164	176	42·7	4·2	8·9	0·4
11	1·9	255	157	1·62	0·55611	0·13376	0·05672	0·00513	0·00143	0·00010	4397	360	56·0	4·9	9·2	0·6
12	1·7	111	331	0·34	0·33508	0·05312	0·04411	0·00411	0·00134	0·00007	3640	245	43·8	4·0	8·6	0·4
13	5·2	361	2148	0·17	0·07431	0·00659	0·01600	0·00135	0·00160	0·00004	1050	180	16·1	1·4	10·3	0·3
14	13·5	3·4	20·0	0·17	0·16562	0·00517	10·02110	0·30749	0·43934	0·00623	2514	52	2437	28	2348	28
15	1·2	146	161	0·91	0·35909	0·09926	0·07314	0·01393	0·00142	0·00011	3746	434	71·7	13·2	9·1	0·7
16	6·8	142	3671	0·04	0·04624	0·00347	0·01129	0·00082	0·00179	0·00003	9·36	179·6	11·4	0·8	11·5	0·2
17	2·3	334	349	0·96	0·15224	0·01498	0·02715	0·00242	0·00139	0·00005	2372	169	27·2	2·4	8·9	0·3
18	17·2	101	175	0·58	0·05249	0·00190	0·36209	0·01322	0·05009	0·00051	306	83	314	10	315	3
19	2·7	669	502	1·33	0·14680	0·03016	0·02775	0·00513	0·00138	0·00008	2309	360	27·8	5·1	8·9	0·5
20	59·6	483	873	0·55	0·05625	0·00287	0·24855	0·00586	0·03531	0·00081	461	113	225	5	224	5
21	61·7	219	614	0·36	0·05394	0·00061	0·52994	0·00609	0·07108	0·00028	369	26	432	4	443	2
22	2·8	576	653	0·88	0·10284	0·01011	0·01994	0·00153	0·00150	0·00005	1676	182	20·0	1·5	9·7	0·3
23	10·4	9·3	17·0	0·55	0·11225	0·00293	4·92882	0·12313	0·32097	0·00269	1836	48	1807	21	1794	13
24	1·0	103	142	0·73	0·52008	0·06916	0·06993	0·00556	0·00135	0·00008	4299	198	68·6	5·3	8·7	0·5
25	1·7	237	360	0·66	0·20115	0·03688	0·03281	0·00450	0·00142	0·00008	2835	302	32·8	4·4	9·1	0·5
26	42·1	229	502	0·46	0·06616	0·00090	0·41246	0·00537	0·04530	0·00026	813	28	351	4	286	2
27	81·3	432	1009	0·43	0·10947	0·00081	0·82829	0·00646	0·05468	0·00029	1791	14	613	4	343	2
28	2·7	225	204	1·10	0·60451	0·13324	0·07083	0·00914	0·00136	0·00008	4519	365	69·5	8·7	8·7	0·5
29	5·4	282	177	1·59	0·61887	0·04669	0·18730	0·00898	0·00278	0·00009	4553	110	174	8	18	1
30	6·9	39·0	92·0	0·42	0·11252	0·00521	0·32224	0·01447	0·02137	0·00032	1840	84	284	11	136	2
31	1·7	259	719	0·36	0·09537	0·01224	0·01958	0·00264	0·00149	0·00004	1544	244	19·7	2·6	9·6	0·3
32	2·5	304	234	1·30	0·25555	0·02951	0·04344	0·00478	0·00136	0·00006	3219	183	43·2	4·6	8·8	0·4
33	0·9	168	179	0·94	0·31674	0·03771	0·04998	0·00388	0·00137	0·00006	3554	185	49·5	3·7	8·8	0·4
34	57·5	81·0	66·9	1·21	0·11335	0·00171	4·25561	0·06509	0·27182	0·00161	1854	26	1685	13	1550	8
35	1·3	173	197	0·88	0·35427	0·04564	0·05408	0·00396	0·00139	0·00006	3726	197	53·5	3·8	8·9	0·4
36	1·7	295	192	1·54	0·32503	0·05852	0·05244	0·00809	0·00144	0·00009	3594	279	51·9	7·8	9·3	0·6
1P2JD7-1																
1	10·8	219	20645	0·01	0·05529	0·00312	0·00350	0·00020	0·00046	0·00001	433	123	3·55	0·20	2·97	0·07
2	529	770	464	1·66	0·06980	0·00141	1·43564	0·03172	0·14982	0·00251	924	43	904	13	900	14
3	197	207	580	0·36	0·06722	0·00119	1·23688	0·02494	0·13503	0·00216	856	37	817	11	817	12
4	3·7	484	364	1·33	0·15171	0·00911	0·02462	0·00132	0·00138	0·00004	2365	103	24·69	1·31	8·91	0·29
5	10·1	308	19550	0·02	0·05487	0·00156	0·00354	0·00011	0·00048	0·00001	406	68	3·58	0·11	3·12	0·07
6	6·3	715	3628	0·20	0·06269	0·00463	0·00712	0·00056	0·00082	0·00002	698	158	7·20	0·57	5·29	0·12
7	10·0	239	17323	0·01	0·05548	0·00137	0·00358	0·00009	0·00047	0·00001	432	56	3·63	0·09	3·04	0·03

(continued)

Table 9: Continued

Sample spot	Pb (ppm)	Th (ppm)	U (ppm)	Th/U	$^{207}Pb/^{206}Pb$		$^{207}Pb/^{235}U$		$^{206}Pb/^{238}U$		$^{207}Pb/^{206}Pb$ (Ma)		$^{207}Pb/^{235}U$ (Ma)		$^{206}Pb/^{238}U$ (Ma)	
					Ratio	1σ	Ratio	1σ	Ratio	1σ	Age	1σ	Age	1σ	Age	1σ
8	37·7	112	711	0·16	0·05642	0·00237	0·27854	0·01461	0·03575	0·00124	478	94	250	12	226	8
9	12·4	748	23740	0·03	0·05134	0·00151	0·00331	0·00010	0·00047	0·00001	257	69	3·35	0·10	3·04	0·05
10	13·4	399	7736	0·05	0·10204	0·00309	0·00672	0·00021	0·00049	0·00001	1661	56	6·80	0·21	3·16	0·05
11	10·1	43	129	0·33	0·05830	0·00226	0·26853	0·01275	0·03483	0·00091	543	90	242	10	221	6
12	949	494	1214	0·41	0·10770	0·00159	4·56065	0·12444	0·30806	0·00849			1742	23	1731	42
13	20·5	525	29190	0·02	0·06263	0·00145	0·00407	0·00010	0·00048	0·00001	694	44	4·12	0·11	3·10	0·06
14	9·1	332	23450	0·01	0·05994	0·00144	0·00393	0·00010	0·00048	0·00001	611	52	3·98	0·10	3·09	0·04
15	2·3	284	221	1·28	0·28512	0·03540	0·05695	0·00622	0·00161	0·00009	3391	195	56	6	10·3	0·56
16	3·6	0·09	1·36	0·07	1·15485	0·12582	19·63286	1·44452	0·16135	0·01161			3073	71	964	64
17	10·9	362	19508	0·02	0·05145	0·00126	0·00343	0·00010	0·00049	0·00001	261	53	3·48	0·10	3·13	0·05
18	3·1	3·27	18·1	0·18	1·29040	0·10764	3·82117	0·20835	0·03142	0·00187			1597	44	199	12
19	8·8	296	19143	0·02	0·05212	0·00135	0·00344	0·00010	0·00049	0·00001	300	59	3·49	0·10	3·13	0·06
20	5·1	0·09	1·73	0·05	1·39686	0·15478	19·72129	1·66673	0·14864	0·01111			3078	82	893	62
21	20·5	349	23833	0·01	0·07847	0·00261	0·00543	0·00021	0·00050	0·00001	1159	67	5·50	0·21	3·23	0·06
22	6·7	720	13288	0·05	0·05486	0·00247	0·00354	0·00017	0·00048	0·00001	406	102	3·59	0·18	3·07	0·08
23	12·1	372	17723	0·02	0·05936	0·00174	0·00391	0·00013	0·00048	0·00001	589	63	3·96	0·13	3·09	0·04
24	9·3	361	17823	0·02	0·05664	0·00141	0·00365	0·00009	0·00047	0·00000	476	56	3·70	0·09	3·03	0·02
25	48·5	296	361	0·82	0·64710	0·02837	0·44212	0·01771	0·00510	0·00020	4618	63	372	12	32·81	1·30
26	391	319	1700	0·19	0·06708	0·00080	1·27341	0·02230	0·13699	0·00196	840	24	834	10	828	11
2509																
1	1·77	220·9	223	0·99	0·59223	0·07333	0·05068	0·00305	0·00087	0·00004	4500	181	50·2	2·9	5·64	0·24
2	4·41	1192·6	2040	0·58	0·06244	0·00478	0·00741	0·00057	0·00086	0·00002	700	169	7·50	0·58	5·55	0·10
3	5·66	71·5	3455	0·02	0·04940	0·00164	0·01143	0·00038	0·00169	0·00003	169	78	11·54	0·38	10·86	0·20
4	2·51	658	484	1·36	0·14223	0·01508	0·01913	0·00183	0·00095	0·00004	2255	184	19·24	1·82	6·11	0·25
5	2·63	123	7248	0·02	0·10065	0·00904	0·00318	0·00030	0·00023	0·00001	1636	168	3·23	0·31	1·46	0·03
6	10·67	21817	5743	3·80	0·10560	0·01002	0·00352	0·00036	0·00024	0·00001	1725	180	3·57	0·36	1·58	0·06
7	1·50	140	830	0·17	0·09215	0·01217	0·01319	0·00119	0·00119	0·00004	1472	252	13·30	1·20	7·65	0·26
8	1·93	168	5967	0·03	0·08062	0·00786	0·00236	0·00019	0·00023	0·00000	1213	194	2·40	0·19	1·45	0·03
9	0·92	51·1	516	0·10	0·12465	0·01116	0·01526	0·00103	0·00104	0·00004	2024	159	15·38	1·03	6·71	0·24
10	1·24	147	4625	0·03	0·07398	0·00577	0·00229	0·00020	0·00023	0·00001	1043	157	2·33	0·21	1·48	0·04
11	0·98	138	3260	0·04	0·10421	0·00645	0·00305	0·00017	0·00023	0·00001	1702	113	3·09	0·17	1·45	0·04
12	1·16	238	4243	0·06	0·06786	0·00627	0·00198	0·00014	0·00023	0·00001	865	197	2·01	0·14	1·46	0·05
13	0·69	182	151	1·20	0·59977	0·14926	0·04138	0·00316	0·00084	0·00007	4509	422	41·17	3·08	5·41	0·48
14	0·98	189	4071	0·05	0·09183	0·00584	0·00277	0·00016	0·00023	0·00000	1465	121	2·81	0·16	1·46	0·03
15	1·53	130	4119	0·03	0·09206	0·00595	0·00285	0·00017	0·00023	0·00000	1533	123	2·89	0·18	1·48	0·03
16	0·94	132	3731	0·04	0·07245	0·00699	0·00220	0·00022	0·00023	0·00001	998	196	2·23	0·23	1·47	0·04
17	5·97	10446	4270	2·45	0·11826	0·01044	0·00364	0·00028	0·00024	0·00001	1931	159	3·69	0·28	1·55	0·06
18	1·13	136	3876	0·04	0·09201	0·00618	0·00274	0·00016	0·00023	0·00001	1533	95	2·77	0·16	1·47	0·04
19	1·46	818	4107	0·20	0·08676	0·00513	0·00275	0·00016	0·00024	0·00000	1355	114	2·79	0·16	1·56	0·03
20	2·79	141	5140	0·03	0·15387	0·01074	0·00478	0·00034	0·00023	0·00001	2391	119	4·84	0·34	1·51	0·05
21	23·5	33·7	683	0·05	0·05542	0·00150	0·27560	0·00902	0·03603	0·00077	428	59	247	7	228	5
22	1·01	131	3995	0·03	0·09078	0·00731	0·00281	0·00024	0·00023	0·00001	1443	154	2·85	0·24	1·50	0·06
23	2·59	92·0	4305	0·02	0·13196	0·01468	0·00402	0·00039	0·00024	0·00001	2124	195	4·07	0·40	1·53	0·06
24	1·22	98·3	3341	0·03	0·12260	0·01011	0·00360	0·00028	0·00024	0·00001	1994	180	3·65	0·29	1·56	0·08
25	7·95	13307	7164	1·86	0·08740	0·00701	0·00278	0·00018	0·00024	0·00001	1369	155	2·82	0·19	1·57	0·04
26	1·74	397	4875	0·08	0·08332	0·00843	0·00242	0·00025	0·00024	0·00001	1277	199	2·46	0·25	1·54	0·09

(continued)

Table 9: Continued

Sample spot	Pb (ppm)	Th (ppm)	U (ppm)	Th/U	$^{207}Pb/^{206}Pb$		$^{207}Pb/^{235}U$		$^{206}Pb/^{238}U$		$^{207}Pb/^{206}Pb$ (Ma)		$^{207}Pb/^{235}U$ (Ma)		$^{206}Pb/^{238}U$ (Ma)	
					Ratio	1σ	Ratio	1σ	Ratio	1σ	Age	1σ	Age	1σ	Age	1σ
27	1·10	175	5229	0·03	0·07405	0·00910	0·00211	0·00024	0·00023	0·00001	1043	250	2·14	0·24	1·47	0·07
28	1·43	130	4462	0·03	0·08004	0·01169	0·00222	0·00033	0·00023	0·00002	1198	291	2·25	0·33	1·51	0·15
29	2·02	1240	4546	0·27	0·09238	0·00572	0·00295	0·00020	0·00024	0·00001	1476	117	2·99	0·20	1·54	0·06
30	1·24	110	3055	0·04	0·13660	0·00893	0·00431	0·00024	0·00025	0·00001	2184	114	4·36	0·25	1·63	0·04
31	0·92	100	2929	0·03	0·12695	0·01320	0·00348	0·00029	0·00023	0·00001	2057	184	3·53	0·29	1·46	0·05
32	1·90	287	5477	0·05	0·05881	0·00573	0·00253	0·00023	0·00032	0·00001	561	214	2·56	0·23	2·07	0·04
33	1·17	117	3417	0·03	0·09974	0·00664	0·00306	0·00021	0·00023	0·00001	1620	119	3·10	0·22	1·49	0·04
34	2·76	225	6001	0·04	0·12982	0·01582	0·00401	0·00048	0·00023	0·00001	2095	215	4·06	0·49	1·50	0·04
35	0·83	114	2816	0·04	0·11936	0·00658	0·00389	0·00018	0·00026	0·00001	1947		3·95	0·18	1·69	0·04
36	0·70	91·9	2308	0·04	0·11559	0·00649	0·00425	0·00025	0·00028	0·00001	1889		4·30	0·25	1·80	0·06
37	1·01	89·0	2306	0·04	0·21476	0·02452	0·00927	0·00104	0·00032	0·00001	2942		9·37	1·05	2·04	0·08
38	2·25	115	3077	0·04	0·27020	0·02128	0·01786	0·00187	0·00046	0·00001	3307		17·98	1·87	2·96	0·09
39	3·88	206	15402	0·01	0·04897	0·00363	0·00161	0·00011	0·00024	0·00001	146		1·64	0·11	1·56	0·03
40	1·15	130	4236	0·03	0·08013	0·00614	0·00263	0·00019	0·00025	0·00001	1200		2·66	0·20	1·64	0·05
41	0·83	116	2967	0·04	0·10755	0·00695	0·00348	0·00019	0·00026	0·00001	1758		3·53	0·19	1·68	0·04
42	3·13	87·6	8838	0·01	0·05956	0·00249	0·00267	0·00010	0·00033	0·00000	588	91	2·70	0·11	2·13	0·03
43	0·98	155	3393	0·05	0·10348	0·00466	0·00362	0·00016	0·00027	0·00000	1687	83	3·67	0·16	1·73	0·03
44	1·00	154	3643	0·04	0·09217	0·00708	0·00306	0·00023	0·00026	0·00001	1471	146	3·10	0·23	1·68	0·05
45	0·82	109	2813	0·04	0·12383	0·00875	0·00414	0·00029	0·00026	0·00001	2012	126	4·20	0·30	1·68	0·05
46	0·91	141	2941	0·05	0·10706	0·01047	0·00358	0·00037	0·00026	0·00001	1750	180	3·63	0·38	1·66	0·09
47	5·64	35·4	31	1·13	0·06857	0·00251	1·21725	0·04723	0·13256	0·00193	886	75·9	809	22	802	11

LA-ICP-MS zircon U–Pb analyses were conducted on an Agilent 7500 ICP-MS system equipped with a 193 nm laser, at the State Key Laboratory of Geological Processes and Mineral Resources, Faculty of Earth Sciences, China University of Geosciences (Wuhan).

Yin & Harrison, 2000; Tapponnier *et al.*, 2001; Kapp *et al.*, 2003, 2005, 2007; Yin *et al.*, 2008*a*, 2008*b*; Zhao *et al.*, 2010, 2011) and, subsequently, via partial melting, were involved in the generation of the rhyolitic rocks during Miocene–Pleistocene times.

Mineral constituents of the source rocks

Geochemical, petrological and melting experiment studies have been used to demonstrate that the Himalayan leucogranites were derived by melting of metasedimentary rocks, driven by fluid-absent mica (muscovite or biotite) breakdown (e.g. Inger & Harris, 1993; Harris & Massey, 1994; Harris *et al.*, 1995; Patiño Douce & Harris, 1998; Knesel & Davidson, 2002). Geochemical model calculations for the melting of metasedimentary rocks suggest that the Rb–Ba–Sr systematics can be used to trace the fluid-absent reaction involving the dehydration of mica during the formation of the Himalayan leucogranites (e.g. Harris & Inger, 1992; Inger & Harris, 1993; Harris & Massey, 1994; Harris *et al.*, 1995; Zhang *et al.*, 2004). The particular melt reaction involved will leave a distinct Rb, Sr and Ba signature in the melt, given that these elements occur almost entirely in the reactant phases (mica and feldspar) rather than in accessory phases (e.g. Harris & Inger, 1992; Zhang *et al.*, 2004). As Ba and Rb are highly compatible in K-feldspar and mica, respectively, lower-degree partial melting involving mica breakdown can cause Rb/Sr enhancement and Ba depletion in the melt (Harris & Inger, 1992). Experimental data suggest that fluid-absent melting of two-mica pelites during prograde metamorphism is initiated by the breakdown of muscovite and proceeds with progressive breakdown of biotite (Patiño Douce & Harris, 1998; Patiño Douce & McCarthy, 1998; Vielzeuf & Schmidt, 2001). Breakdown of either mica under fluid-absent conditions would cause an increase in Rb/Sr ratios in the melt, concomitant with depletion in Ba if feldspar is retained in the residue (Zhang *et al.*, 2004). Thus, the strong negative correlation between Rb/Sr and Ba for the Himalayan leucogranites (Fig. 13a) is indicative of the presence of residual alkali feldspar during the fluid-absent melting of metasedimentary rocks involving the dehydration breakdown of mica

Table 10: LA-ICP-MS U–Pb isotopic data and ages for zircons from the Bukadaban–Malanshan rhyolites (Guangzhou)

Sample spot	Pb (ppm)	Th (ppm)	U (ppm)	Th/U	^{207}Pb/^{206}Pb		^{207}Pb/^{235}U		^{206}Pb/^{238}U		^{207}Pb/^{206}Pb (Ma)		^{207}Pb/^{235}U (Ma)		^{206}Pb/^{238}U (Ma)	
					Ratio	1σ	Ratio	1σ	Ratio	1σ	Age	1σ	Age	1σ	Age	1σ
2303																
1	1·68	418	975	0·43	0·0697	0·0097	0·0140	0·0025	0·0014	0·0001	920	289	14·2	2·5	9·0	0·6
2	0·38	173	177	0·98	0·1812	0·0410	0·0262	0·0045	0·0014	0·0001	2664	383	26·2	4·5	8·7	0·7
3	1·37	367	549	0·67	0·0890	0·0169	0·0191	0·0042	0·0015	0·0001	1403	371	19·2	4·2	9·4	0·4
4	0·64	170	319	0·53	0·0995	0·0147	0·0178	0·0026	0·0014	0·0001	1617	279	17·9	2·6	8·7	0·6
5	1·52	300	853	0·35	0·1744	0·0488	0·0267	0·0058	0·0014	0·0001	2611	483	26·8	5·7	9·0	0·5
6	2·30	141	189	0·75	0·4368	0·0784	0·3278	0·0904	0·0041	0·0006	4043	271	287·9	69·2	26·2	3·9
7	0·61	308	270	1·14	0·0979	0·0229	0·0202	0·0043	0·0014	0·0001	1585	449	20·3	4·3	9·0	0·7
8	9·22	171	673	0·25	0·6210	0·1462	0·7788	0·3421	0·0061	0·0014	4558	393	584·8	197·7	39·2	9·0
9	1·434	60·4	922	0·07	0·0924	0·0317	0·0151	0·0049	0·0014	0·0001	1476	693	15·3	4·9	8·8	0·9
10	0·69	184	206	0·89	0·2041	0·0456	0·0433	0·0092	0·0018	0·0001	2861	372	43·1	9·0	11·4	0·8
11	2·18	231	1460	0·16	0·0581	0·0093	0·0103	0·0015	0·0014	0·0001	532	325	10·4	1·5	8·8	0·5
12	12·78	107	1677	0·06	0·0462	0·0040	0·0516	0·0113	0·0081	0·0016	9·36	201·8	51·1	11·0	51·9	10·2
13	0·44	249	151	1·66	0·0740	0·0056	0·0148	0·0004	0·0014	0·0002	1043	154	15·0	0·4	9·1	1·1
14	2·68	165	1377	0·12	0·0959	0·0297	0·0195	0·0067	0·0014	0·0001	1546	613	19·6	6·7	9·3	0·3
15	0·95	130	130	1·00	0·5045	0·2230	0·1928	0·1160	0·0024	0·0004	4255	883	179·0	99·1	15·6	2·8
2509																
1	0·14	260	311	0·84	0·5002	0·1260	0·0123	0·0027	0·0002	0·0000	4242	381	12·4	2·7	1·59	0·29
2	0·31	177	214	0·83	0·2441	0·0345	0·0288	0·0050	0·0009	0·0001	3147	227	28·8	4·9	5·87	0·68
3	1·3	701	1394	0·50	0·0556	0·0115	0·0058	0·0010	0·0008	0·0000	435	405	5·83	1·1	5·06	0·28
4	2·3	35	1750	0·02	0·0496	0·0050	0·0082	0·0008	0·0012	0·0000	176	222	8·28	0·8	7·86	0·27
5	2·7	268	9035	0·03	0·1502	0·0212	0·0044	0·0006	0·0002	0·0000	2348	244	4·45	0·6	1·47	0·10
6	0·63	425	555	0·77	0·0556	0·0178	0·0076	0·0025	0·0009	0·0001	435	598	7·66	2·6	5·89	0·54
7	4·9	46210	6112	7·56	0·1244	0·0188	0·0044	0·0008	0·0003	0·0000	2020	304	4·48	0·8	1·63	0·07
8	2·9	1841	898	2·05	0·0519	0·0081	0·0113	0·0018	0·0016	0·0001	283	322	11·4	1·9	10·0	0·44
9	3·0	21667	5043	4·30	0·0890	0·0262	0·0029	0·0008	0·0002	0·0000	1406	591	2·91	0·8	1·45	0·08
10	1·2	157	4232	0·04	0·0458	0·0117	0·0015	0·0004	0·0002	0·0000			1·48	0·4	1·52	0·29
11	1·0	104	3523	0·03	0·0527	0·0135	0·0016	0·0004	0·0002	0·0000	322	491	1·59	0·4	1·58	0·09
12	0·61	62	2222	0·03	0·0927	0·0162	0·0028	0·0005	0·0002	0·0000	1483	337	2·79	0·5	1·46	0·14
13	0·17	168	140	1·21	0·2672	0·0754	0·0220	0·0042	0·0008	0·0001	3290	459	22·1	4·1	5·42	0·54
14	1·3	87	2787	0·03	0·7574	0·3495	0·0115	0·0040	0·0003	0·0000			11·7	4·0	1·64	0·22
15	1·9	10390	4201	2·47	0·1375	0·0733	0·0044	0·0023	0·0002	0·0000	2196	1086	4·44	2·3	1·52	0·29
16	4·0	13860	7322	1·89	0·3068	0·0598	0·0106	0·0025	0·0002	0·0000	3505	306	10·8	2·5	1·56	0·11

LA-ICP-MS zircon U–Pb analyses were conducted on an Agilent 7500 ICP-MS system equipped with a 193 nm laser, the State Key Laboratory of Isotope Geochemistry, Guangzhou Institute of Geochemistry, Chinese Academy of Sciences.

(Inger & Harris, 1993; Zhang *et al.*, 2004). As is the case for the Himalayan leucogranites, the BM rhyolite samples exhibit a strong negative correlation between Rb/Sr and Ba, which is consistent with the trend for the dehydration melting of mica-bearing metasedimentary rocks with alkali feldspar as a residual phase (Fig. 13a). The tourmaline-bearing mica rhyolites in the Hudongliang area exhibit the highest Rb/Sr and lowest Ba values among the BM rhyolites (Fig. 13a), similar to tourmaline-bearing leucogranites that represent primary near-minimum melts from a water-undersaturated source (e.g. Inger & Harris, 1993; Searle *et al.*, 1997; Searle & Godin, 2003). Their mineral constituents, including potassium feldspar, albite, quartz, very minor oligoclase and no calcic plagioclase (Figs 2c, d and 3e), further confirm the above conclusion.

Plagioclase occurs with alkali feldspar as a residual phase during the dehydration melting of mica-bearing

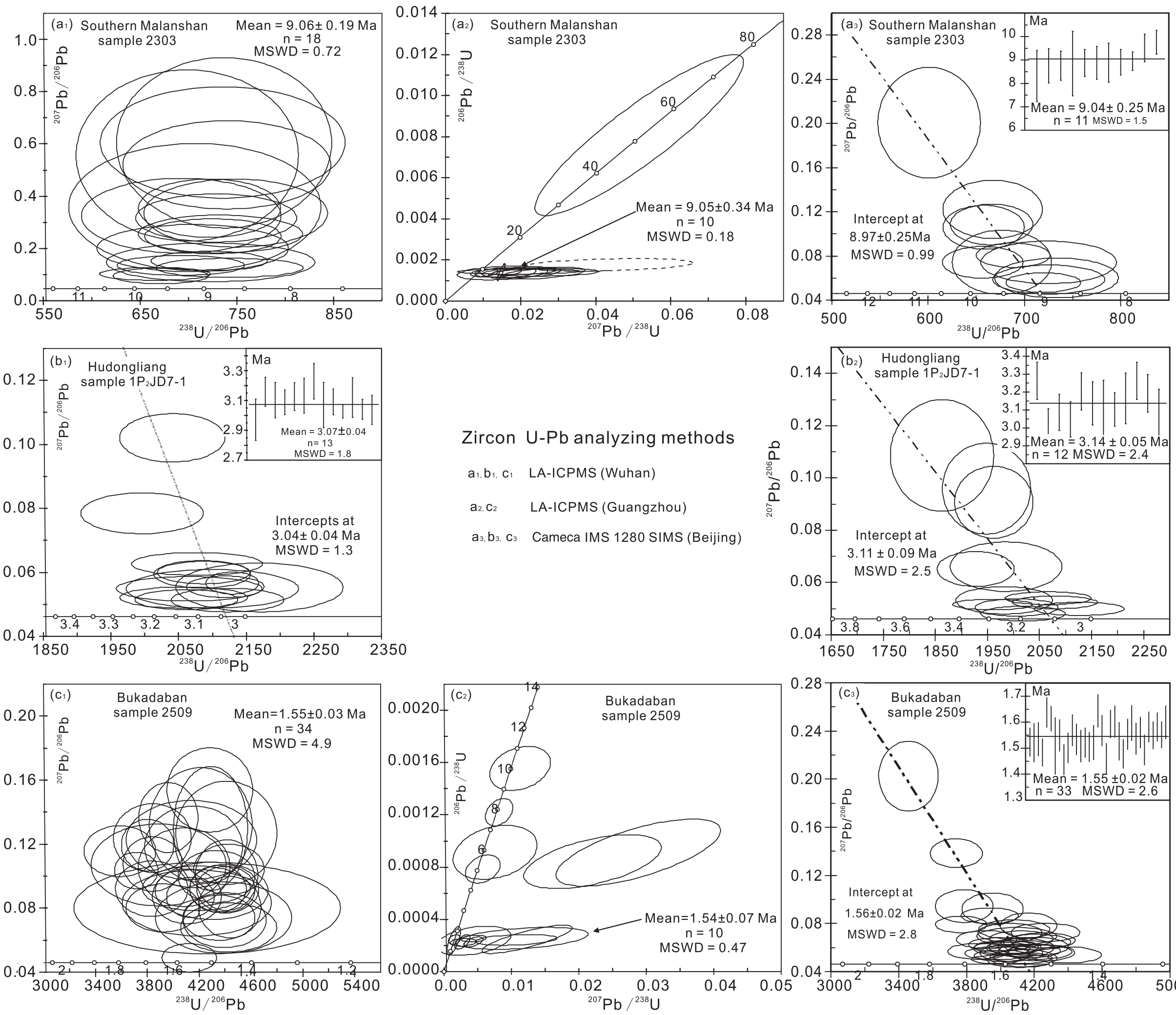

Fig. 6. Zircon U–Pb age plots. (a_1) LA-ICP-MS zircon U–Pb (Wuhan) Tera–Wasserburg plot for the southern Malanshan rhyolitic porphyry. (a_2) LA-ICP-MS zircon U–Pb (Guangzhou) concordia plot for the southern Malanshan rhyolitic porphyry. (a_3) CASIMS (Beijing) Zircon U–Pb Tera–Wasserburg plot for the southern Malanshan rhyolitic porphyry. (b_1) LA-ICP-MS zircon U–Pb (Wuhan) Tera–Wasserburg plot for the Hudongliang rhyolite. (b_2) CASIMS (Beijing) zircon U–Pb Tera–Wasserburg plot for the Hudongliang rhyolite. (c_1) LA-ICP-MS zircon U–Pb (Wuhan) Tera–Wasserburg plot for the Bukadaban rhyolite. (c_2) LA-ICP-MS zircon U–Pb (Guangzhou) concordia plot for the Bukadaban rhyolite. (c_3) CASIMS (Beijing) zircon U–Pb Tera–Wasserburg plot for the Bukadaban rhyolite. Wuhan: LA-ICP-MS (Agilent 7500) zircon U–Pb analyses at the National Key Laboratory of Geological Processes and Mineral Resources, Faculty of Earth Sciences, China University of Geosciences (Wuhan). Guangzhou: LA-ICP-MS (Agilent 7500) zircon U–Pb analyses at the State Key Laboratory of Isotope Geochemistry, Guangzhou Institute of Geochemistry (GIG), Chinese Academy of Sciences (CAS). Beijing: Cameca IMS-1280 ion microprobe (CASIMS) zircon U–Pb analyses at the Institute of Geology and Geophysics, CAS in Beijing.

metasedimentary rocks. Given that plagioclase is enriched in Eu and Sr (e.g. Defant & Drummond, 1990; Rapp *et al.*, 2003), the distinct negative Eu and Sr anomalies observed in the BM rhyolites (Fig. 9a–b) suggest the presence of residual plagioclase in their magma source region. The negative Ba, Sr, Nb and Ti anomalies in their primitive mantle-normalized trace element patterns (Fig. 9b) are also consistent with the presence of residual plagioclase, K-feldspar and biotite in the source region (e.g. Guo & Wilson, 2012).

Garnet is also a common residual phase during the melting of metasedimentary rocks under relatively high-pressure conditions. Garnet is especially rich in HREE and Y (e.g. Defant & Drummond, 1990; Rapp *et al.*, 2003) and the strongly depleted HREE and Y (Fig. 9a–b) abundances in primitive mantle-normalized trace element patterns suggest garnet as an additional residual phase in the BM rhyolite magma source region, as do the HREE characteristics of the BM rhyolite zircons (Fig. 4a–c). Guo & Wilson (2012) suggested that the

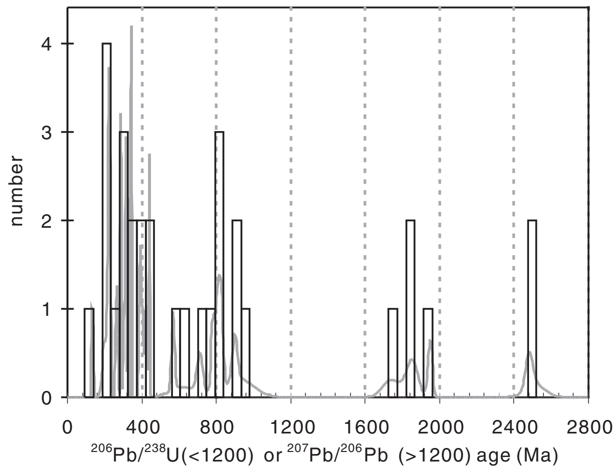

Fig. 7. Age distribution of old (>100 Ma) zircon crystals in the Bukadaban–Malanshan rhyolitic rocks. The zircon age data are from Tables 8–11.

positively correlated increase of La/Yb with Gd/Yb from the Higher Himalayan Leucogranites (HHL) in the south to the Tethyan Himalayan Leucogranites (THL) in the north (Fig. 13b) indicates that the amount of residual garnet in the source region of the leucogranites is higher in the THL than in the HHL. The strongly positive linear correlation between La/Yb and Gd/Yb for the Southern Malanshan, Bukadaban and Weixueshan rhyolites, along with their distinctly higher La/Yb and Gd/Yb ratios compared with the THL (Fig. 13b), suggests that the amount of residual garnet in their source region is higher than in either the THL or the HHL. However, the lower La/Yb and Gd/Yb of the Hudongliang tourmaline-bearing two-mica rhyolites indicates that the garnet content in their source was similar to that of the THL (Fig. 13b). Zircon REE patterns for the BM rhyolites support this distinction, given that those of the Southern Malanshan and

Table 11: Major (wt %) and trace (ppm) element and Nd–Sr–Pb isotope data for the Bukadaban-Malanshan rhyolites

Location:	Bukadaban			Southern Malanshan		Hudongliang		
Sample:	2509*	2059a†	2511-1*	2303*	2303a†	2011a*	$1P_2JD7$-1*	$1P_2JD7$-1a†
SiO_2	73·13	71·86	69·24	71·40	70·67	75·50	72·64	72·43
TiO_2	0·23	0·22	0·43	0·39	0·37	0·11	0·12	0·11
Al_2O_3	14·49	14·48	15·10	14·79	15·08	13·82	15·88	16·50
Fe_2O_3	1·49	2·80	1·82	1·37	1·90	0·30	1·09	1·34
FeO	0·30		1·25	0·75		1·20	0·40	
MnO	0·02	0·03	0·04	0·02	0·03	0·03	0·09	0·08
MgO	0·26	0·24	0·57	0·48	0·51	0·24	0·25	0·02
CaO	0·67	0·68	1·02	1·01	1·12	0·42	0·36	0·36
Na_2O	3·21	3·26	3·04	3·15	3·28	3·13	4·17	4·06
K_2O	5·08	5·03	5·47	5·23	5·42	4·13	3·95	4·14
P_2O_5	0·32	0·28	0·32	0·25	0·26	0·16	0·39	0·35
LOI	0·84	1·02	1·50	1·06	1·54	0·76	0·46	0·62
$\sum$	100·04	99·88	99·80	99·90	100·18	99·80	99·80	100·00
Mg#	0·22	0·14	0·26	0·30	0·35	0·23	0·24	0·04
ACNK	1·21	1·20	1·18	1·17	1·13	1·33	1·35	1·40
Sc	3·92	2·51	3·24	4·00	3·68	1·97	2·53	2·65
V	5·85	5·61	14·0	20·4	21·4	1·97	1·95	3·54
Cr	16·8	8·71	7·76	23·4	15·1		12·2	0·177
Co	1·61	2·35	3·40	3·12	3·61	0·85	1·07	1·24
Ni	0·81	3·49	53·0	31·5	10·3			0·078
Cu	8·37	19·3		10·2	11·4		3·29	8·52
Zn	84·7	76·3		79·6	78·2		88·8	86·0
Ga	28·2	26·1	25·8	27·1	26·4	24·4	35·3	31·9
Rb	586	545	476	425	418	454	923	810
Sr	28·7	42·7	71·5	90·9	113	30·8	6·75	9·29

(continued)

Table 11: Continued

Location:	Bukadaban			Southern Malanshan		Hudongliang		
Sample:	2509*	2059a†	2511-1*	2303*	2303a†	2011a*	$1P_2JD7$-1*	$1P_2JD7$-1a†
Y	7·01	6·83	9·84	6·07	6·75	5·50	4·02	4·79
Zr	84·1	101	170	152	165	48·2	57·8	52·9
Nb	27·0	24·7	20·9	14·3	12·5	20·4	48·0	41·4
Cs	28·9	26·6	35·6	15·3	15·2	111	244	188
Ba	72·8	98·0	225	245	303	69·7	32·6	27·6
La	27·6	31·9	79·8	42·2	48·5	11·5	10·0	11·5
Ce	64·0	68·7	177	96·7	103	24·1	22·4	24·3
Pr	6·86	8·24	19·7	10·3	12·3	2·80	2·42	2·81
Nd	25·4	28·9	71·2	38·3	43·3	9·87	8·32	10·1
Sm	4·65	5·10	11·6	6·32	7·09	2·08	1·66	2·01
Eu	0·18	0·202	0·45	0·54	0·543	0·14	0·053	0·042
Gd	3·45	3·25	5·86	4·92	4·24	1·27	1·23	1·51
Tb	0·49	0·370	0·77	0·60	0·408	0·21	0·21	0·226
Dy	2·03	1·51	3·01	2·45	1·60	0·85	1·01	1·04
Ho	0·29	0·211	0·37	0·36	0·225	0·16	0·18	0·155
Er	0·67	0·50	0·87	0·81	0·56	0·41	0·38	0·35
Tm	0·075	0·072	0·104	0·087	0·084	0·055	0·047	0·057
Yb	0·51	0·46	0·62	0·59	0·58	0·39	0·32	0·35
Lu	0·066	0·066	0·089	0·087	0·089	0·058	0·046	0·052
Hf	2·48	3·00	5·64	4·32	4·57	1·92	1·93	2·01
Ta	5·64	4·05	2·04	1·89	1·41	5·53	20·0	13·6
Pb	28·3	28·0	36·2	35·2	33·5	17·6	12·2	12·9
Th	34·6	35·4	103	48·9	47·2	13·0	12·0	12·9
U	10·6	11·0	23·7	8·54	9·36	9·18	14·5	14·2
Sr/Y	4·1	6·3	7·3	15·0	16·8	5·6	1·7	1·9
La/Yb	55	69	128	72	83	29	31	33
Nb/Ta	4·8	6·1	10·2	7·6	8·8	3·7	2·4	3·0
Th/La	1·3	1·1	1·3	1·2	1·0	1·1	1·2	1·1
T_{zr} (°C)‡	768	783	818	809	812	734	749	744
$T_{zr\text{-}av}$ (°C)§	790	810	740					
$^{147}Sm/^{144}Nd$	0·1111	0·1074	0·09914	0·1003	0·09952	0·1283	0·1217	0·1215
$^{143}Nd/^{144}Nd$	0·512329	0·512320	0·512338	0·512279	0·512290	0·512330	0·512256	0·512199
2σ	0·000007	0·000008	0·000011	0·000007	0·000008	0·000005	0·000005	0·000008
εNd(0)	–6·0	–6·2	–5·8	–7·0	–6·8	–6·0	–7·4	–8·6
T_{DM} (Ga)	1·2	1·2	1·1	1·2	1·1	1·5	1·5	1·6
$^{87}Rb/^{86}Sr$	59·18	36·93	19·26	13·52		42·67	396·0	
$^{87}Sr/^{86}Sr$	0·714225	0·713170	0·713011	0·714969		0·712485	0·717849	
2σ	0·00002	0·000016	0·000012	0·000017		0·000015	0·000015	
$^{206}Pb/^{204}Pb$	18·587		18·603	18·636		18·562	18·701	
$^{207}Pb/^{204}Pb$	15·554		15·562	15·613		15·493	15·630	
$^{206}Pb/^{204}Pb$	18·587		18·603	18·636		18·562	18·701	
$^{208}Pb/^{204}Pb$	38·533		38·522	38·742		38·309	38·699	

Mg# = $Mg^{2+}/(Mg^{2+} + Fe^{total})$; ACNK = $[Al_2O_3/(CaO + Na_2O + K_2O)]$ molar.
*Major elements for these samples were analysed at the Hubei Institute of Geology and Mineral Resource.
†Major elements for these samples were analysed at the State Key Laboratory of Isotope Geochemistry, Guangzhou Institute of Geochemistry, Chinese Academy of Sciences.
‡T_{zr}, zircon saturation temperature based on the whole-rock-Zr thermometer (Watson & Harrison, 1983).
§$T_{zr\text{-}av}$, average T_{zr}.

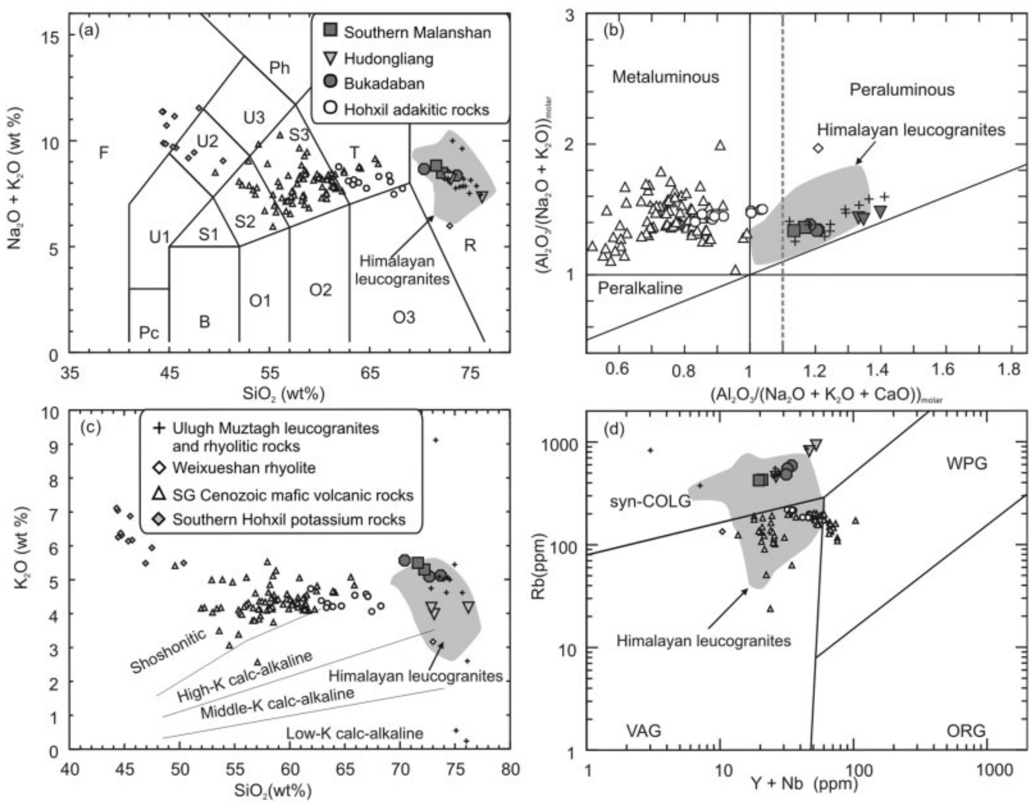

Fig. 8. Major and trace element geochemical characteristics of the Bukadaban–Malanshan rhyolitic rocks. (a) SiO_2 vs $Na_2O + K_2O$. All data plotted have been recalculated to 100 wt % on a volatile-free basis. Classification boundaries are from Le Bas *et al.* (1986). Rock types shown by letters are as follows: S1, trachybasalt; S2, basaltic trachyandesite; S3, trachyandesite; T, trachyte; U1, tephrite; U2, phonotephrite; U3, tephriphonolite; Ph, phonolite; Pc, picrobasalt; O1, basaltic andesite; O2, andesite; O3, dacite; F, foidite; R, rhyolite. (b) $[Al_2O3/(Na_2O + K_2O + CaO)]_{molar}$ vs $[Al_2O_3/(Na_2O + K_2O)]_{molar}$ diagram. (c) SiO_2 vs K_2O (after Peccerillo & Taylor, 1976). (d) Rb vs Y + Nb (after Pearce *et al.*, 1984). Data for the Songpan–Ganzi (SG) Cenozoic mafic volcanic rocks, and the Hohxil adakitic rocks and potassium rocks are from Arnaud *et al.* (1992), Turner *et al.* (1993, 1996), Chung *et al.* (2005), Wang *et al.* (2005), Guo *et al.* (2006) and references therein. Data for the Himalayan leucogranites are from Visonà & Lombardo (2002), Zhang *et al.* (2004), Searle (2006), Searle *et al.* (2007), Guo & Wilson (2012) and references therein. WPG, within-plate granite; syn-COLG, syn-collisional granite; VAG, volcanic arc granite; ORG, ocean ridge granite.

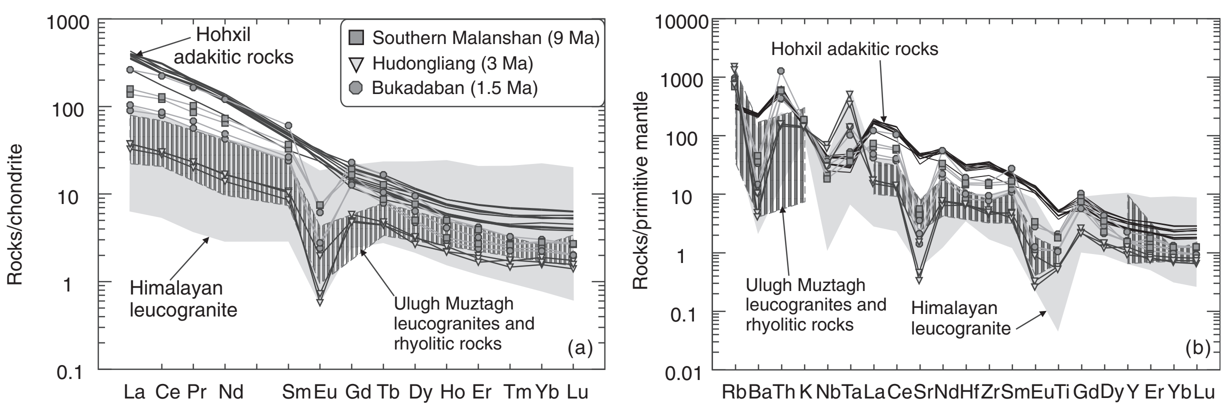

Fig. 9. (a) Chondrite-normalized rare earth element patterns for the BM rhyolites. (b) Primitive mantle normalized multi-element patterns for the BM rhyolites. Chondrite and primitive mantle values are from Sun & McDonough (1989). Data for the Himalayan leucogranites are from the same source as in Fig. 8. Data for the Ulugh Muztagh leucogranites and rhyolitic rocks are from McKenna & Walker (1990).

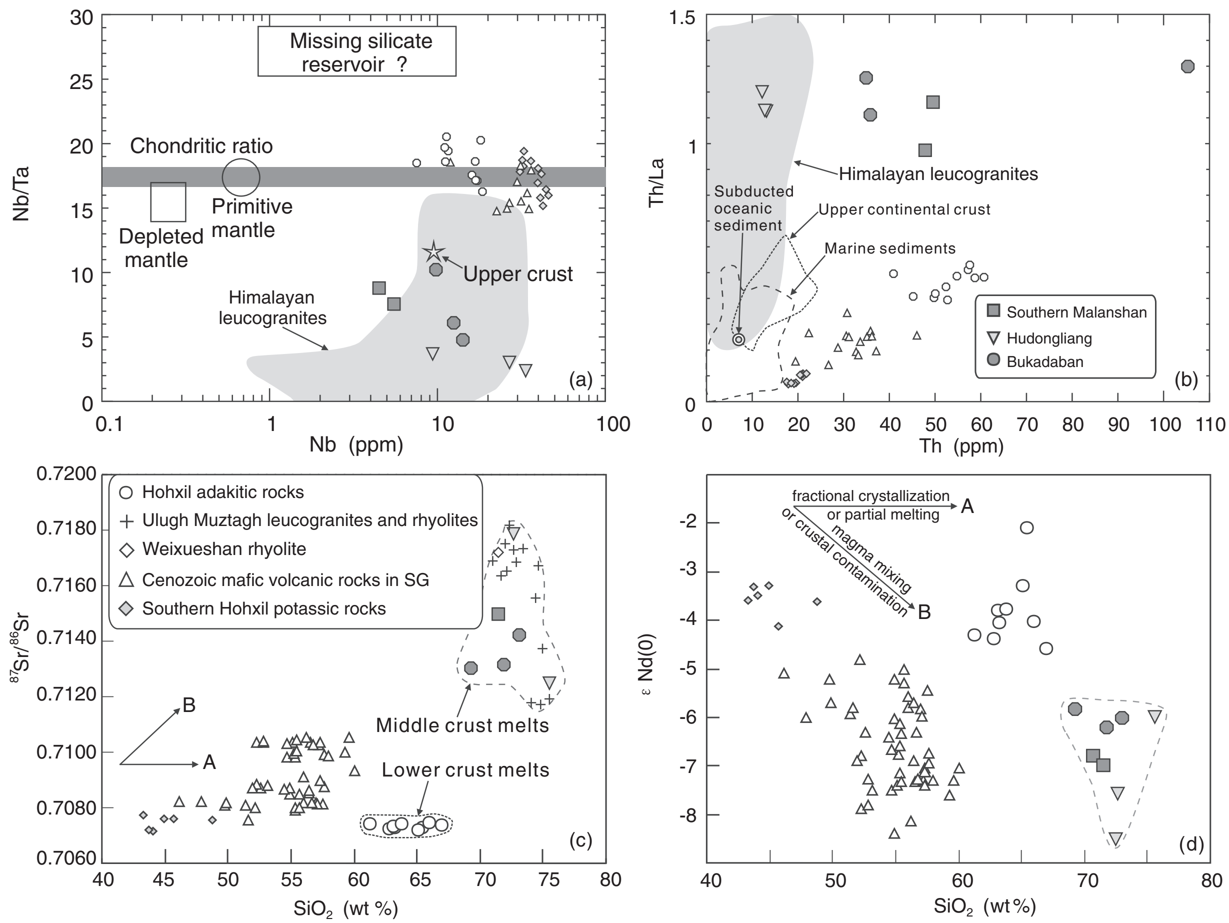

Fig. 10. (a) Nb vs Nb/Ta (Barth *et al*., 2000). (b) Th/La vs Th (Plank, 2005). (c) SiO_2 vs $^{87}Sr/^{86}Sr$. (d) SiO_2 vs εNd. The data for marine sediments and subducted oceanic sediment are from Plank & Langmuir (1998). The data for upper continental crust are from Condie (1993), Plank (2005), and references therein. The fields for primitive and depleted mantle, chondrites and the missing silicate reservoir in the Earth are from Barth *et al*. (2000) and references therein. Data for the Himalayan leucogranites are from the same source as in Fig. 8. Data for the Ulugh Muztagh and Weixueshan leucogranites and rhyolitic rocks are from McKenna & Walker (1990) and Jolivet *et al*. (2003), respectively. Data for the Songpan–Ganzi (SG) Cenozoic mafic volcanic rocks, and the Hohxil adakitic and potassic rocks are from the same source as in Fig. 8.

Bukadaban biotite rhyolites have HREE contents that are clearly lower than those of the garnet-free granulites and associated leucosomes in the same area, but similar to those from the garnet (+ feldspar)-bearing granulites and associated leucosomes in the Reynolds Range (Australia) (Rubatto, 2002; Rubatto & Hermann, 2007) (Fig. 4a–b). The Hudongliang tourmaline-bearing mica rhyolite exhibits slightly variable zircon HREE contents (Fig. 4c) and its zircon HREE patterns straddle the fields of garnet-bearing and garnet-free granulites and associated leucosomes of the Reynolds Range (Rubatto, 2002) (Fig. 4c), probably indicating minor garnet in the Hudongliang rhyolite source. In fact, melting experiments (e.g. Stevens *et al*., 1997; Patiño Douce & Harris, 1998; Castro *et al*., 2000; García-Casco *et al*., 2003) suggest that neoblastic garnet is often developed during the fluid-absent dehydration melting of metasedimentary rocks.

Temperature and pressure conditions for melting

The crystallization temperature of zircon was estimated using Ti-in-zircon thermometry (Watson & Harrison, 2005; Watson *et al*., 2006; Ferry & Watson, 2007). Spot locations were sampled adjacent to the spots for U–Pb analyses of the same zircons and have the same labels (Table 6). The crystallization temperatures of zircon were calculated using the revised calibration of the Ti-in-zircon thermometer (Ferry & Watson, 2007):

$$\log(\text{ppmTi-in-zircon}) = (5{\cdot}711 \pm 0{\cdot}072) - (4800 \pm 86)/T(\text{K}) - \log a\text{SiO}_2 + \log a\text{TiO}_2. \quad (1)$$

The calculated Ti-in-zircon temperatures are uncorrected for pressure. Because quartz is present in abundance in the BM rhyolites, $a\text{SiO}_2$ can be considered to be 1·0.

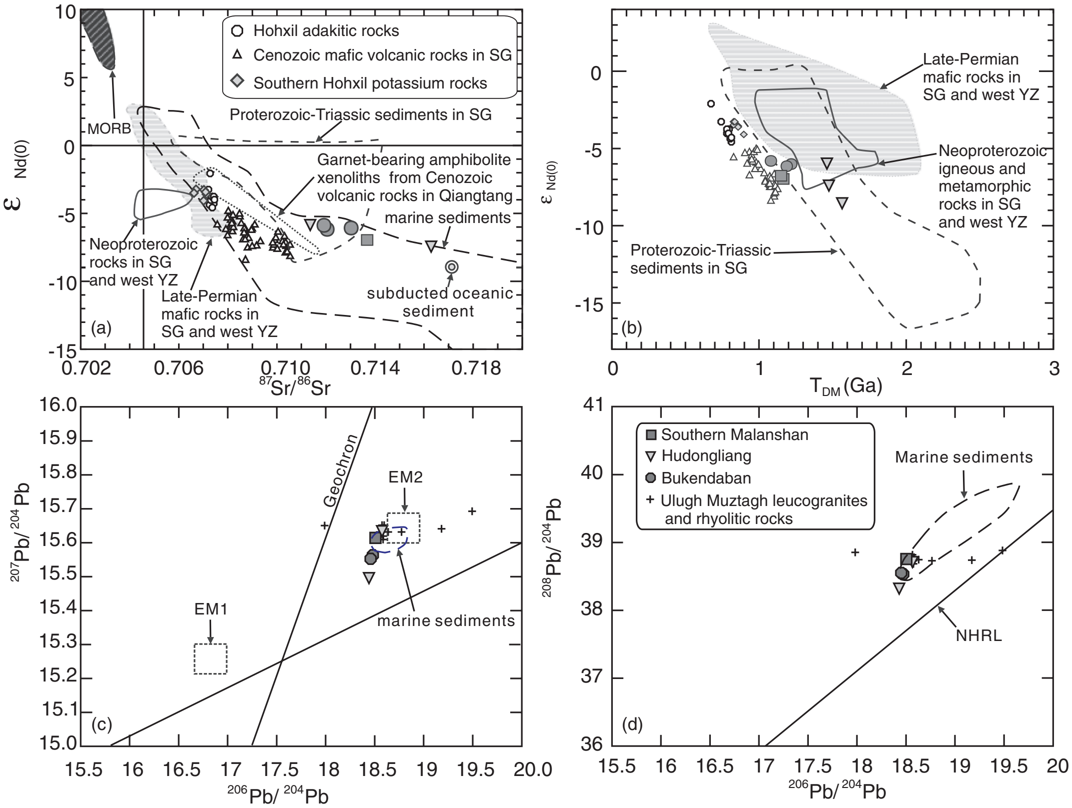

Fig. 11. Nd–Sr–Pb isotope variation in the Bukadaban–Malanshan rhyolitic rocks. (a) $^{87}Sr/^{86}Sr$ vs εNd(0). (b) T_{DM} (Ga) vs εNd(0). (c) $^{206}Pb/^{204}Pb$ vs $^{207}Pb/^{204}Pb$. (d) $^{206}Pb/^{204}Pb$ vs $^{208}Pb/^{204}Pb$. The fields for MORB, Neoproterozoic rocks and Late Permian mafic rocks in the Songpang–Ganzi (SG) and west Yantze Block (YZ) and garnet-bearing amphibolite xenoliths within Cenozoic volcanic rocks in the Qiangtang Block are after Wang *et al*. (2008). The field for marine sediments is constructed using the data of Plank & Langmuir (1998). Data for marine sediments and subducted oceanic sediment are from Plank & Langmuir (1998). Proterozoic–Triassic sediments in the Songpan–Ganzi Block are from Chen *et al*. (2006) and She *et al*. (2006). The Northern Hemisphere Reference Line (NHRL), EM1 and EM2 enriched mantle end-members are from Hart (1984), Zindler & Hart (1986) and Hofmann (1997). Data for the Ulugh Muztagh leucogranites and rhyolitic rocks are from the same source as in Fig. 10.

Table 12: Zircon in situ *Hf isotope data for the Bukadaban–Malanshan rhyolites*

Spots*	$^{176}Yb/^{177}Hf$	$^{176}Lu/^{177}Hf$	$^{176}Hf/^{177}Hf$	±2σ	T (Ma)	$\varepsilon_{Hf}(t)$	±2σ	T_{DM2} (Ga)
1P₂JD7-1								
1	0·076841	0·001699	0·282629	0·000011	3·0	–5·0	0·4	1·41
11	0·081123	0·001559	0·282521	0·000009	221·0	–4·3	0·3	1·53
2303								
8	0·017398	0·000392	0·282670	0·000011	9·0	–3·4	0·4	1·31
9	0·032530	0·000924	0·282777	0·000011	331	7·2	0·4	0·88
10	0·026741	0·000594	0·282715	0·000011	9·0	–1·8	0·4	1·21
11	0·031692	0·000715	0·282686	0·000012	9·0	–2·8	0·4	1·27
12	0·023349	0·000523	0·282697	0·000011	9·0	–2·4	0·4	1·25
13	0·032212	0·000697	0·282701	0·000012	10·3	–2·3	0·4	1·24
14	0·009867	0·000241	0·281235	0·000010	2514	1·7	0·3	2·91
15	0·017542	0·000415	0·282700	0·000010	9·0	–2·4	0·4	1·24
16	0·016545	0·000380	0·282714	0·000010	11·5	–1·8	0·4	1·21

(continued)

Table 12: Continued

Spots*	$^{176}Yb/^{177}Hf$	$^{176}Lu/^{177}Hf$	$^{176}Hf/^{177}Hf$	±2σ	T (Ma)	$\varepsilon_{Hf}(t)$	±2σ	T_{DM2} (Ga)
17	0·022047	0·000519	0·282689	0·000010	9·0	−2·7	0·4	1·27
18	0·079939	0·001918	0·282731	0·000010	315	5·1	0·4	1·00
19	0·025070	0·000573	0·282728	0·000011	9·0	−1·4	0·4	1·18
20	0·033162	0·000831	0·282557	0·000010	224	−2·8	0·4	1·44
21	0·055256	0·001327	0·282513	0·000012	443	0·2	0·4	1·41
22	0·039390	0·000861	0·282693	0·000012	9·0	−2·6	0·4	1·26
23	0·029814	0·000683	0·281503	0·000010	1836	−4·8	0·3	2·79
24	0·015955	0·000365	0·282713	0·000009	9·0	−1·9	0·3	1·22
25	0·025166	0·000566	0·282712	0·000011	9·0	−1·9	0·4	1·22
26	0·050770	0·001245	0·282679	0·000013	286	2·8	0·5	1·13
27	0·055236	0·001278	0·281782	0·000010	343	−27·8	0·4	3·09
28	0·023483	0·000497	0·282722	0·000011	9·0	−1·6	0·4	1·20
29	0·017751	0·000390	0·282704	0·000011	18·0	−2·0	0·4	1·23
30	0·116612	0·002620	0·282876	0·000012	136	6·4	0·4	0·78
31	0·030031	0·000745	0·282705	0·000015	9·0	−2·2	0·5	1·23
32	0·019722	0·000442	0·282692	0·000009	9·0	−2·6	0·3	1·26
33	0·029589	0·000645	0·282705	0·000008	9·0	−2·2	0·3	1·23
34	0·018644	0·000466	0·281555	0·000008	1854	−2·3	0·3	2·64
35	0·020723	0·000460	0·282704	0·000011	9·0	−2·2	0·4	1·24
36	0·023276	0·000512	0·282747	0·000010	9·0	−0·7	0·4	1·14
2509								
1	0·001983	0·000034	0·282607	0·000009	5·6	−5·7	0·3	1·46
2	0·001757	0·000031	0·282658	0·000011	5·6	−3·9	0·4	1·34
3	0·013044	0·000289	0·282629	0·000010	10·9	−4·8	0·4	1·40
4	0·022766	0·000610	0·282718	0·000011	6·1	−1·8	0·4	1·21
6	0·005411	0·000123	0·282639	0·000011	7·7	−4·5	0·4	1·38
7	0·032829	0·000771	0·282684	0·000010	1·5	−3·1	0·4	1·28
8	0·034195	0·000765	0·282849	0·000014	6·7	2·9	0·5	0·91
9	0·039467	0·000927	0·282705	0·000012	1·5	−2·3	0·4	1·24
10	0·032951	0·000769	0·282652	0·000016	1·5	−4·2	0·6	1·36
11	0·007578	0·000178	0·282092	0·000013	802	−6·4	0·5	2·10
12	0·041948	0·001078	0·282749	0·000014	1·5	−0·8	0·5	1·14
13	0·056429	0·001533	0·282699	0·000013	1·5	−2·5	0·5	1·25
14	0·030200	0·000829	0·282658	0·000012	1·5	−4·0	0·4	1·34
15	0·003137	0·000062	0·282602	0·000010	5·4	−5·9	0·4	1·47
16	0·034211	0·000833	0·282664	0·000009	1·5	−3·8	0·3	1·33
17	0·064844	0·001820	0·282300	0·000052	228·0	−12·0	1·8	2·02
18	0·042913	0·001043	0·282638	0·000012	1·5	−4·7	0·4	1·39
19	0·044171	0·001078	0·282760	0·000016	1·5	−0·4	0·6	1·11
20	0·043022	0·000990	0·282696	0·000010	1·5	−2·6	0·4	1·26
21	0·064677	0·001453	0·282646	0·000011	1·5	−4·4	0·4	1·37
22	0·056706	0·001673	0·282530	0·000028	5·4	−8·5	1·0	1·63

Zircon *in situ* Hf isotope analyses were conducted on a Neptune, multi-collector, ICP-MS system equipped with a Geolas-193 laser ablation system, at the State Key Laboratory of Isotope Geochemistry, Guangzhou Institute of Geochemistry, Chinese Academy of Sciences.
*Analytical spots for zircon *in situ* Hf isotope compositions of samples 2303 and 2509 are the same as those for zircon *in situ* U–Pb ages in Table 10. Analytical spots for zircon *in situ* Hf isotope compositions of sample $1P_2JD7$-1 are the same as those for zircon *in situ* U–Pb ages in Table 8.

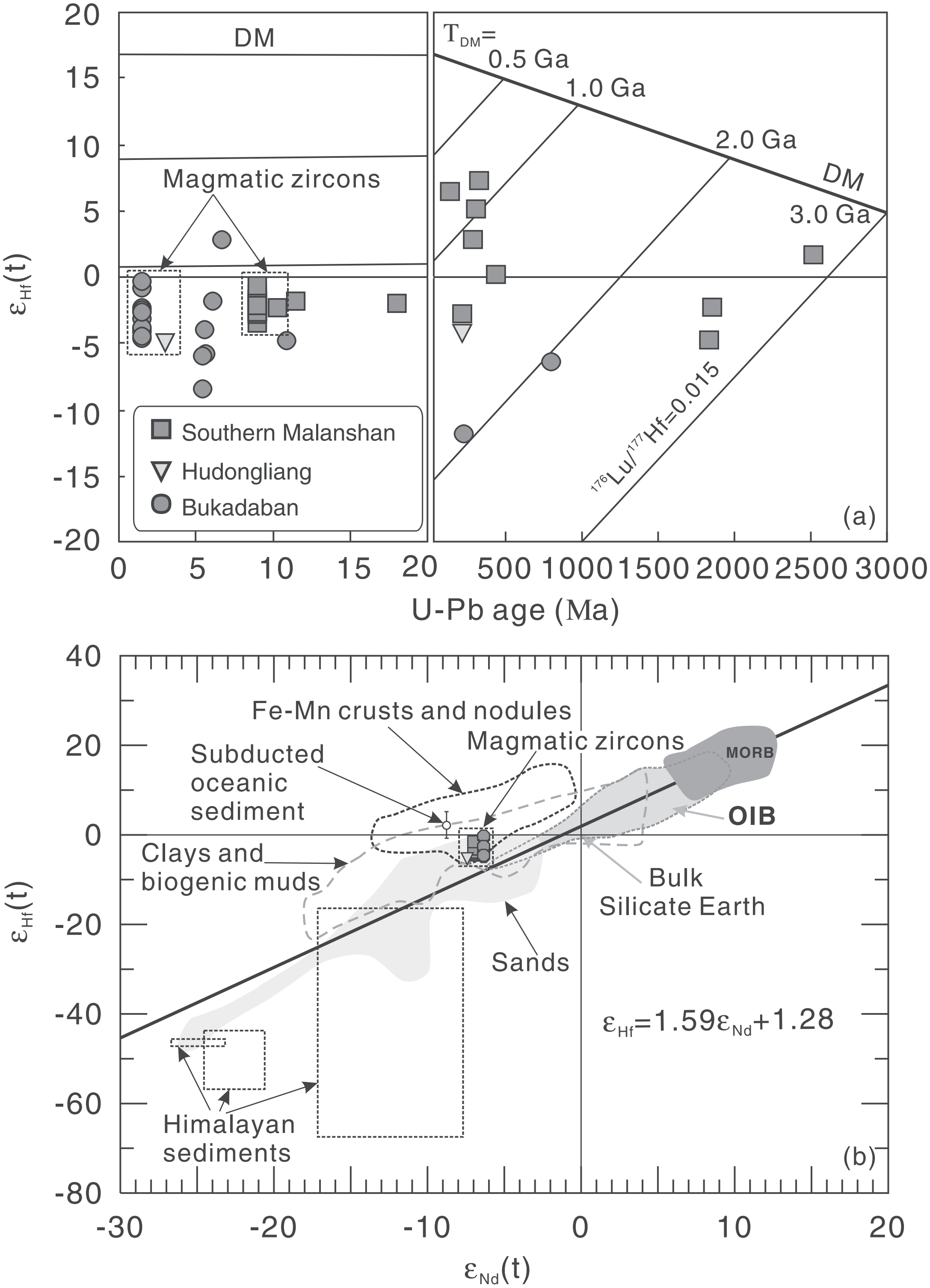

Fig. 12. (a) εHf(t) vs zircon U–Pb age (Ma). (b) εHf(t) vs εNd(t) (Chauvel *et al.*, 2008). DM, depleted mantle; MORB, mid-ocean ridge basalts; OIB, ocean island basalts. The fields for MORB, OIB and sediments (Fe–Mn crusts and nodules, subducted oceanic sediment, clays and biogenic muds, sands and Himalayan sediments) are after Richards *et al.* (2005), Chauvel *et al.* (2008) and references therein.

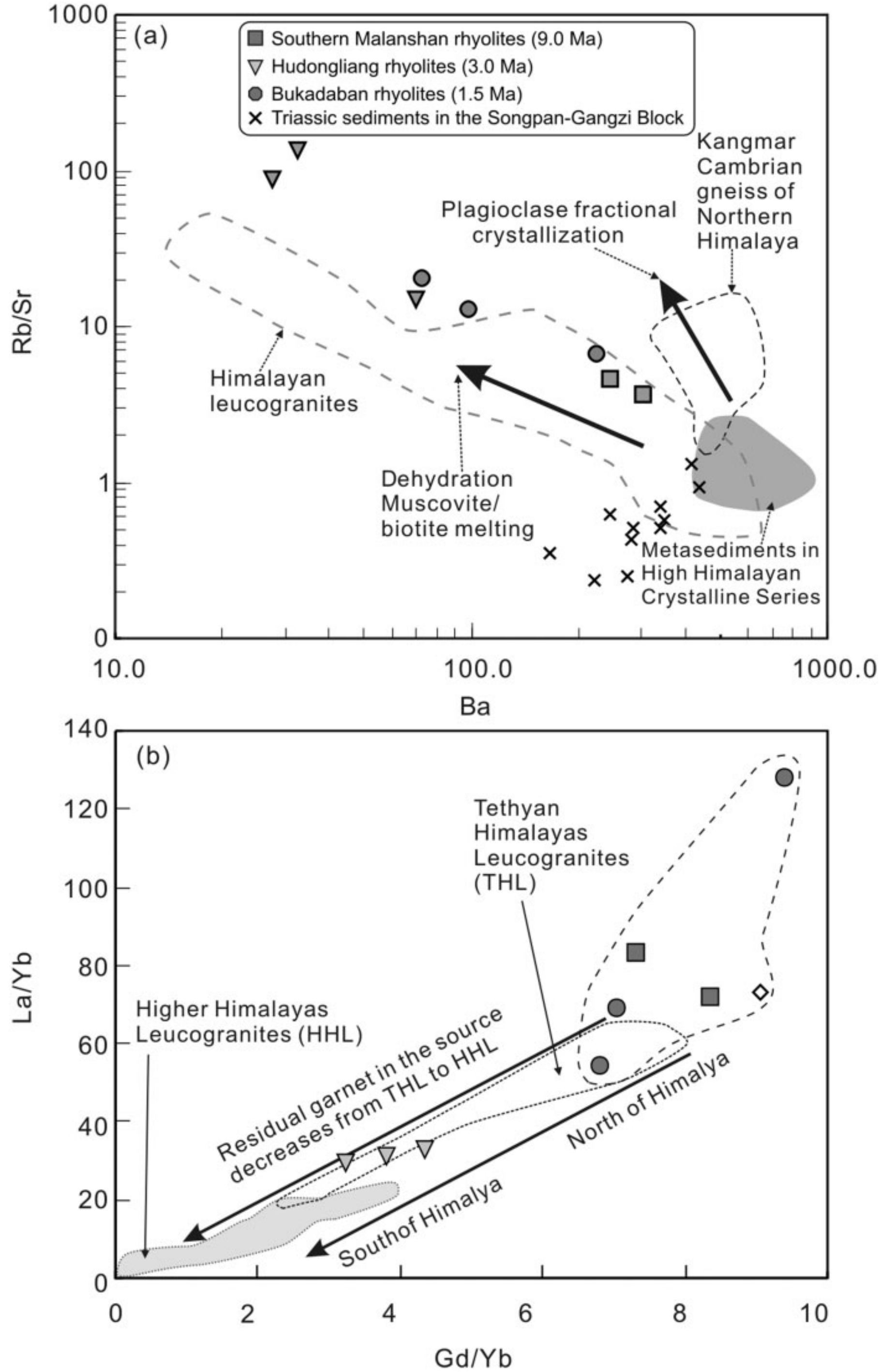

Fig. 13. (a) Rb/Sr vs Ba (ppm) (Zhang *et al*., 2004); (b) La/Yb vs Gd/Yb (Guo & Wilson, 2012). Data for the Kangmar Cambrian gneiss of the Northern Himalaya, metasediments of the High Himalayan Crystalline Series and Himalayan leuogranites are from Inger & Harris (1993) and Zhang *et al*. (2004). The trends for dehydration muscovite/biotite melting and plagioclase fractional crystallization are from Inger & Harris (1993) and Zhang *et al*. (2004). Data for Triassic sediments in the Songpan–Gangzi Block are from She *et al*. (2006). The fields for the Higher Himalayan Leucogranites (HHL) and the Tethyan Himalayan Leucogranites are from Guo & Wilson (2012).

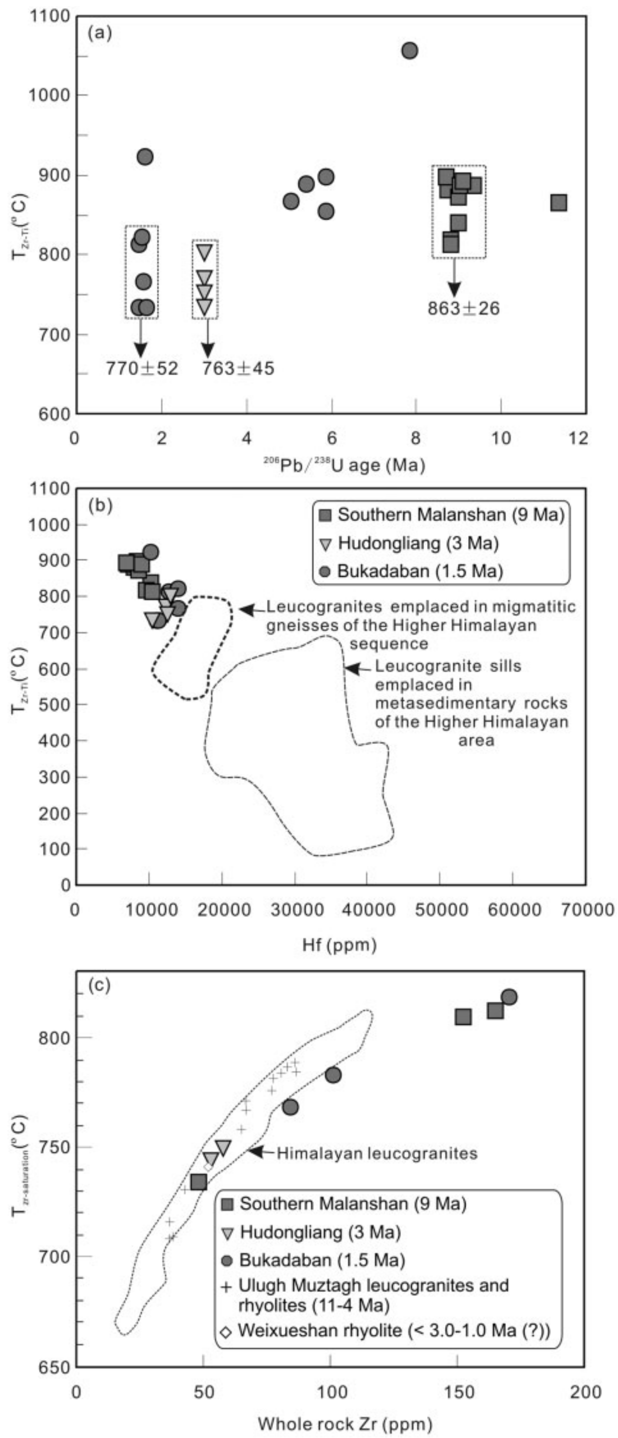

Fig. 14. (a) Titanium in zircon temperatures ($T_{Zr\text{-}Ti}$) (after Ferry & Watson, 2007) vs $^{206}Pb/^{238}U$ age. (b) $T_{Zr\text{-}Ti}$ vs Hf content for zircons. (c) $T_{zr\text{-}saturation}$ (zircon saturation temperature) (Watson & Harrison, 1983) vs whole-rock Zr content. $T_{Zr\text{-}Ti}$ values, $^{206}Pb/^{238}U$ ages and Hf contents are from Table 6. The fields for leucogranites emplaced in migmatitic gneisses of the Higher Himalayan sequence and leucogranite sills emplaced in metasedimentary rocks of the Higher Himalayan sequence (Fig. 14b) are after Kellett et al. (2009). The data for the Himalayan leucogranites in (c) are from the same souce as in Fig. 8.

For most igneous rocks, $\acute{a}TiO_2$ is $\geq$0·5 (Watson & Harrison, 2005; Watson *et al.*, 2006). The studied rhyolites do not contain any Ti-bearing phases such as rutile, an indication that $\acute{a}TiO_2$ is <1·0 (Watson & Harrison, 2005; Watson *et al.*, 2006). Our data are calculated for $\acute{a}TiO_2 = 0{\cdot}5$ (Fig. 14a; Table 6) and probably represent maximum temperatures (Kellett *et al.*, 2009). The calculated Ti-in-zircon temperatures for the southern Malanshan, Hudongliang and Bukadaban rhyolites give $T_{Zr\text{-}Ti}$ ($t = 9{\cdot}0$ Ma) $= 863 \pm 26$°C, $T_{Zr\text{-}Ti}$ ($t \sim 3{\cdot}0$ Ma) $= 763 \pm 45$°C, and $T_{Zr\text{-}Ti}$ ($t = 1{\cdot}5$ Ma) $= 770 \pm 52$°C. The temperatures are clearly higher than those of the Higher Himalayan leucogranites (Fig. 14b), which represent the maximum-crystallization temperatures of zircons from leucogranites (Kellett *et al.*, 2009). However, we suggest that these temperatures probably represent the maximum-melting temperatures of their respective BM rhyolite magmas. Further evidence is provided by the zircon saturation temperatures (T_{Zr}) (Watson & Harrison, 1983) estimated from the whole-rock major element contents of the southern Malanshan, Hudongliang and Bukadaban rhyolites, which have average T_{zr} values of 810, 740 and 790°C, respectively (Table 11; Fig. 14c). The Zr contents of the BM rhyolitic rocks may have been elevated by the inheritance of abundant old zircons (Fig. 7), which would cause $T_{zr\text{-}saturation}$ (zircon saturation temperature) values based on whole-rock Zr contents to be higher than the melting temperature of their host rocks. Therefore, in combination with Ti-in-zircon temperatures (Fig. 14a; Table 6), the T_{Zr} values indicate maximum-melting temperature ranges for the southern Malanshan, Hudongliang and Bukadaban rhyolitic magmas of 810–863°C, 740–763°C and 770–790°C, respectively.

The southern Malanshan and Bukadaban biotite rhyolites have relatively high magma temperatures compared with the Hudongliang tourmaline-bearing mica rhyolites. Comparable relationships exist between Himalayan biotite and tourmaline leucogranites and their respective high and low zircon saturation temperatures (Searle *et al.*, 1997). Therefore, the Himalayan tourmaline leucogranites (e.g. Inger & Harris, 1993; Searle *et al.*, 1997; Searle & Godin, 2003) and Hudongliang rhyolites most plausibly represent low-temperature, primary, near-minimum melts. Conversely, the southern Malanshan and Bukadaban rhyolites were generated at higher temperatures and high degrees of anatectic melting driven by biotite dehydration, similar to the process suggested for the Himalayan biotite leucogranites (e.g. Inger & Harris, 1993; Searle *et al.*, 1997; Zhang *et al.*, 2004). This may be the reason why the southern Malanshan and Bukadaban rhyolitic rocks have relatively high REE, TiO_2, MgO and FeO^{total} contents compared with the Hudongliang rhyolites, given that the experimental work of Montel (1993) showed that with

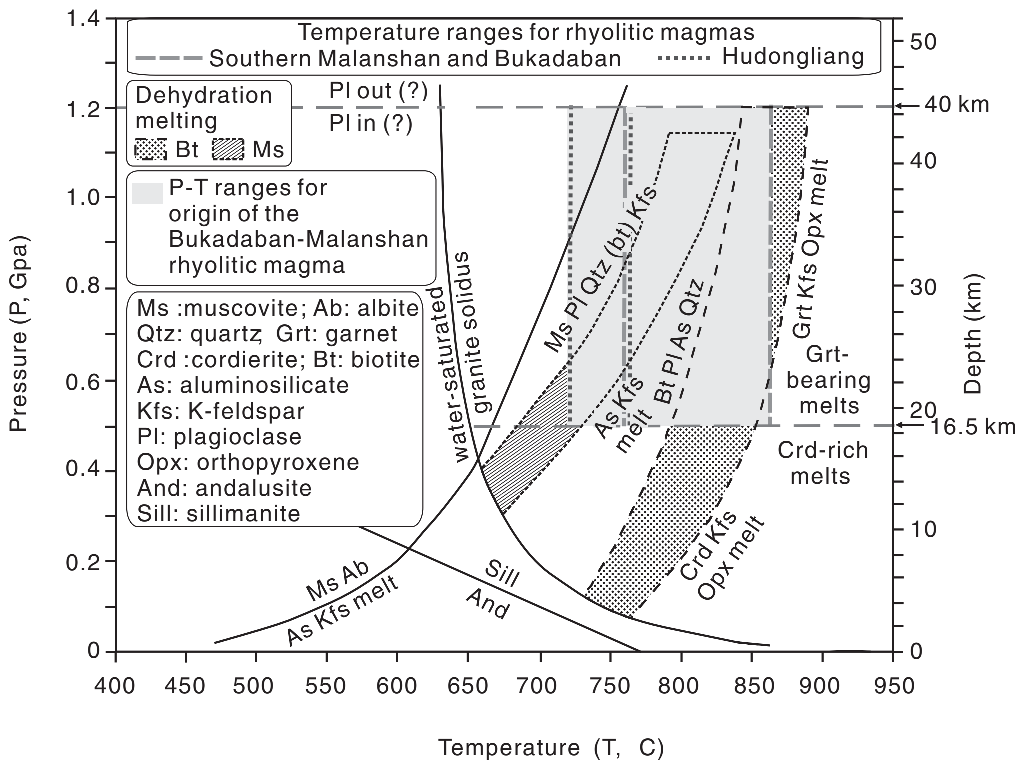

Fig. 15. *P–T* diagram showing conditions for rhyolitic magma generation (after Dini *et al.*, 2005). The lower limit for garnet stability is after Stevens *et al.* (1997), Patiño Douce & Harris (1998), Castro *et al.* (2000) and García-Casco *et al.* (2003). The upper limit for plagioclase stability is after Rapp & Watson (1995), Rapp *et al.* (2003) and Patiño Douce (2005).

increasing temperature there is a strong increase in melt REE content.

The pressure–temperature conditions associated with the formation of the BM rhyolitic magmas can be further constrained by experimental data. For example, at pressures of 0·5–1·0 GPa, muscovite breakdown can be initiated at 720–770°C (Patiño Douce & Harris, 1998) and biotite breakdown at 760–830°C (Le Breton & Thompson, 1998; Koester *et al.*, 2002). In addition, experimental data suggest that garnet can start to form at pressures of 0·5–0·6 GPa and temperatures of 750–900°C during fluid-absent melting of metasedimentary rocks (e.g. Stevens *et al.*, 1997; Patiño Douce & Harris, 1998; Castro *et al.*, 2000; García-Casco *et al.*, 2003), indicating that the lower limit of garnet stability is 0·5 GPa (Fig. 15). Plagioclase is a common residual mineral during fluid-absent melting of a variety of crustal rocks including metasedimentary rocks and igneous rocks (e.g. tonalites and basalts), but it disappears at pressures of >1·2–1·5 GPa (e.g. Rapp & Watson, 1995; Rapp *et al.*, 2003; Patiño Douce, 2005), indicating that the upper limit of plagioclase stability is 1·2 GPa (Fig. 15). Taking into account the above mineral (garnet and plagioclase) and pressure–temperature data, we conclude that the Malanshan and Bukadaban rhyolitic magmas were generated by muscovite ± biotite dehydration melting of metasedimentary rocks at a temperature and pressure range of 760–863°C and 0·5–1·2 GPa, respectively (Fig. 15), and the Hudongliang rhyolitic magmas by muscovite dehydration melting at a slightly lower temperature range of 720–763°C and the same pressure range (Fig. 15).

Heat source for crustal melting

Geophysical data suggest that there is hotter lithospheric mantle beneath central–northern Tibet compared with southern Tibet (Owens & Zandt, 1997; Tilmann *et al.*, 2003). Partial melting of such a thickened lithospheric mantle produced Cenozoic potassic mafic magmas in northern Tibet (Arnaud *et al.*, 1992; Turner *et al.*, 1993, 1996; Chung *et al.*, 2005; Guo *et al.*, 2006), which was probably heated by an upwelling asthenosphere squeezed between the northward advancing Indian and the resisting Qaidam and Tarim lithospheres (e.g. Turner *et al.*, 1993, 1996; Chung *et al.*, 2005; Guo *et al.*, 2006) or an upwelling asthenospheric counterflow coupled with northward downwelling Indian mantle lithosphere or southward downwelling Asian mantle lithosphere (Owens & Zandt, 1997; Kind *et al.*, 2002; Tilmann *et al.*, 2003; Priestley *et al.*, 2006). Furthermore, the conducted heat from the underlying hot lithospheric mantle heated the mid- to lower crust, which melted to form the partially molten crustal layers

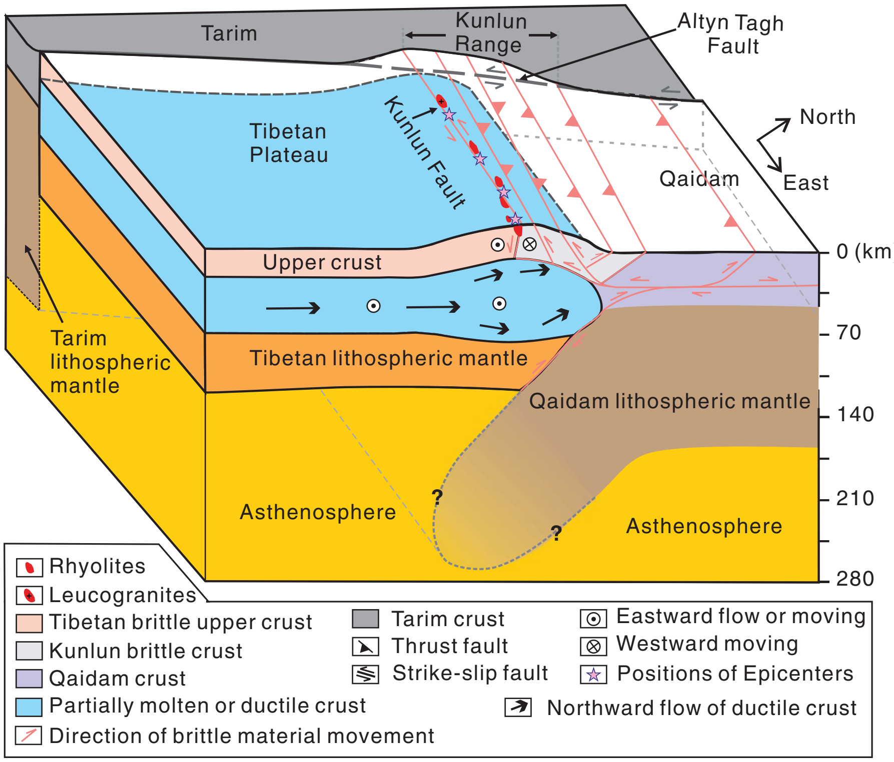

Fig. 16. A model for crustal flow causing crustal magmatism, crustal thickening, earthquakes and surface uplift along the northern margin of the Tibetan Plateau. The model is developed based on ideas and/or data in the following references: Owens & Zandt (1997); Zhu & Helmberger (1998); Cowgill *et al.* (2003); Tilmann *et al.* (2003); Chung *et al.* (2005); Royden *et al.* (2008); Yin *et al.* (2008*b*); Shi *et al.* (2009); Karplus *et al.* (2011); Le Pape *et al.* (2012). Fault zones in the Kunlun Ranges are after Meyer *et al.* (1998), Jolivet *et al.* (2003), Xu *et al.* (2006) and Yin *et al.* (2008*b*).

in northern Tibet. Alternatively, or additionally, radioactive decay in the thickened crust may also have provided a heat source for crustal melting and the generation of felsic magmas (e.g. Jamieson *et al.*, 1998; Huerta *et al.*, 1999; McKenzie & Priestley, 2008). During India–Eurasia convergence or Pre-Cenozoic subduction, Triassic sedimentary rocks of the Songpan–Ganzi terrane may have been added to the mid- to lower crust beneath central–northern Tibet (Meyer *et al.*, 1998; Yin & Harrison, 2000; Tapponnier *et al.*, 2001; Kapp *et al.*, 2003, 2005). These sedimentary rocks contain high concentrations of radioactive elements and were probably easily melted by their own radioactive heat. Based on a simulation by McKenzie & Priestley (2008), for example, the temperature of these sedimentary rocks could readily exceed the granite solidus in the thickened lower crust.

GEODYNAMIC IMPLICATIONS

Crustal melting as an explanation for low-velocity zones in central–northern Tibet

The discovery of granulite xenoliths exhumed in 3 Ma basaltic rocks in the Qiangtang Block showed that the lower crust in central–northern Tibet may be both hot and dry (Hacker *et al.*, 2000). These granulite xenoliths have been widely viewed as evidence against crustal melting in central–northern Tibet (e.g. Tapponnier *et al.*, 2001; Wei *et al.*, 2001; Cowgill *et al.*, 2003; Unsworth *et al.*, 2004; Klemperer, 2006). As a result, various alternative interpretations of the crustal low-velocity zones at 15–50 km depth in the crust of central–northern Tibet have been suggested, including crustal shearing, preferred orientation of micas, the presence of aqueous fluids, underplating of mantle-derived melts, or the separation between an upper felsic and a lower mafic part in the crust (e.g. Tapponnier *et al.*, 2001; Wei *et al.*, 2001; Vergne *et al.*, 2002; Shapiro *et al.*, 2004; Unsworth *et al.*, 2004; Klemperer, 2006). However, our data suggest that the BM rhyolites resulted from partial melting of metasedimentary rocks at ~0·5–1·2 GPa, corresponding to depths of ~16–40 km (Fig. 15) in the mid- to lower crust of the Songpan–Ganzi Block, which has total crustal thickness of 60–70 km (e.g. Zhu & Helmberger, 1998; Vergne *et al.*, 2002; Shi *et al.*, 2009; Karplus *et al.*, 2011). In combination with the nearby occurrences of 18–15 Ma adakitic rocks that originated from partial melting of an eclogitic mafic lower crust at depths of more than ~40–50 km (Wang *et al.*, 2005) or 60 km (Hetényi *et al.*, 2007) (Fig. 1), we envisage the existence of crustal melting beneath the region at variable depths of *c.* 16–50 km, mainly in the mid- to lower crust. This estimate is in good agreement with the depths of *c.* 15–50 km for the observed abnormally weak layers or lower seismic velocity zones in northern Tibet (Owens & Zandt, 1997; Wei *et al.*, 2001; Unsworth *et al.*, 2004; Klemperer, 2006). Our petrological data, therefore, lend strong support to the argument that these layers are partially molten zones. Moreover, the ~3·0–1·5 Ma rhyolites from the Bukadaban and Hudongliang areas are coeval with, or younger than, the 3 Ma basaltic rocks that contain granulite xenoliths in central Tibet (Hacker *et al.*, 2000), and stand as the first petrological evidence for Tibetan crustal melting in the Quaternary. Together with the southern Malanshan (~9·0 Ma) and Ulugh Muztagh (11–4 Ma) leucogranites and rhyolites, and the Hohxil adakitic rocks (18–15 Ma), these data suggest a rather long-lived history of crustal melting from the mid-Miocene to Recent beneath northern Tibet.

Northward crustal flow and growth of the Tibetan Plateau

Partially molten layers have important implications for the weakening and flow of the mid- to lower crust and the growth of the Tibetan Plateau (Owens & Zandt, 1997; Medvedev & Beaumont, 2006). Under regional north–south compression caused by the northward subduction of the Indian continent and the southward subduction of the Asian continent (e.g. Nábelek *et al.*, 2009; Capitanio *et al.*, 2010; Zhao *et al.*, 2010, 2011), the mid- to lower crust, weakened by partially molten layers in central–northern Tibet, may flow northward owing to the horizontal pressure gradient along the crustal channel. In southern Tibet, beneath the Himalayan orogen, many geophysical observations (e.g. Nelson *et al.*, 1996; Unsworth *et al.* 2005; Ashish *et al.*, 2009; Zhang & Klemperer, 2010) suggest that partial melting and a resultant weaker crustal channel probably dominate in the middle crust. Ductile extrusion of the Greater Himalayan Sequence has, therefore, been attributed to southward flow of such weakened middle crust between *c.* 28 and 9 Ma (e.g. Grujic *et al.*, 1996, 2002; Zhang *et al.*, 2004; Grujic, 2006; Searle *et al.*, 2006, 2007, 2009; Harris, 2007; King *et al.*, 2011). In eastern Tibet, the weakened mid- to lower crust could have flowed dominantly eastward towards and around the Sichuan Basin (Clark & Royden, 2000; McKenzie *et al.*, 2000; DeCelles *et al.*, 2002; McKenzie & Jackson, 2002; Clark *et al.*, 2005; Enkelmann *et al.*, 2006; Royden *et al.*, 2008; Yao *et al.*, 2008; Bai *et al.*, 2010), causing crustal thickening, surface uplift and the latest earthquakes along the eastern margin of the Tibetan Plateau (Fig. 1a) (Burchfiel *et al.*, 2008; Royden *et al.*, 2008).

In central–northern Tibet, the weak channel caused by crustal partial melts is likely to exist in the mid- to lower crust or even upper mantle, with eastward flow (e.g. Huang *et al.*, 2000; Wei *et al.* 2001; Cowgill *et al.*, 2003; Meissner *et al.* 2004; Wang *et al.*, 2010). Recent geophysical studies also suggest that there is a possible northward lower crustal flow, which caused the crustal thickening and northward growth of the northern Tibetan Plateau (Zhu & Helmberger, 1998; Karplus *et al.*, 2011). Geophysical data show that the crustal thickness of the northern Tibetan Plateau just south of the Qaidam Basin is about 60–70 km, which is significantly thicker than the *c.* 45 km thick crust in the Qaidam Basin (Zhu & Helmberger, 1998; Vergne *et al.*, 2002; Shi *et al.*, 2009; Karplus *et al.*, 2011). Moreover, a 15–20 km Moho offset separates the thick Tibetan Plateau crust to the south from the Qaidam Basin crust to the north (Zhu & Helmberger, 1998; Shi *et al.*, 2009; Karplus *et al.*, 2011), and the southernmost lower crust of the Qaidam Basin is underlain by the northernmost lower crust of the Tibetan Plateau (Shi *et al.*, 2009; Karplus *et al.*, 2011). The apparently overlapping crustal material may represent Songpan–Ganzi lower crust underthrusting or northward flow beneath the Qaidam Basin Moho (Karplus *et al.*, 2011). Thus the high Tibetan Plateau may be thickening northward into south Qaidam as weak, thickened, lower crust is injected beneath stronger Qaidam crust (Karplus *et al.*, 2011). However, such a Moho offset has also been interpreted as evidence against a significant ductile flow in the lower crust across the Kunlun–Qaidam border and in favour of either successive stacking of crustal thrust wedges as the mechanism for the northeastward growth of the plateau (Vergne *et al.*, 2002) or a south-directed fault ramp along which the Qaidam lower crust and mantle lithosphere have subducted beneath the northern Kunlun Range (Meyer *et al.*, 1998; Yin *et al.*, 2008*b*).

We argue that there is a trend of northward propagation in the occurrence of crustal melt-enhanced ductile flow and inflation, with the present crustal bulge being located in northern Tibet (Fig. 16), based on the crustal thickness and Moho offset data mentioned above and the following lines of evidence.

(1) The Ulugh Muztagh, Weixueshan, Bukadaban, Hudongliang and southern Malanshan leucogranites and rhyolitic rocks, as well as the western Wuxuefeng adakitic rocks (Fig. 1c), constitute an approximately east–west-trending zone of Miocene–Quaternary crust-derived magmatic rocks (Fig. 1b and c). This zone is close to the Kunlun Fault Zone in the southern Kunlun Ranges (Fig. 1b and c). The main peaks or glaciers (e.g. Ulugh Muztagh, Bukadaban, Malanshan, Weixueshan, Wuxuefeng, Daxue and Yuzhufeng) of the Kunlun Ranges are also distributed along the Kunlun Fault Zone and exhibit approximately the same trend as that of the Miocene–Quaternary crust-derived magmatic rocks (Fig. 1b and c), indicating a possible relationship between crustal melting,

fault activity and surface uplift of the northern Tibetan margin (Van der Woerd *et al.*, 2002; Tocheport *et al.*, 2006).

(2) The Kunlun Fault Zone has traditionally been identified as a significant rheological boundary (Unsworth *et al.*, 2004) between weak, warm Tibetan crust (Klemperer, 2006) and the rigid eastern Kunlun–Qaidam block. However, the northernmost extension of low seismic wave velocity zones lies beneath the southern part of the Kunlun Ranges (Owens & Zandt, 1997; Wei *et al.*, 2001; Unsworth *et al.* 2004; Klemperer, 2006), corresponding to the Kunlun Fault Zone and the Ulugh Muztagh–Wuxuefeng crust-derived magmatic zone exposed at the surface (Fig. 1c). Moreover, the reanalyses and remodelling of existing magnetotelluric data (Le Pape *et al.*, 2012) show that a crustal melt at a depth of 20–45 km penetrates beyond the Kunlun Fault Zone into northern Tibet and compromises the previous identification of this fault zone as an important rheological boundary. Conversely, there is no low seismic velocity zone in the crust beneath the northern Kunlun Ranges and the Qaidam Block (Wei *et al.*, 2001; Unsworth *et al.* 2004; Klemperer, 2006).

(3) The Kunlun Fault Zone is also limited to the brittle upper crust (Zhu & Helmberger, 1998; Klemperer, 2006; Karplus *et al.*, 2011; Le Pape *et al.*, 2012) and exhibits local Quaternary normal faulting in addition to contemporary sinistral strike-slip activity (Jolivet *et al.*, 2003; Xu *et al.*, 2006). In fact, Oligocene–Quaternary normal fault activity associated with of the northern Tibetan margin has frequently occurred in the southern Kunlun Ranges (e.g. Arnaud *et al.*, 1993; Mock *et al.*, 1999; Elliott *et al.*, 2010).

(4) The centroid depth of the 2001 Hohxil earthquake was about 15 km, and the earthquake rupture was widely attributed to sinistral strike-slip activity along the Kunlun Fault Zone (e.g. Lin *et al.*, 2002; Li *et al.*, 2005; Tocheport *et al.*, 2006; Xu *et al.*, 2006); the depth of the rupture has a lower limit of 14·2–21 km, with 17 km as the optimal value (e.g. Wan *et al.*, 2004). Moreover, the normal component of the sub-events that occurred to the west of the earthquake rupture, near the epicenter locations (Fig. 1b and c) (e.g. Xu *et al.*, 2006) may be responsible for the uplift of Bukadaban Mountain (Fig. 1b and c) (Van der Woerd *et al.*, 2002; Tocheport *et al.*, 2006). In fact, in the west of the southern Kunlun Range, the 2008 Yutian earthquake occurred in the highest region (~6700 m) on Earth (Fig. 1a) and was also associated with a normal faulting event with a sinistral component of strike-slip motion (Elliott *et al.*, 2010). This event has been attributed to variations in the gravitational potential energy of the lithosphere related to the great elevation of the Tibetan Plateau (Elliott *et al.*, 2010).

(5) Based on tectonic and stratigraphic data, Yin *et al.* (2008*b*) proposed that lower crustal flow may be occurring beneath the Kunlun Range. They suggested that the southern margin of the Qaidam Basin has undergone transgression throughout the Cenozoic, which implies that the surface uplift rate induced by lower-crustal flow, if it has occurred, has been lower than the sedimentation rate.

We envisage that, under regional north–south compression caused by continuous north–south convergence between the Indian and Eurasian plates or the northward subduction of the Indian continent and the southward subduction of the Asian continent, the mid- to lower crust, weakened by partially molten layers in central–northern Tibet, may flow northward owing to the horizontal pressure gradient along the crustal channel. As a result, inflation of ductile crust and crustal thickening (McKenzie *et al.*, 2000; McKenzie & Jackson, 2002; Clark *et al.*, 2005) has occurred in response to blockage caused by the stronger Qaidam crust to the north, leading to surface uplift along the northern margin of the Tibetan Plateau (Fig. 16). In addition, the melt-weakened ductile mid- to lower crust may have also simultaneously flowed eastward owing to the blockage caused by the strong Tarim crust to the NW of Tibet (Fig. 16). If so, then in addition to the possible 'far-field stresses' triggered by the partitioning of the north–south convergence between the Indian and Eurasian plates (Lin *et al.*, 2002; Li *et al.*, 2005; Tocheport *et al.*, 2006; Xu *et al.*, 2006), the crustal melt-enhanced ductile flow may have caused eastward movement of the Songpang–Ganzi Block upper crust and triggered sinistral strike-slip activity on the Kunlun Fault Zone. As a result, mid- to lower crust-derived magmas have erupted, and shallow earthquakes (e.g. the 2001 Hohxil earthquake) have taken place along the Kunlun strike-slip fault zone (Figs 1b, c and 16). In fact, many researchers have suggested that eastward flow of the ductile mid- to lower crust is widespread (e.g. Royden *et al.*, 1997, 2008; Clark & Royden, 2000; Cowgill *et al.*, 2003; Clark *et al.*, 2005; Enkelmann *et al.*, 2006; Burchfiel *et al.*, 2008; Cook & Royden, 2008; Yao *et al.*, 2008; Bai *et al.*, 2010; Unsworth, 2010; Wang *et al.*, 2010). This may also have resulted in crustal thickening and subsequent surface uplift and extension accompanied by earthquakes along the eastern margin of the Tibetan Plateau (Burchfiel *et al.*, 2008; Royden *et al.*, 2008).

The crustal melt-enhanced ductile flow model discussed here differs from the block extrusion tectonic model in that the latter requires major bounding faults to cut the entire lithosphere whereas the flow model requires only upper crustal faulting. For instance, the 2001 Hohxil earthquake (Fig. 1a and b) has previously been attributed to sinistral strike-slip activity on the Kunlun Fault Zone that resulted from the eastward block extrusion of Tibet (Lin *et al.*, 2002; Li *et al.*, 2005). However, such an extrusion model requires that the Kunlun Fault Zone penetrates the entire lithospheric mantle (Tapponnier *et al.*, 2001), which is inconsistent with the brittle upper-crust depth of the Kunlun Fault Zone as defined by geophysical data (Owens & Zandt, 1997; Zhu & Helmberger, 1998; Klemperer, 2006; Karplus *et al.*, 2011; Le Pape *et al.*, 2012), particularly the lower depth limit (14·2–21 km) of the 2001 Hohxil earthquake rupture (e.g. Wan *et al.*, 2004). In fact, the Kulun Fault Zone cannot be an important rheological boundary because crustal melts at 20–45 km penetrate beyond this fault zone into northern Tibet (Le Pape *et al.*, 2012). Moreover, the melt penetration across the Kunlun Fault is accommodating crustal shortening in northern Tibet but may also characterize the growth of the plateau (Medvedev & Beaumont, 2006) to the north, with extension of the crustal thickening to the south of the Qaidam Basin (Karplus *et al.*, 2011). The extrusion model should be a low-temperature process that implies movement of discrete crustal blocks between lithosphere-penetrating faults (Tapponnier *et al.*, 2001), and possibly occurred during the early stages of collision between the India and the Eurasian plates (Owens & Zandt, 1997). Our crustal flow model, although also accounting for the sinistral strike-slip activity of the Kunlun Fault Zone and associated earthquakes (Fig. 16), is a high-temperature process that implies a decoupling of motions in the upper crust from those in the mid- to lower crust.

Yin *et al.* (2008*a*) proposed a model involving continental crystalline basement thrusting to explain the crustal thickening and surface uplift of the Qilian Shan–Nan Shan area to the north of the Qaidam Basin. In this model, lower crust beneath the northern Qaidam Basin may have undergone general shear deformation, accommodating thrusting, vertical crustal thickening and top-to-the-SW simple shear in the mid- to upper crust. Apart from crustal shortening, no lower crustal injection or thermal events in the mantle are needed to explain the current elevation (~3000–3500 m) and crustal thickness (45–50 km) of the northern Qaidam Basin and the southern Qilian Shan–Nan Shan thrust belt. The thrusting model of Yin *et al.* (2008*a*) is a low-temperature process similar to the block extrusion tectonic model. However, such a low-temperature process does not adequately account for the current >4500 m elevation and 60–70 km crustal thickness of the Kunlan Range to the south of the Qiadam Basin where high-temperature, lower crustal flow may play an important role in the current surface uplift and crustal thickening (Yin *et al.*, 2008*b*).

Crustal melt-enhanced ductile flow was probably initiated by the heating and eventual melting of the crust in response to the continuous convergence between the Indian and Eurasian plates (Owens & Zandt, 1997; Royden *et al.*, 2008). Such flow in the high-temperature or partially molten mid- to lower crust makes it easier to maintain a uniform elevation in the Tibetan Plateau (Owens & Zandt, 1997; Jamieson *et al.*, 2011) and would cause the present expansion and frequent earthquakes of the Tibetan Plateau along its northern and eastern margins (Fig. 1a) (Burchfiel *et al.*, 2008; Royden *et al.*, 2008). Worldwide (e.g. in the modern Andean and Anatolian plateaux), similar crustal melt-enhanced ductile flow events may have had widespread influence on the deep structure of the Earth's continental crust, in addition to limiting the thickness and elevation of mountain belts (e.g. Babeyko *et al.*, 2002; Unsworth, 2010; Jamieson *et al.*, 2011).

CONCLUSIONS

In this study, we explain the petrogenesis of 9·0–1·5 Ma tourmaline-bearing mica and biotite rhyolites in the Bukadaban–Malanshan area, southern Kunlun Range, which are geochemically similar to the Himalayan leucogranites. Importantly, the ~3·0–1·5 Ma rhyolites from the Bukadaban and Hudongliang areas are coeval with, or younger than, granulite xenolith-hosting basalts (Hacker *et al.*, 2000) and stand as the first petrological evidence for Tibetan crustal melting in the Quaternary. The Ulugh Muztagh, Weixueshan and BM leucogranites and rhyolites, as well as the western Wuxuefeng adakitic volcanic rocks, constitute an approximately east–west-trending Miocene–Quaternary crust-derived felsic volcanic zone (Fig. 1c). These felsic magmas originated from partial melting of the mid- to lower crust at depths of ~16–50 km, which is in good agreement with the depths of *c.* 15–50 km for the observed abnormally weak layers, lower seismic velocity zones or a crustal melt layer in northern Tibet (Owens & Zandt, 1997; Wei *et al.*, 2001; Unsworth *et al.*, 2004; Klemperer, 2006; Le Pape *et al.*, 2012). A crustal melt-enhanced ductile flow model can account for the formation of crustal inflation, surface uplift, and earthquakes along the northern margin of the Tibetan Plateau (Fig. 16).

ACKNOWLEDGEMENTS

We sincerely thank Professors Marjorie Wilson and Alberto Patiño Douce and two anonymous reviewers for their constructive and helpful reviews and suggestions. We also appreciate the assistance of Editorial Manager A. Lumsden. Tongzhen Guo, Lianchang Shi, Wei Peng, Guangpu Bao, Haiqing Chen, Yongwen Wang, Guangqian Hu, Haihong Chen, Xirong Liang, Xiangling Tu and Ying Liu are thanked for their assistance with laboratory and fieldwork.

FUNDING

Financial support for this research was provided by the Chinese Academy of Sciences (Knowledge Innovation Project KZCX2-YW-Q09-05-01), the National Natural Science Foundation of China (NSFC projects 41025006, 41073029 and 41121002) and the Guangzhou Institute of Geochemistry, Chinese Academy of Sciences (GIGCAS 135 project Y234021001). This is Contribution IS-1556 from GIGCAS, contribution 208 from the ARC Centre of Excellence for Core to Crust Fluid Systems (http://www.ccfs.mq.edu.au), and TIGeR publication #427.

SUPPLEMENTARY DATA

Supplementary data for this paper are available at *Journal of Petrology* online.

REFERENCES

Abdel Rahman, A. M. (1994). Nature of biotites from alkaline, calc-alkaline, and peraluminous magmas. *Journal of Petrology* **35(2)**, 525–541.

Arnaud, N. O., Vidal, P., Tapponnier, P., Matte, P. & Deng, W. M. (1992). The high K_2O volcanism of northwestern Tibet: Geochemistry and tectonic implications. *Earth and Planetary Science Letters* **111(2–4)**, 351–367.

Arnaud, N. O., Brunel, M., Cantagrel, J. M. & Tapponnier, P. (1993). High cooling and denudation rates at Kongur Shan, eastern Pamir (Xinjiang, China) revealed by $^{40}Ar/^{39}Ar$ alkali feldspar thermochronology. *Tectonics* **12**, 1335–1346.

Ashish, , Padhi, A., Rai, S. S. & Gupta, S. (2009). Seismological evidence for shallow crustal melt beneath the Garhwal High Himalaya, India: implications for the Himalayan channel flow. *Geophysical Journal International* **177**, 1111–1120.

Babeyko, A. Y., Sobolev, S. V., Trumbull, R. B., Oncken, O. & Lavier, L. L. (2002). Numerical models of crustal scale convection and partial melting beneath the Altiplano–Puna plateau. *Earth and Planetary Science Letters* **199(3–4)**, 373–388.

Bai, D., Unsworth, M. J., Meju, M. A., Ma, X., Teng, J., Kong, X., Sun, Y., Sun, J., Wang, L., Jiang, C., Zhao, C., Xiao, P. & Liu, M. (2010). Crustal deformation of the eastern Tibetan plateau revealed by magnetotelluric imaging. *Nature Geoscince* **3**, 358–362.

Barbarin, B. (1999). A review of the relationships between granitoid types, their origins and their geodynamic environments. *Lithos* **46(3)**, 605–626.

Barth, M. G., William, F., McDonough, W. F. & Rudnick, R. L. (2000). Tracking the budget of Nb and Ta in the continental crust. *Chemical Geology* **165**, 197–213.

Beaumont, C., Jamieson, R. A., Nguyen, M. H. & Lee, B. (2001). Himalayan tectonics explained by extrusion of a low-viscosity crustal channel coupled to focused surface denudation. *Nature* **414**, 738–742.

Bird, P. (1991). Lateral extrusion of lower crust from under high topography in the isostatic limit. *Journal of Geophysical Research* **96**, 10275–10286.

Black, L. P., Kamo, S. L., Allen, C. M., Davis, D. W., Aleinikoff, J. N., Valley, J. W., Mundil, R., Campbell, I. H., Korsch, R. J., Williams, I. S. & Foudoulis, C. (2004). Improved $^{206}Pb/^{238}U$ microprobe geochronology by the monitoring of a trace-element-related matrix effect; SHRIMP, ID-TIMS, ELA-ICP-MS and oxygen isotope documentation for a series of zircon standards. *Chemical Geology* **205**, 115–140.

Bruguier, O., Lancelot, J. R. & Malavieille, J. (1997). U–Pb dating on single detrital zircon grains from the Triassic Songpan–Ganze flysch (Central China): provenance and tectonic correlations. *Earth and Planetary Science Letters* **152**, 217–231.

Burchfiel, B. C., Molnar, P., Zhao, Z., Liang, K.u., Wang, S., Huang, M. & Sutter, J. (1989). Geology of the Ulugh Muztagh area, northern Tibet. *Earth and Planetary Science Letters* **94**, 57–70.

Burchfiel, B. C., Royden, L. H., van der Hilst, R. D., Hager, B. H., Chen, Z., King, R. W., Li, C., Lü, J., Yao, H. & Kirby, E. (2008). A geological and geophysical context for the Wenchuan earthquake of 12 May 2008, Sichuan, People's Republic of China. *GSA Today* **18**, 4–11.

Caldwell, B., Klemperer, S. L., Rai, S. S. & Lawrence, J. F. (2009). Partial melt in the upper–middle crust of the northwest Himalaya revealed by Rayleigh wave dispersion. *Tectonophysics* **477**, 58–65.

Capitanio, F. A., Morra, G., Goes, S., Weinberg, R. F. & Moresi, L. (2010). India–Asia convergence driven by the subduction of the Greater Indian continent. *Nature Geoscience* **3(2)**, 136–139.

Castro, A., Guiliermo Corretgé, L., El-biad, M., El-hmidi, H., Fernández, C. & Patiño Douce, A. E. (2000). Experimental constraints on Hercynian anatexis in the Iberian Massif, Spain. *Journal of Petrology* **41**, 1471–1488.

Chauvel, C., Lewin, E., Carpentier, M., Arndt, N. T. & Marini, J.-C. (2008). Role of recycled oceanic basalt and sediment in generating the Hf–Nd mantle array. *Nature Geoscience* **1(1)**, 64–67.

Chen, Y. L., Tang, J. R., Liu, F., Zhang, H. F., Nie, S. L. & Jiang, L. T. (2006). Elemental and Sm–Nd isotopic geochemistry of clastic sedimentary rocks in the Garzê–Songpan and Longmen Mountains. *Geology in China* **33**, 109–118 (in Chinese with English abstract).

Chung, S.-L., Chu, M.-F., Zhang, Y., Xie, Y., Lo, C.-H., Lee, T.-Y., Lan, C.-Y., Li, X., Zhang, Q. & Wang, Y. (2005). Tibetan tectonic evolution inferred from spatial and temporal variations in post-collisional magmatism. *Earth-Science Reviews* **68**, 173–196.

Chung, S.-L., Chu, M.-F., Ji, J., O'Reilly, S. Y., Pearson, N. J., Liu, D., Lee, T.-Y. & Lo, C.-H. (2009). The nature and timing of crustal thickening in Southern Tibet: Geochemical and zircon Hf isotopic constraints from postcollisional adakites. *Tectonophysics* **477**, 36–48.

Clark, M. K. & Royden, L. H. (2000). Topographic ooze: Building the eastern margin of Tibet by lower crustal flow. *Geology* **28**, 703–706.

Clark, M. K., Bush, J. W. M. & Royden, L. H. (2005). Dynamic topography produced by lower crustal flow against rheological strength heterogeneities bordering the Tibetan Plateau. *Geophysical Journal International* **162(2)**, 575–590.

Condie, K. C. (1993). Chemical composition and evolution of the upper continental crust: contrasting results from surface samples and shales. *Chemical Geology* **104**, 1–37.

Cook, K. L. & Royden, L. H. (2008). The role of crustal strength variations in shaping orogenic plateaus, with application to Tibet. *Journal of Geophysical Research* **113**, B08407, doi:10.1029/2007JB005457.

Cowgill, E., Yin, A., Harrison, T. M. & Wang, X.-F. (2003). Reconstruction of the Altyn Tagh fault based on U–Pb geochronology: Role of back thrusts, mantle sutures, and heterogeneous crustal strength in forming the Tibetan Plateau. *Journal of Geophysical Research* **108**, 2346, doi:10.1029/2002JB002080.

DeCelles, P. G., Robinson, D. M. & Zandt, G. (2002). Implications of shortening in the Himalayan fold–thrust belt for uplift of the Tibetan Plateau. *Tectonics* **21(6)**, 1062, doi:10.1029/2001TC001322.

Defant, M. J. & Drummond, M. S. (1990). Derivation of some modern arc magmas by melting of young subducted lithosphere. *Nature* **347**, 662–665.

Ding, L., Kapp, P., Zhong, D. & Deng, W. (2003). Cenozoic volcanism in Tibet: evidence for a transition from oceanic to continental subduction. *Journal of Petrology* **44**, 1833–1865.

Dini, A., Gianelli, G., Puxeddu, M. & Ruggieri, G. (2005). Origin and evolution of Pliocene–Pleistocene granites from the Larderello geothermal field (Tuscan Magmatic Province, Italy). *Lithos* **81**, 1–31.

Elliott, J. R., Walters, R. J., England, P. C., Jackson, J. A., Li, Z. & Parsons, B. (2010). Extension on the Tibetan plateau: recent normal faulting measured by InSAR and body wave seismology. *Geophysical Journal International* **183(2)**, 503–535.

England, P. & Houseman, G. (1989). Extension during continental convergence, with application to the Tibetan Plateau. *Journal of Geophysical Research* **94**, 17561–17579.

Enkelmann, E., Ratschbacher, L., Jonckheere, R., Nestler, R., Fleischer, M., Gloaguen, R., Hacker, B. R., Zhang, Y. Q. & Ma, Y.-S. (2006). Cenozoic exhumation and deformation of northeastern Tibet and the Qinling: Is Tibetan lower crustal flow diverging around the Sichuan Basin? *Geological Society of American Bulletin* **118**, 651–671.

Ferry, J. & Watson, E. (2007). New thermodynamic models and revised calibrations for the Ti-in-zircon and Zr-in-rutile thermometers. *Contributions to Mineralogy and Petrology* **154(4)**, 429–437.

Gaillard, F., Scaillet, B. & Pichavant, M. (2004). Evidence for present-day leucogranite pluton growth in Tibet. *Geology* **32**, 801–804.

Gao, S., Zhang, B., Gu, X., Xie, X., Gao, C. & Guo, X. (1995). Silurian–Devonian provenance changes of South Qinling Basin: implications for accretion of the Yangtze (South China) to the North China Craton. *Tectonophysics* **250**, 183–197.

Gao, S., Liu, X.-M., Yuan, H.-L., Hattendorf, B., Günther, D., Chen, L. & Hu, S.-H. (2002). Determination of forty two major and trace elements in USGS and NIST SRM glasses by laser ablation inductively coupled plasma-mass spectrometry. *Geostandards Newsletter* **26**, 181–195.

García-Casco, A., Haissen, F., Castro, A., El-Hmidi, H., Torres-Roldan, R. L. & Millán, G. (2003). Synthesis of staurolite in melting experiments of a natural metapelite: consequences for the phase relations in low-temperature pelitic migmatites. *Journal of Petrology* **44**, 1727–1757.

Grimes, C. B., John, B. E., Kelemen, P. B., Mazdab, F. K., Wooden, J. L., Cheadle, M. J., Hanghoj, K. & Schwartz, J. J. (2007). Trace element chemistry of zircons from oceanic crust: A method for distinguishing detrital zircon provenance. *Geology* **35(7)**, 643–646.

Grujic, D. (2006). Channel flow and continental collision tectonics: an overview. In: Law, R. D., Searle, M. P. & Godin, L. (eds) *Channel Flow, Ductile Extrusion and Exhumation in Continental Collision Zones. Geological Society, London, Special Publications* **268**, 25–37.

Grujic, D., Casey, M., Davidson, C., Hollister, L., Kündig, R., Pavlis, T. & Schmid, S. (1996). Ductile extrusion of the Higher Himalayan Crystalline in Bhutan: evidence from quartz microfabrics. *Tectonophysics* **260**, 21–44.

Grujic, D., Hollister, L.S. & Parrish, R. R. (2002). Himalayan metamorphic sequence as an orogenic channel: insight from Bhutan. *Earth and Planetary Science Letters* **198**, 177–191.

Guo, Z. & Wilson, M. (2012). The Himalayan leucogranites: Constraints on the nature of their crustal source region and geodynamic setting. *Gondwana Research* **22**, 360–376.

Guo, Z., Wilson, M., Liu, J. & Mao, Q. (2006). Post-collisional, potassic and ultrapotassic magmatism of the northern Tibetan Plateau: constraints on characteristics of the mantle source, geodynamic setting and uplift mechanisms. *Journal of Petrology* **47**, 1177–1220.

Hacker, B. R., Gnos, E., Ratschbacher, L., Grove, M., McWilliams, M., Sobolev, S. V., Wan, J. & Wu, Z. H. (2000). Hot and dry deep crustal xenoliths from Tibet. *Science* **287**, 2463–2466.

Harris, N. (2007). Channel flow and the Himalayan–Tibetan orogen: a critical review. *Journal of the Geological Society, London* **164(3)**, 511–523.

Harris, N. B. W. & Inger, S. (1992). Trace element modelling of pelite-derived granites. *Contributions to Mineralogy and Petrology* **110**, 46–56.

Harris, N. & Massey, J. (1994). Decompression and anatexis of Himalayan metapelites. *Tectonics* **13**, 1537–1546.

Harris, N., Ayres, M. & Massey, J. (1995). Geochemistry of granitic melts produced during the incongruent melting of muscovite: implications for the extraction of Himalayan leucogranitic magmas. *Journal of Geophysical Research* **100**, 15767–15777.

Harrison, T. M. (2006). Did the Himalayan Crystallines extrude partially molten from beneath the Tibetan Plateau? In: Law, R. D., Searle, M. P. & Godin, L. (eds) *Channel Flow, Ductile Extrusion and Exhumation in Continental Collision Zones Geological Society, London, Special Publications* **268**, 237–254.

Harrison, M. T., Grove, M., McKeegan, K. D., Coath, C. D., Lovera, O. M. & Fort, P. L. (1999). Origin and episodic emplacement of the Manaslu Intrusive Complex, Central Himalaya. *Journal of Petrology* **40(1)**, 3–19.

Hart, S. R. (1984). The DUPAL anomaly: a large-scale isotopic anomaly in the southern hemisphere. *Nature* **309**, 753–756.

Hetényi, G., Cattin, R., Brunet, F., Bollinger, L., Vergne, J., Nábělek, J. L. & Diament, M. (2007). Density distribution of the India plate beneath the Tibetan plateau: Geophysical and petrological constraints on the kinetics of lower-crustal eclogitization. *Earth and Planetary Science Letters* **264(1–2)**, 226–244.

Hofmann, A. W. (1997). Mantle geochemistry: the message from oceanic volcanism. *Nature* **385**, 219–229.

Huang, W. C., Ni, J. F., Tilmann, F., Nelson, D., Guo, J., Zhao, W., Mechie, J., Kind, R., Saul, J., Rapine, R. & Hearn, T. M. (2000). Seismic polarization anisotropy beneath the central Tibetan Plateau. *Journal of Geophysical Research* **105(B12)**, 27979–27990.

Huang, X. L., Xu, Y. G., Lo, C. H., Wang, R. C. & Lin, C. Y. (2007). Exsolution lamellae in a clinopyroxene megacryst aggregate from Cenozoic basalt, Leizhou Peninsula, South China: petrography and chemical evolution. *Contributions to Mineralogy and Petrology* **154**, 691–705.

Hubbard, J. & Shaw, J. H. (2009). Uplift of the Longmen Shan and Tibetan plateau, and the 2008 Wenchuan (M = 7·9) earthquake. *Nature* **458**, 194–197.

Huerta, A. D., Royden, L. H. & Hodges, K. V. (1999). The effects of accretion, erosion and radiogenic heat on the metamorphic evolution of collisional orogens. *Journal of Metamorphic Geology* **17(4)**, 349–366.

Inger, S. & Harris, N. (1993). Geochemical constraints on leucogranite magmatism in the Langtang Valley, Nepal Himalaya. *Journal of Petrology* **34(2)**, 345–368.

Ireland, T. R. & Williams, I. S. (2003). Considerations in zircon geochronology by SIMS. In: Hanchar, J. M. & Hoskin, P. W. O. (eds) *Zircon. Mineralogical Society of America and Geochemical Society, Reviews in Mineralogy and Geochemistry* **53**, 215–241.

Jackson, S. E., Pearson, N. J., Belousova, E. & Griffin, W. L. (2004). The application of laser ablation-inductively coupled plasma-mass spectrometry (LA-ICP-MS) to *in situ* U–Pb geochronology. *Chemical Geology* **211**, 47–69.

Jamieson, R. A., Beaumont, C., Fullsack, P. & Lee, B. (1998). Barrovian regional metamorphism: where's the heat?. In: Treloar, P. J. & O'Brien, P. J. (eds) *What Drives Metamorphism and*

Metamorphic Reactions? Geological Society, London, Special Publications **138**, 23–51.

Jamieson, R. A., Unsworth, M. J., Harris, N. B. W., Rosenberg, C. L. & Schulmann, K. (2011). Crustal melting and the flow of mountains. *Elements* **7(4)**, 253–260.

Jolivet, M., Brunel, M., Seward, D., Xu, Z., Yang, J., Malavieille, J., Roger, F., Leyreloup, A., Arnaud, N. & Wu, C. (2003). Neogene extension and volcanism in the Kunlun Fault Zone, northern Tibet: New constraints on the age of the Kunlun Fault. *Tectonics* **22**, 1052, doi:10.1029/2002TC001428.

Kapp, P., Murphy, M. A., Yin, A., Harrison, T. M., Ding, L. & Guo, J. (2003). Mesozoic and Cenozoic tectonic evolution of the Shiquanhe area of western Tibet. *Tectonics* **22**, 1029, doi:10.1029/2001TC001332.

Kapp, P., Yin, A., Harrison, T. M. & Ding, L. (2005). Cretaceous–Tertiary shortening, basin development, and volcanism in central Tibet. *Geological Society of American Bulletin* **117(7–8)**, 865–878.

Kapp, P., DeCelles, P. G., Gehrels, G. E., Heizler, M. & Ding, L. (2007). Geological records of the Lhasa–Qiangtang and Indo–Asian collisions in the Nima area of central Tibet. *Geological Society of American Bulletin* **119(7–8)**, 917–933.

Karplus, M. S., Zhao, W., Klemperer, S. L., Wu, Z., Mechie, J., Shi, D., Brown, L. D. & Chen, C. (2011). Injection of Tibetan crust beneath the south Qaidam Basin: Evidence from INDEPTH IV wide-angle seismic data. *Journal of Geophysical Research* **116(B7)**, B07301, doi:10.1029/2010jb007911.

Kellett, D. A., Grujic, D. & Erdmann, S. (2009). Miocene structural reorganization of the South Tibetan detachment, eastern Himalaya: Implications for continental collision. *Lithosphere* **1(5)**, 259–281.

Kind, R., Yuan, X., Saul, J., Nelson, D., Sobolev, S. V., Mechie, J., Zhao, W., Kosarev, G., Ni, J., Achauer, U. & Jiang, M. (2002). Seismic images of crust and upper mantle beneath Tibet: evidence for Eurasian plate subduction. *Science* **298(5596)**, 1219–1221.

King, J., Harris, N., Argles, T., Parrish, R., Charlier, B., Sherlock, S. & Zhang, H.F. (2007). First field evidence of southward ductile flow of Asian crust beneath southern Tibet. *Geology* **35(8)**, 727–730.

King, J., Harris, N., Argles, T., Parrish, R. & Zhang, H. (2011). Contribution of crustal anatexis to the tectonic evolution of Indian crust beneath southern Tibet. *Geological Society of America Bulletin* **123(1–2)**, 218–239.

Klemperer, S. L. (2006). Crustal flow in Tibet: geophysical evidence for the physical state of Tibetan lithosphere, and inferred patterns of active flow. In: Law, R. D., Searle, M. P. & Godin, L. (eds) *Channel Flow, Ductile Extrusion and Exhumation in Continental Collision Zones. Geological Society, London, Special Publications* **268**, 39–70.

Knesel, K. M. & Davidson, J. P. (2002). Insights into collisional magmatism from isotopic fingerprints of melting reactions. *Science* **296**, 2206–2208.

Koester, E., Pawley, A. R., Luís, A. D., Fernandes, L. A. D., Porcher, C. C. & Soliani, E., Jr (2002). Experimental melting of cordierite gneiss and the petrogenesis of syntranscurrent peraluminous granites in Southern Brazil. *Journal of Petrology* **43**, 1595–1616.

Koppers, A. A. P. (2002). ArArCALC—software for $^{40}Ar/^{39}Ar$ age calculations. *Computers and Geosciences* **28**, 605–619.

Le Bas, M. J., Le Maitre, R. W., Streckeisen, A. & Zanettin, B. (1986). A chemical classification of volcanic rocks based on the total alkali–silica diagram. *Journal of Petrology* **27**, 745–750.

Le Breton, N. & Thompson, A.B. (1998). Fluid-absent (dehydration) melting of biotite in metapelites in the early stages of crustal anatexis. *Contributions to Mineralogy and Petrology* **99**, 226–237.

Le Fort, P., Cuney, M., Deniel, C., France-Lanord, C., Sheppard, S. M. F., Upreti, B. N. & Vidal, P. (1987). Crustal generation of the Himalayan leucogranites. *Tectonophysics* **134**, 39–57.

Le Pape, F., Jones, A. G., Vozar, J. & Wenbo, W. (2012). Penetration of crustal melt beyond the Kunlun Fault into northern Tibet. *Nature Geoscience* **5**, 330–335.

Li, X. H., Li, Z.-X., Zhou, H., Liu, Y. & Kinny, P. D. (2002). U–Pb zircon geochronology, geochemistry and Nd isotopic study of Neoproterozoic bimodal volcanic rocks in the Kangdian Rift of South China: implications for the initial rifting of Rodinia. *Precambrian Research* **113**, 135–154.

Li, H., Van der Woerd, J., Tapponnier, P., Klinger, Y., Qi, X., Yang, J. & Zhu, Y. (2005). Slip rate on the Kunlun fault at Hongshui Gou, and recurrence time of great events comparable to the 14/11/2001, Mw∼7·9 Kokoxili earthquake. *Earth and Planetary Science Letters* **237**, 285–299.

Li, X. H., Li, Z. X., Wingate, M. T. D., Chung, S. L., Liu, Y., Lin, G. C. & Li, W. X. (2006). Geochemistry of the 755 Ma Mundine Well dyke swarm, northwestern Australia: Part of a Neoproterozoic mantle superplume beneath Rodinia? *Precambrian Research* **146**, 1–15.

Li, X. H., Liu, Y., Li, Q. L., Guo, C. H. & Chamberlain, K. R. (2009). Precise determination of Phanerozoic zircon Pb/Pb age by multicollector SIMS without external standardization. *Geochemistry, Geophysics, Geosystems* **10**, Q04010, doi:10.1029/2009GC002400.

Li, X. H., Long, W. G., Li, Q. L., Liu, Y., Zheng, Y. F., Yang, Y. H., Chamberlain, K. R., Wan, D. F., Guo, C. H., Wang, X. C. & Tao, H. (2010). Penglai zircon megacrysts: a potential new working reference material for microbeam determination of Hf–O isotopes and U–Pb age. *Geostandards and Geoanalytical Research* **34**, 117–134.

Lin, A. M., Fu, B. H., Guo, J. M., Zeng, Q. L., Dang, G. M., He, W. G. & Zhao, Y. (2002). Co-seismic strike-stip and rupture length produced by the 2001 M-s 8·1 Central Kunlun earthquake. *Science* **296**, 2015–2017.

Liu, Y., Hu, Z., Gao, S., Günther, D., Xu, J., Gao, C. & Chen, H. (2008). *In situ* analysis of major and trace elements of anhydrous minerals by LA-ICP-MS without applying an internal standard. *Chemical Geology* **257**, 34–43.

Liu, Y. S., Gao, S., Gao, C. G., Wang, D. B., Zong, K. Q. & Hu, Z. C. (2010). Timing of melt–peridotite interactions in xenoliths of the Trans-North China Orogen: U–Pb dating, Hf isotopes and trace elements in zircon. *Journal of Petrology* **51**, 537–571.

Ludwig, K. R. (2003). User's manual for Isoplot 3.00: a geochronological toolkit for Microsoft Excel. *Berkeley Geochronology Center Special Publication* **4**, 1–70.

McKenna, L. W. & Walker, J. D. (1990). Geochemistry of crustally derived leucocratic igneous rocks from the Ulugh Muztagh area, northern Tibet and their implications for the formation of the Tibetan Plateau. *Journal of Geophysical Research* **95**, 21483–21502.

McKenzie, D. & Jackson, J. A. (2002). Conditions for flow in the continental crust. *Tectonics* **21(6)**, 1055, doi:10.1029/2002TC001394.

McKenzie, D. & Priestley, K. (2008). The influence of lithospheric thickness variations on continental evolution. *Lithos* **102**, 1–11.

McKenzie, D., Nimmo, F., Jackson, J. A., Gans, P. B. & Miller, E. L. (2000). Characteristics and consequences of flow in the lower crust. *Journal of Geophysical Research* **105**, 11029–11046.

Medvedev, S. & Beaumont, C. (2006). Growth of continental plateaux by channel injection: Constraints and thermo-mechanical consistency. In: Law, R. D., Searle, M. P. & Godin, L. (eds) *Channel Flow, Ductile Extrusion and Exhumation in Continental Collision Zones. Geological Society, London, Special Publications* **268**, 147–164.

Meissner, R., Tilmann, F. & Haines, S. (2004). About the lithospheric structure of central Tibet, based on seismic data from the INDEPTH III profile. *Tectonophysics* **380**, 1–25.

Meyer, B., Tapponnier, P., Bourjot, L., Metivier, F., Gaudemer, Y., Pelzer, G., Shumin, G. & Zhitai, C. (1998). Crustal thickening in Gansu–Qinghai, lithospheric mantle subduction, and oblique, strike-slip controlled growth of the Tibet plateau. *Geophysical Journal International* **135**, 1–47.

Miller, C. F., Stoddard, E. F., Bradfish, L. J. & Dollase, W. A. (1981). Composition of plutonic muscovite; genetic implications. *Canadian Mineralogist* **19**, 25–34.

Mock, C., Arnaud, N. O. & Cantagrel, J.-M. (1999). An early unroofing in northeastern Tibet? Constraints from $^{40}Ar/^{39}Ar$ thermochronology on granitoids from the eastern Kunlun range (Qianghai, NW China). *Earth and Planetary Science Letters* **171(1)**, 107–122.

Montel, J. M. (1993). A model for monazite/melt equilibrium and application to the generation of granitic magmas. *Chemical Geology* **110**, 127–146.

Nábelek, J., Hetényi, G., Vergne, J., Sapkota, S., Kafle, B., Jiang, M., Su, H., Chen, J. & Huang, B.-S. (2009). the Hi-CLIMB TeamUnderplating in the Himalaya–Tibet collision zone revealed by the Hi-CLIMB Experiment. *Science* **325**, 1371–1374.

Nelson, K. D., Zhao, W. J., Brown, L. D., Kuo, J., Che, J. K., Liu, X. W., Klemperer, S. L., Makovsky, Y., Meissner, R., Mechie, J., Kind, R., Wenzel, F., Ni, J., Nabelek, J., Chen, L. S., Tan, H. D., Wei, W. B., Jones, A. G., Booker, J., Unsworth, M., Kidd, W. S. F., Hauck, M., Alsdorf, D., Ross, A., Cogan, M., Wu, C. D., Sandvol, E. & Edwards, M. (1996). Partially molten middle crust beneath southern Tibet: Synthesis of project INDEPTH results. *Science* **274**, 1684–1688.

Owens, T. J. & Zandt, G. (1997). Implications of crustal property variations for models of Tibetan plateau evolution. *Nature* **387**, 37–43.

Patiño Douce, A. E. (2005). Vapor-absent melting of tonalite at 15–32 kbar. *Journal of Petrology* **46**, 275–290.

Patiño Douce, A. E. & Harris, N. (1998). Experimental constraints on Himalayan anatexis. *Journal of Petrology* **39**, 689–710.

Patiño Douce, A. E. & McCarthy, T. C. (1998). Melting of crustal rocks during continental collision and subduction. In: Hacker, B. R. & Liou, J. G. (eds) *When Continents Collide: Geodynamics and Geochemistry of Ultrahigh-Pressure Rocks*. Dordrecht: Kluwer Academic, pp. 27–55.

Pearce, J. A., Harris, N. B. W. & Tindle, A. C. (1984). Trace element discrimination diagrams for the tectonic interpretation of granitic rocks. *Journal of Petrology* **25**, 956–983.

Peccerillo, A. & Taylor, S. R. (1976). Geochemistry of Eocene calc-alkaline volcanic rocks from the Kastamonu area, Northern Turkey. *Contributions to Mineralogy and Petrology* **58**, 63–81.

Pham, V. N., Boyer, D., Therme, P., Yuan, X. C., Li, L. & Jin, G. Y. (1986). Partial melting zones in the crust in southern Tibet from magnetotelluric results. *Nature* **319**, 310–314.

Plank, T. (2005). Constraints from thorium/lanthanum on sediment recycling at subduction zones and the evolution of the continents. *Journal of Petrology* **46(5)**, 921–944.

Plank, T. & Langmuir, C. H. (1998). The chemical composition of subducting sediment and its consequences for the crust and mantle. *Chemical Geology* **145**, 325–394.

Priestley, K., Debayle, E., McKenzie, D. & Pilidou, S. (2006). Upper mantle structure of eastern Asia from multimode surface waveform tomography. *Journal of Geophysical Research* **111(B10)**, 1–20.

Qiu, H. N. (2006). Construction and development of new Ar–Ar laboratories in China: Insight from GV-5400 Ar–Ar laboratory in Guangzhou Insitute of Geochemistry, Chinese Academy of Sciences. *Geochimica* **35**, 133–140 (in Chinese with English abstract).

Qiu, H. N. & Jiang, Y. D. (2007). Sphalerite $^{40}Ar/^{39}Ar$ progressive crushing and stepwise heating techniques. *Earth and Planetary Science Letters* **256**, 224–232.

Rapp, R. P. & Watson, E. B. (1995). Dehydration melting of metabasalt at 8–32 kbar: implications for continental growth and crust–mantle recycling. *Journal of Petrology* **36**, 891–931.

Rapp, R. P., Shimizu, N. & Norman, M. D. (2003). Growth of early continental crust by partial melting of eclogite. *Nature* **425**, 605–609.

Richards, A., Argles, T., Harris, N., Parrish, R., Ahmad, T., Darbyshire, F. & Draganits, E. (2005). Himalayan architecture constrained by isotopic tracers from clastic sediments. *Earth and Planetary Science Letters* **236(3–4)**, 773–796.

Royden, L. H., Burchfiel, B. C., King, R. W., Wang, E., Chen, Z. L., Shen, F. & Liu, Y. P. (1997). Surface deformation and lower crustal flow in eastern Tibet. *Science* **276**, 788–790.

Royden, L. H., Burchfiel, B. C. & van der Hilst, R. D. (2008). The geological evolution of the Tibetan Plateau. *Science* **321**, 1054–1058.

Rubatto, D. (2002). Zircon trace element geochemistry: partitioning with garnet and the link between U–Pb ages and metamorphism. *Chemical Geology* **184(1–2)**, 123–138.

Rubatto, D. & Hermann, J. (2007). Experimental zircon/melt and zircon/garnet trace element partitioning and implications for the geochronology of crustal rocks. *Chemical Geology* **241(1–2)**, 38–61.

Schmidt, M. W., Vielzeuf, D. & Auzanneau, E. (2004). Melting and dissolution of subducting crust at high pressures: the key role of white mica. *Earth and Planetary Science Letters* **228**, 65–84.

Searle, M. P. & Godin, L. (2003). The South Tibetan Detachment and the Manaslu leucogranite: a structural reinterpretation and restoration of the Annapurna–Manaslu Himalaya, Nepal. *Journal of Geology* **111**, 505–523.

Searle, M. P., Parrish, R. R., Hodges, K. V., Hurford, A., Ayres, M. W. & Whitehouse, M. J. (1997). Shisha Pangma leucogranite, South Tibetan Himalaya: field relations, geochemistry, age, origin, and emplacement. *Journal of Geology* **105**, 295–318.

Searle, M. P., Law, R. D. & Jessup, M. J. (2006). Crustal structure, restoration and evolution of the Greater Himalaya in Nepal–South Tibet: implications for channel flow and ductile extrusion of the middle crust. In: Law, R. D., Searle, M. P. & Godin, L. (eds) *Channel Flow, Ductile Extrusion and Exhumation in Continental Collision Zones. Geological Society, London, Special Publications* **268**, 355–378.

Searle, M. P., Stephenson, B. J., Walker, J. D. & Walker, C. B. (2007). Restoration of the western Himalaya: implications for metamorphic protoliths, thrust and normal faulting, and channel flow models. *Episodes* **30**, 242–257.

Searle, M. P., Cottle, J. M., Streule, M. J. & Waters, D. J. (2009). Crustal melt granites and migmatites along the Himalaya: melt source, segregation, transport and granite emplacement mechanisms. *Earth and Environmental Science Transactions of the Royal Society of Edinburgh* **100(Special Issue 1–2)**, 219–233.

Shapiro, N. M., Ritzwoller, M. H., Molnar, P. & Levin, V. (2004). Thinning and flow of Tibetan crust constrained by seismic anisotropy. *Science* **305**, 233–236.

She, Z., Ma, C., Mason, R., Li, J., Wang, G. & Lei, Y. (2006). Provenance of the Triassic Songpan–Ganzi flysch, west China. *Chemical Geology* **231**, 159–175.

Shi, D., Shen, Y., Zhao, W. & Li, A. (2009). Seismic evidence for a Moho offset and south-directed thrust at the easternmost Qaidam–Kunlun boundary in the Northeast Tibetan plateau. *Earth and Planetary Science Letters* **288(1–2)**, 329–334.

Stacey, J. S. & Kramers, J. D. (1975). Approximation of terrestrial lead isotope evolution by a two-stage model. *Earth and Planetary Science Letters* **26**, 207–221.

Stevens, G., Clemens, J. D. & Droop, G. T. R. (1997). Melt production during granulite-facies anatexis: experimental data from 'primitive' metasedimentary protoliths. *Contributions to Mineralogy and Petrology* **128**, 352–370.

Sun, S. S. & McDonough, W. F. (1989). Chemical and isotopic systematics of oceanic basalts: Implications for mantle composition and processes. In: Saunders, A. D. & Norry, M. J. (eds) *Magmatism in the Ocean Basins. Geological Society, London, Special Publications* **42**, 313–345.

Sylvester, P. J. (1998). Post-collisional strongly peraluminous granites. *Lithos* **45(1–4)**, 29–44.

Tapponnier, P., Xu, Z., Roger, F., Meyer, B., Arnaud, N., Wittlinger, G. & Yang, J. (2001). Oblique stepwise rise and growth of the Tibet Plateau. *Science* **294**, 1671–1677.

Tilmann, F. & Ni, J. (2003). Team, INDEPH III Seismic TeamSeismic imaging of the downwelling Indian lithosphere beneath central Tibet. *Science* **300**, 1424–1427.

Tocheport, A., Rivera, L. & Van der Woerd, J. (2006). A study of the 14 November 2001 Kokoxili earthquake: history and geometry of the rupture from teleseismic data and field observations. *Bulletin of the Seismological Society of America* **96**, 1729–1741.

Turner, S., Hawkesworth, C., Liu, J., Rogers, N., Kelley, S. & van Calsteren, P. (1993). Timing of Tibetan uplift constrained by analysis of volcanic rocks. *Nature* **364**, 50–54.

Turner, S., Arnaud, N., Liu, J., Rogers, N., Hawkesworth, C., Harris, N., Kelley, S., Van Calsteren, P. & Deng, W. (1996). Post-collision, shoshonitic volcanism on the Tibetan Plateau: Implications for convective thinning of the lithosphere and the source of ocean island basalts. *Journal of Petrology* **37(1)**, 45–71.

Unsworth, M. (2010). Magnetotelluric studies of active continent–continent collisions. *Surveys in Geophysics* **31(2)**, 137–161.

Unsworth, M., Wei, W., Jones, A. G., Li, S., Bedrosian, P., Booker, J., Jin, S., Deng, M. & Tan, H. (2004). Crustal and upper mantle structure of northern Tibet imaged with magnetotelluric data. *Journal of Geophysical Research* **109**, B02403, doi:10.1029/2002JB002305.

Unsworth, M. J., Jones, A. G., Wei, W., Marquis, G., Gokarn, S. G. & Spratt, J. E. (2005). Crustal rheology of the Himalaya and Southern Tibet inferred from magnetotelluric data. *Nature* **438**, 78–81.

Van der Woerd, J., Mériaux, A. S., Klinger, Y., Ryerson, F. J., Gaudemer, Y. & Tapponnier, P. (2002). The 14 November 2001, Mw 7·8 Kokoxili earthquake in Northern Tibet (Qinghai Province, China). *Seismological Research Letters* **73**, 125–135.

Vergne, J., Wittlinger, G., Hui, Q., Tapponnier, P., Poupinet, G., Mei, J., Herquel, G. & Paul, A. (2002). Seismic evidence for stepwise thickening of the crust across the NE Tibetan plateau. *Earth and Planetary Science Letters* **203**, 25–33.

Vielzeuf, D. & Schmidt, N. W. (2001). Melting relations in hydrous systems revisited: application to metapelites, metagreywackes and metabasalts. *Contributions to Mineralogy and Petrology* **141**, 251–267.

Visonà, D. & Lombardo, B. (2002). Two-mica and tourmaline leucogranites from the Everest–Makalu region (Nepal–Tibet). Himalayan leucogranite genesis by isobaric heating? *Lithos* **62**, 125–150.

Wan, Y. G., Wang, M., Shen, Z. K., Chen, J., Zhang, Z. S., Wang, Q. L. & Gan, W. J. (2004). Coseismic slip distribution of the 2001 west of Kunlun Mountain Pass earthquake inverted by GPS and leveling data. *Seismology and Geology* **26**, 393–404 (in Chinese).

Wang, Q., McDermott, F., Xu, J.-F., Bellon, H. & Zhu, Y.-T. (2005). Cenozoic K-rich adakitic volcanic rocks in the Hohxil area, northern Tibet: Lower-crustal melting in an intracontinental setting. *Geology* **33**, 465–468.

Wang, Q., Wyman, D. A., Xu, J., Dong, Y., Vasconcelos, P. M., Pearson, N., Wan, Y., Dong, H., Li, C., Yu, Y., Zhu, T., Feng, X., Zhang, Q., Zi, F. & Chu, Z. (2008). Eocene melting of subducting continental crust and early uplifting of central Tibet: Evidence from central–western Qiangtang high-K calc-alkaline andesites, dacites and rhyolites. *Earth and Planetary Science Letters* **272**, 158–171.

Wang, Q., Wyman, D. A., Li, Z.-X., Sun, W., Chung, S.-L., Vasconcelos, P. M., Zhang, Q., Dong, H., Yu, Y., Pearson, N., Qiu, H., Zhu, T. & Feng, X. (2010). Eocene north–south trending dikes in central Tibet: New constraints on the timing of east–west extension with implications for early plateau uplift? *Earth and Planetary Science Letters* **298**, 205–216.

Wang, Q., Li, Z. X., Chung, S. L., Wyman, D. A., Sun, Y. L., Zhao, Z. H., Zhu, Y. T. & Qiu, H. N. (2011). Late Triassic high-Mg andesite/dacite suites from northern Hohxil, North Tibet: Geochronology, geochemical characteristics, petrogenetic processes and tectonic implications. *Lithos* **126(1–2)**, 54–67.

Watson, E. B. & Harrison, T. M. (1983). Zircon saturation revisited: temperature and composition effects in a variety of crustal magma types. *Earth and Planetary Science Letters* **64**, 295–304.

Watson, E. B. & Harrison, T. M. (2005). Zircon thermometer reveals minimum melting conditions on earliest Earth. *Science* **308**, 841–844.

Watson, E. B., Wark, D. A. & Thomas, J. B. (2006). Crystallization thermometers for zircon and rutile. *Contributions to Mineralogy and Petrology* **151**, 413–433.

Wei, W. B., Unsworth, M., Jones, A., Booker, J., Tan, H. D., Nelson, D., Chen, L. S., Li, S. H., Solon, K., Bedrosian, P., Jin, S., Deng, M., Ledo, J., Ray, D. & Roberts, B. (2001). Detection of widespread fluids in the Tibetan crust by magnetotelluric studies. *Science* **292**, 716–718.

Weislogel, A. L., Graham, S. A., Chang, E. Z., Wooden, J. L., Gehrels, G. E. & Yang, H. (2006). Detrital zircon provenance of the Late Triassic Songpan–Ganzi complex: Sedimentary record of collision of the North and South China blocks. *Geology* **34**, 97–100.

Whitehouse, M. J., Claesson, S., Sunde, T. & Vestin, J. (1997). Ion microprobe U–Pb zircon geochronology and correlation of Archaean gneisses from the Lewisian Complex of Gruinard Bay, northwestern Scotland. *Geochimica et Cosmochimica Acta* **61**, 4429–4438.

Wiedenbeck, M., Allé, P., Corfu, F., Griffin, W. L., Meier, M., Oberli, F., von Quadt, A., Roddick, J. C. & Spiegel, W. (1995). Three natural zircon standards for U–Th–Pb, Lu–Hf, trace element and REE analyses. *Geostandards Newsletter* **19**, 1–23.

Wittlinger, G., Tapponnier, P., Poupinet, G., Mei, J., Danian, S., Herquel, G. & Masson, F. (1998). Tomographic evidence for localized lithospheric shear along the Altyn Tagh fault. *Science* **282**, 74–76.

Wittlinger, G., Farra, V., Hetényi, G., Vergne, J. & Nábělek, J. (2009). Seismic velocities in Southern Tibet lower crust: a receiver function approach for eclogite detection. *Geophysical Journal International* **177**, 1037–1049.

Wu, F. Y., Yang, Y. H., Xie, L. W., Yang, J. H. & Xu, P. (2006). Hf isotopic compositions of the standard zircons and baddeleyites used in U–Pb geochronology. *Chemical Geology* **234(1–2)**, 105–126.

Xu, X., Yu, G., Klinger, Y., Tapponnier, P. & Van Der Woerd, J. (2006). Reevaluation of surface rupture parameters and faulting segmentation of the 2001 Kunlunshan earthquake (Mw7·8), northern Tibetan Plateau, China. *Journal of Geophysical Research* **111**, B05316, doi:10.1029/2004JB003488.

Yao, H., Beghein, C. & Van Der Hilst, R. D. (2008). Surface wave array tomography in SE Tibet from ambient seismic noise and two-station analysis—II. Crustal and upper-mantle structure. *Geophysical Journal International* **173**, 205–219.

Yin, A. & Harrison, T. M. (2000). Geologic evolution of the Himalayan–Tibetan orogen. *Annual Review of Earth and Planetary Sciences* **28**, 211–280.

Yin, A., Dang, Y.-Q., Wang, L.-C., Jiang, W.-M., Zhou, S.-P., Chen, X.-H., Gehrels, G. E. & McRivette, M. W. (2008*a*). Cenozoic tectonic evolution of Qaidam basin and its surrounding regions (Part 1): The southern Qilian Shan–Nan Shan thrust belt and northern Qaidam basin. *Geological Society of America Bulletin* **120(7–8)**, 813–846.

Yin, A., Dang, Y.-Q., Zhang, M., Chen, X.-H. & McRivette, M. W. (2008*b*). Cenozoic tectonic evolution of the Qaidam basin and its surrounding regions (Part 3): Structural geology, sedimentation, and regional tectonic reconstruction. *Geological Society of America Bulletin* **120(7–8)**, 847–876.

Zhang, H., Harris, N., Parrish, R., Kelley, S., Zhang, L., Rogers, N., Argles, T. & King, J. (2004). Causes and consequences of protracted melting of the mid-crust exposed in the North Himalayan antiform. *Earth and Planetary Science Letters* **228**, 195–212.

Zhang, Z. & Klemperer, S. (2010). Crustal structure of the Tethyan Himalaya, southern Tibet: new constraints from old wide-angle seismic data. *Geophysical Journal International* **181**, 1247–1260.

Zhao, J., Yuan, X., Liu, H., Kumar, P., Pei, S., Kind, R., Zhang, Z., Teng, J., Ding, L., Gao, X., Xu, Q. & Wang, W. (2010). The boundary between the Indian and Asian tectonic plates below Tibet. *Proceedings of the National Academy of Sciences of the USA* **107**, 11229–11233.

Zhao, W., Kumar, P., Mechie, J., Kind, R., Meissner, R., Wu, Z., Shi, D., Su, H., Xue, G., Karplus, M. & Tilmann, F. (2011). Tibetan plate overriding the Asian plate in central and northern Tibet. *Nature Geoscience* **4(12)**, 870–873.

Zhu, B. Q., Chen, Y. W. & Peng, J. H. (2001). Lead isotope geochemistry of the urban enviroment in the Pearl River Delta. *Applied Geochemistry* **16**, 409–417.

Zhu, L. & Helmberger, D. V. (1998). Moho offset across the northern margin of the Tibetan Plateau. *Science* **281**, 1170–1172.

Zindler, A. & Hart, S. R. (1986). Chemical geodynamics. *Annual Review of Earth and Planetary Sciences* **14**, 493–571.